学位論文

An evaluation of the direct aerosol radiative forcing from satellite remote sensing and climate modeling

（衛星リモートセンシングと気候モデルによる エアロゾル直接放射強制力の評価）

平成 26 年 12 月　博士（理学）申請

東京大学大学院理学系研究科

地球惑星科学専攻

及川　栄治

Abstract

Anthropogenic and natural aerosols affect the Earth's radiation budget both in direct and indirect way. The direct aerosol effect on Earth's radiation budget is caused by direct scattering and absorption of solar and thermal radiation, and can be quantified by the radiative forcing. In this study, shortwave direct aerosol radiative forcing (SWDARF) is estimated by using satellite observation data and climate modeling, and the uncertainties of estimated SWDARF are discussed.

In 2006, the Cloud-Aerosol Lidar and Infrared Pathfinder Satellite Observations (CALIPSO) satellite was launched with the space-borne lidar, CALIOP (the Cloud-Aerosol Lidar with Orthogonal Polarization). CALIOP, for the first time, provides us with a global data of aerosol and cloud vertical profiles [*Winker et al*., 2009, 2013]. In addition, CALIOP has capability to detect aerosols existing above the optically thick clouds which are not observed by passive remote sensing and ground based lidar [*Winker et al*., 2010]. Several studies reported that absorbing aerosols above low-level clouds produce a large positive forcing over the Atlantic Ocean off southwest Africa [e.g. *Keil and Haywood*, 2003; *Chand et al*., 2009]. SWDARFs of aerosols above clouds have never been estimated in the global scale using observation data.

I investigate four scenarios for estimating the SWDARF at the top of the atmosphere (TOA) using data of CALIPSO lidar and data of MODIS sensor. The first scenario, which is called as clear-sky case, is the case that aerosols are observed in clear-sky condition. High cloud reflectance changes the SWDARF from negative to positive [*Haywood and Shine*, 1997]. Hence, I made three scenarios under cloudy-sky condition. The first is a case of aerosols existing above clouds (above-cloud case). The second is a case of aerosols existing below high-level clouds such as cirrus (below-cloud case). The third is a case of aerosols undetected by CALIOP lidar exist below/within the optically thick clouds (cloudy-undetected case). The cloudy-sky SWDARF is calculated by SWDARFs of above-cloud, below-cloud, and cloudy-undetected cases weighted by the occurrence probability of each scenario. The all-sky SWDARF is then calculated by combination of clear-sky and cloudy-sky SWDARF weighted by the cloud occurrence probability. In this study, the global scale estimate of cloudy-sky SWDARF is performed for the first time by using observation data. My analysis of the CALIPSO Version 3 product shows the occurrence probabilities in clear-sky, above-cloud, below-cloud, and cloudy-undetected cases are 38%, 4%, 16%, and 42%, respectively. This indicates that CALIOP can observe 58% of aerosols in all-sky condition, whereas the aerosol observation by passive remote sensing is limited only in clear-sky condition,

i.e. 38% of aerosols.

In clear-sky and below-cloud cases, aerosols mainly scatter sunlight and SWDARF shows negative values, except for bright surfaces. On the other hand, SWDARF globally shows positive value in above-cloud case. In this case, the absorption of aerosols is enhanced by the high reflectance of clouds and changes the SWDARF at TOA from negative to positive. As for the cloudy-undetected case, I assume the SWDARF to be zero, because optically thick clouds dominantly scatter the incident sunlight. The above mentioned method of analysis is applied to CALIPSO Version 2 and Version 3 products to obtain SWDARFs between 60°S and 60°N under clear-sky, cloudy-sky, and all-sky conditions as -3.7 ± 0.8, -3.7 ± 0.7, and -2.0 ± 1.2 Wm^{-2}. The result indicates the difference of the version of the CALIPSO product is as large as 50% in all-sky forcing.

According to previous studies of the global aerosol model intercomparison project AeroCom, SWDARF simulated by MIROC-SPRINTARS is smaller negative than the mean value of other model estimates [*Yu et al.*, 2006; *Schulz et al.*, 2006; *Myhre et al.*, 2013]. In this study, SWDARF is also calculated by the latest version of MIROC [*Watanabe et al.*, 2010]. In the MIROC model, the optical properties of aerosols and clouds are separately calculated in SPRINTARS aerosol module and mstrnX radiation module. By detailed investigation of aerosol optical thickness (AOT) and and single scattering albedo (SSA) from the two modules, I found that the mstrnX AOT and SSA are smaller than those of SPRINTARS, because aerosol size indices of mstrnX is different from that of SPRINTARS in order to save CPU time. In order to make the two modules consistent with each other, I modified the interface between the two modules to set common optical aerosol models with 6 size bins of mineral dust, 4 types of carbonaceous aerosols, sulfate, and 4 size bins of sea salt. In this study, this new model is referred to as the SPnew model. I confirmed that AOT of each aerosol component and SSA of mstrnX agree with those of SPRINTARS within 4% in the SPnew model. Absorption of dust and carbonaceous aerosols becomes smaller from the standard model to the SPnew model. Zonal averages of SWDARF between 60°S and 60°N under clear-sky, cloudy-sky, and all-sky conditions change from –2.0, +0.3, and –0.7 Wm^{-2} in the standard model to –2.1, –0.1, and –1.1 Wm^{-2} in SPnew model.

The vertical profiles of aerosols are globally observed by CALIPSO lidar under clear-sky condition. High concentrated aerosols are globally observed by CALIPSO lower than 2 km altitude; in particular, aerosol extinction coefficient is larger than 0.05 at altitude lower than 1 km. On the other hand, the aerosol extinction coefficient in SPnew model is underestimated globally below 2 km altitude, while aerosols are

elevated up to 7 km altitude around source regions of carbonaceous aerosols and dust in the model. These results indicate that aerosols are transported higher than the observation in a vertical direction, but are hardly transported in a horizontal direction in MIROC.

I compared the the obtained geographical distributions of AOT and SSA from satellites and models. The geographical distribution of CALIPSO AOT is found similar to that of MODIS observations, while CALIPSO AOT is smaller than MODIS AOT by 20%. Compared with CALIPSO and MODIS AOT, SPnew AOT is underestimated in almost all regions. This causes smaller negative SWDARF under clear-sky condition in the model. It is also found that under clear-sky condition the aerosol extinction coefficient of SPnew is smaller below 4 km altitude and larger above 4 km altitude than that of CALIPSO. The ratio of CALIPSO AOT to SPnew AOT (CALIPSO AOT / SPnew AOT) is 2.14 below 4 km and 0.29 above 4 km altitude. In order to study the effect of this difference, I performed a model simulation that aerosol concentrations multiplied by 2.14 below 4 km altitude and 0.29 above 4 km altitude in the SPnew model. This simulation is referred to as the SP4km experiment.

Zonal averages of SWDARF between 60°S and 60°N under clear-sky, cloudy-sky, and all-sky conditions are calculated in the SP4km experiment as –3.2, -0.3, and –1.7 Wm^{-2}. The zonal average AOT between 60°S and 60°N for SP4km is comparable to CALIPSO AOT and the modeled SSA is overestimated, but the zonal average of clear-sky SWDARF for SP4km is smaller negative than CALIPSO by 0.5 Wm^{-2}. This difference is mainly caused by an underestimation of aerosol extinction coefficient below 2 km altitude over ocean in the Southern Hemisphere.

MIROC frequently simulate optically thicker clouds than observation. Off southwest Africa, absorbing aerosols emitted by biomass burning in Africa are transported above low-level clouds. Aerosols usually undetected below 1.5 km altitude by CALIPSO observations in above-cloud case, whereas aerosols are simulated from surface to 5 km altitude in the model. In cloudy-sky condition, the modeled SWDARF is more positive than the observation, because the absorption of aerosols within/above clouds is largely enhanced by higher cloud reflectance derived from optically thick clouds. Over central and northern Pacific, optically thick clouds are simulated from the lower to upper troposphere in the model, so that clouds mainly scatter sunlight and aerosols cause less negative forcing than the CALIPSO case. From these results, the cloudy-sky SWDARF in MIROC is considered to be smaller negative than that of CALIPSO.

Summarizing the results in this study, I like to propose the best estimates of clear-sky and all-sky SWDARF of –4.1 and –1.9 Wm^{-2}. On the other hand, the global

averages of SWDARF from the past studies are -4.8 ± 0.8 and -2.7 ± 0.9 Wm^{-2} under clear-sky and all-sky conditions [*Liu et al*., 2007; *Kim and Ramanathan,* 2008; *Ma et al.,* 2012; *Zhang et al.,* 2012; *Kinne et al.,* 2013]. My estimate of the clear-sky SWDARF is located in between the CALIPSO values obtained in this study and the average of previous studies. This conclusion suggests that both the satellite-borne lidar and modeling methods have their own characteristic errors in SWDARF estimation. The present analysis is considered to be useful to identify causes for errors found in this study.

Contents

1. Introduction

Dust, sea salt, and volcanic sulfate are naturally emitted to the atmosphere as natural aerosols. Major sources of anthropogenic aerosols are, on the other hand, fossil fuel, biofuel, and biomass burning. Most of current global aerosol models treat natural aerosols, anthropogenic sulfate, black carbon (BC), and organic carbon (OC). Some models simulate these species and anthropogenic nitrate and secondary organic aerosols (SOA). Anthropogenic and natural aerosols affect the Earth's radiation budget both directly and indirectly. The direct aerosol effect is caused by direct scattering and absorption of solar and thermal radiation. The indirect aerosol effect is caused by the influence of aerosols that change the cloud microphysical and optical properties and also the cloud amount and lifetime by acting as cloud condensation nuclei (CCN) [*Twomey*, 1977; *Albrecht*, 1989]. Moreover, absorption of solar radiation by aerosols can influence the atmospheric temperature structure and lead to evaporation of cloud droplets. This phenomenon is called the semi-direct aerosol effect [*Hansen et al*., 1997; *Ackerman et al*., 2000].

In this study, I focus on the direct aerosol effect, which can be quantified by the radiative forcing. Under all-sky condition, direct aerosol radiative forcing (DARF) of anthropogenic aerosols has been estimated by various global models as -0.35 ± 0.5 Wm^{-2} [*IPCC,* 2013]. The Aerosol interComparison project AeroCom (http://nansen.ipsl.jussieu.fr/AEROCOM) attempts to the understanding of global aerosol life cycle and its impact on climate by performing a systematic analysis of more than 16 different global aerosol model results in addition to a comparison with satellite and surface measurements [e.g., *Kinne et al.*, 2006; *Textor et al*., 2006; *Schulz et al.*, 2006; *Myhre et al*., 2013]. DARF reported in *IPCC* [2013] was mainly based on the DARF simulated by the AeroCom models [*Myhre et al*., 2013]. AeroCom 16 models simulated the clear-sky and all-sky DARF of anthropogenic aerosols and resulted in mean values of -0.65 Wm^{-2} and -0.27 Wm^{-2} in clear-sky and all-sky conditions, respectively. The range of clear-sky DARF was from -0.35 to -1.01 Wm^{-2} and that of all-sky DARF was -0.58 to -0.02 Wm^{-2}. Several models did not include nitrate or SOA for the simulation. A correction of the model estimates for missing aerosol components leaded the mean all-sky DARF to be -0.35 Wm^{-2}. There are still large uncertainties in DARF calculated by various global aerosol models that estimate the climate effects by aerosols.

Total (natural and anthropogenic) aerosols are observed by ground-based and satellite-based measurements. AERosol RObotic NETwork (AERONET) [*Holben et al.*, 1998] and SKYNET [*Nakajima et al.*, 1996] are the world-wide ground-based

observation networks to retrieve aerosol parameters (aerosol optical thickness (AOT), single scattering albedo (SSA), the complex refractive index, and the size and shape distributions from spectral and multiangular sun/sky radiometer observations. Although the high-quality observations come from ground-based observations, satellite observations cover the land and ocean on a global scale. Especially, aerosol observations by the Moderate Resolution Imaging Spectroradiometer (MODIS) sensors aboard the Aqua and Terra satellites are well-known [e.g., *Remer et al.*, 2005, 2008]. Validation of MODIS observations was conducted using AERONET observations over both land and ocean [e.g., *Chu et al*., 2002; *Ichoku et al.*, 2002; *Remer et al*., 2002]. Assumed retrieved errors of MODIS AOT are $\Delta\tau = \pm(0.03 + 0.05\tau)$ over ocean, and $\Delta\tau = \pm(0.05 + 0.15\tau)$ over land, where τ represents AOT [*Remer et al.*, 2005, 2008]. *Remer et al.* [2008] reported that the multiannual global averages of AOT at 550 nm over ocean were 0.13 for Aqua and 0.14 for Terra, and those over land were 0.19 for both Aqua and Terra; however, AOT over the bright surfaces (deserts and snow and ice surfaces) is not retrieved by using the dark target approach, because the observed radiance is dominated by the surface reflectance. It should be noted that the land AOT is the averages over the land except for desert regions and cryosphere.

Recent studies about the clear-sky shortwave DARF (SWDARF) of total aerosols at the top-of-atmosphere (TOA) were summarized in *Yu et al.* [2006]. The satellite-based SWDARF was estimated to be -5.3 ± 0.2 Wm^{-2} and the model-based SWDARF was -3.3 ± 0.6 Wm^{-2}. The difference of SWDARF between observations and models were larger than the standard errors of observed and modeled SWDARFs. It is said that the MODIS-retrieved AOT tends to be overestimated by about 10 to 15%, because of contamination of thin cirrus [*Kaufman et al.*, 2005]. Such overestimation of AOT would result in a comparable overestimate of SWDARF. The modeled SWDARF was smaller than the measurement-based SWDARF by about 30 to 40%, even after accounting for a cloud contamination.

The global mean DARF at the TOA for anthropogenic and total aerosols were summarized in Fig. 1-1. On the global scale, aerosols mainly cool the Earth by reflecting sunlight back to space, that is, aerosols cause a negative forcing. The magnitude of the negative forcing for total aerosols is several times greater than that for anthropogenic aerosols. One of global aerosol models that have participated in AeroCom project is called Spectral Radiation-Transport Model for Aerosol Species (SPRINTARS) [*Takemura et al*., 2000, 2005, 2009]. The DARFs calculated by SPRINTARS are also summarized in Fig. 1-1. SPRINTARS simulated −0.71 and −0.14 Wm^{-2} for the clear-sky and all-sky DARFs of anthropogenic aerosols, respectively. The

clear-sky forcing was comparable to the model average, while the all-sky forcing was a half the value of the model average. It could be that since nitrate and SOA were not included in SPRINTARS simulation. In view of different aerosol components simulated in different models, the SPRRINTARS all-sky forcing became close to the model average; however, the SPRINTARS clear-sky forcing became largely different from the model average. The clear-sky DARF for total aerosols was also simulated by SPRINTARS in the model and observation comparison exercises [*Yu et al*., 2006]. The clear-sky DARF of SPRINTARS was −1.7 Wm^{-2}; even allowing for missing aerosol components, the SPRINTARS DARF for total aerosols was smaller than DARFs by other studies.

One of uncertainties in the evaluated DARF is the effect of vertical stratification of aerosols and clouds. Previous studies suggested that the all-sky DARF significantly depends on the amount of aerosols loaded above the cloud layer. In particular, absorbing aerosols as emitted from biomass burning above clouds produce a large positive forcing off southern Africa and South America [*Keil and Haywood*, 2003; *Takemura et al*., 2005]. *Haywood et al.* [2004] used the vertical profiles of aerosols and clouds off the coast of southern Africa from aircraft measurements to demonstrate that MODIS retrievals exhibit a low bias in the cloud optical thickness (COT) and cloud effective radius. *De Graaf et al.* [2012] used data of passive satellite spectrometry from the ultraviolet to the shortwave infrared for estimating aerosol solar absorption by the above-cloud aerosols. The cloud optical properties were retrieved using three channels in shortwave infrared for calculating the cloud reflectance in the modeled aerosol-free condition. SWDARF was estimated by the difference of the cloud reflectance between measurements and modeled aerosol-free calculations. They reported that SWDARF of above-cloud absorbing aerosols off southern Africa was +23 Wm^{-2} in August 2006.

In 2006, the Cloud-Aerosol Lidar and Infrared Pathfinder Satellite Observations (CALIPSO) satellite was launched with the space-borne lidar, CALIOP (the Cloud-Aerosol Lidar with Orthogonal Polarization), as one of the NASA Earth System Science Pathfinder (ESSP) programs. CALIOP, for the first time, provided us with global data of aerosol and cloud vertical profiles [*Winker et al*., 2009, 2013]. Clouds and aerosols were discriminated using a combination of 532 nm backscatter magnitude and attenuated color ratio, which is the ratio of 1064 to 532 nm of attenuated backscatter intensity [*Liu et al*., 2009]. Vertical profiles of extinction coefficients for clouds and aerosols were retrieved from the extinction retrieval algorithms [*Young and Vaughan*, 2009]. *Winker et al*., [2013] showed some aerosol characteristics retrieved by the CALIPSO measurements. In most regions, clear-sky and all-sky mean extinction

profiles for aerosols were similar; it implied that aerosol loadings in the lower troposphere are uncorrelated with the occurrence of high-level clouds. Diurnal differences of the column AOT was larger over land than over ocean. In addition, CALIOP can detect and retrieve aerosols above clouds [*Winker et al*., 2010], while these aerosols are undetected from ground-based lidar measurements. *Chand et al.* [2009] evaluated the direct aerosol effect over the Atlantic Ocean off southwest Africa using AOT of aerosols above optically thick low-level clouds quantified by retrieval methods of *Hu et al.* [2007] and *Chand et al.* [2008]. *Chand et al.* [2009] reported that the DARF largely depends on the fractional coverage and albedo of the underlying clouds: thus, cloud and aerosol profiling is significantly important for an accurate evaluation of the direct aerosol effect.

In this study, the global all-sky SWDARF of the total (natural plus anthropogenic) aerosols is calculated using aerosol and cloud distributions of both CALIPSO observations and global aerosol modeling with SPRINTARS [*Takemura et al*., 2000, 2005, 2009] for discussing the uncertainties of estimation of SWDARF from observations and models. Distributions of aerosols and clouds from CALIPSO and MODIS observations and satellite-based SWDARF are shown in chapter 2. I present a new method of improving aerosol optical modeling in the SPRINTARS and the radiation code in chapter 3. Comparisons between observations and model simulations are made in chapter 4 to study the sensitivity of the model simulation to the assumed aerosol characteristics. The overall results are summarized and discussed in chapter 5.

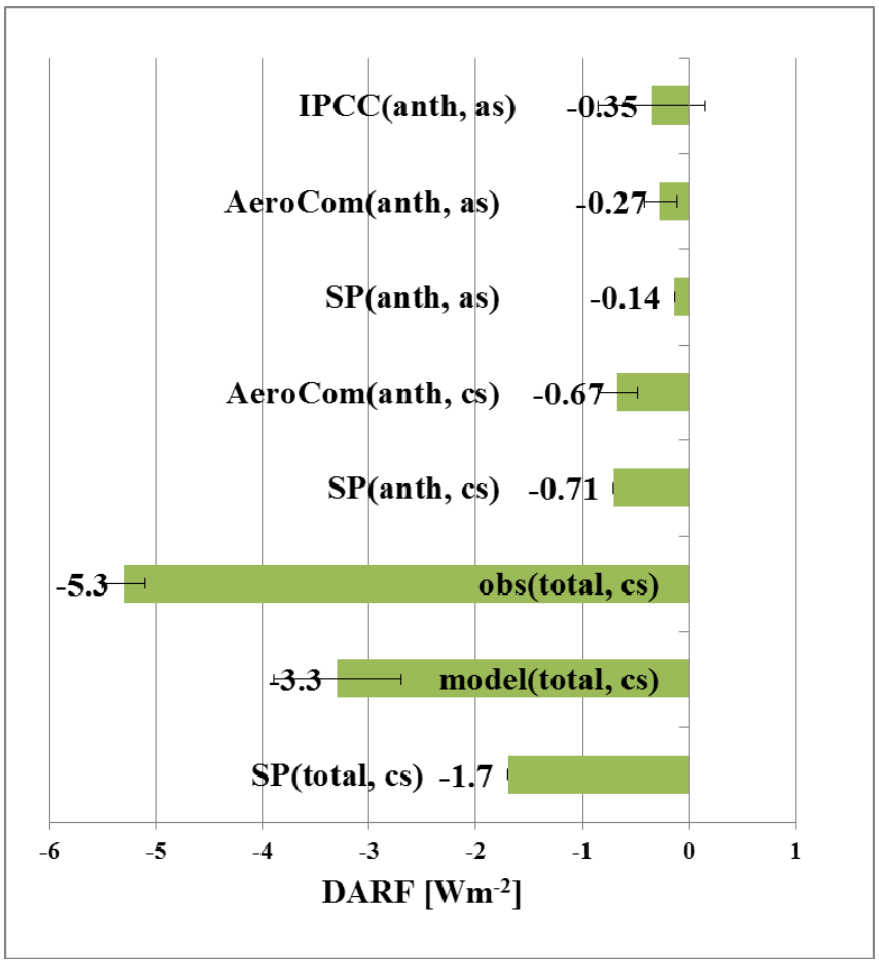

Fig. 1-1. Direct aerosol radiative forcing (DARF) at the top of atmosphere for anthropogenic and total (anthropogenic+natural) aerosols. Data of the all-sky and clear-sky DARF for anthropogenic aerosols ((anth, as) and (anth, cs)) are referred to *IPCC* [2013] and the simulation results of the AeroCom models (AeroCom) and SPRINTARS model (SP) [*Myhre et al*., 2013]. The clear-sky DARFs for total aerosols (total, cs) are estimated by the multi-satellite observations (obs) and multi-models (model) and SPRINTARS model [*Yu et al*., 2006].

2. Direct aerosol radiative forcing of CALIPSO satellite measurements

In this study, I use CALIPSO Level 2 Products Version 2 (V2) and Version 3 (V3) for investigating the 3D distributions of aerosols and clouds, and for estimating the all-sky SWDARF. Although the retrieval algorithms of V3 product are different from those of V2 product, the same aerosol model (lidar ratio, size distribution, and refractive index) [*Omar et al*., 2009] is used in V2 and V3 algorithms. The DARF depends on the 3D distributions of aerosols and clouds, and also on the aerosol optical properties. This situation is convenient for me to evaluate the algorithm dependence of DARF on the 3D distribution of aerosols and clouds but with the same aerosol optical properties used in V2 and V3 algorithms. Monthly mean values of observation data are used for calculating the SWDARF between 60°S and 60°N for each month from 2007 to 2009. Aerosol and cloud fields from 60°S to 60°N are obtained from CALIPSO and Moderate Resolution Imaging Spectroradiometer (MODIS) sensors throughout the year. I need to cut the high latitude regions off from our analysis, because MODIS cloud optical thickness (COT) is not retrieved in the high latitudes, which is necessary for the all-sky SWDARF calculation (see section 2.4). I can explore higher latitudes up to 70°, but the sampling becomes uneven depending on the season; thus the resulting map may not be consistent.

2.1 CALIPSO observations

The CALIOP's laser produces linear polarized pulses at two wavelengths (532 nm and 1064 nm) from a near nadir-viewing geometry during both day and night phases of the orbit; then, its receiver measures the total backscattered intensity at 1064nm and the parallel and perpendicular attenuated backscatter coefficients ($\beta'_{par}(z)$, $\beta'_{perp}(z)$) at 532 nm. The total attenuated backscatter coefficient $\beta'(z)$ at 532 nm is written as

$$\beta'(z) = \beta'_{par}(z) + \beta'_{perp}(z), \tag{2-1}$$

$$\begin{aligned} \beta'(z) &= \beta'_p(z) + \beta'_m(z) \\ &= \left[\beta_p(z) + \beta_m(z)\right] T^2(0,z) \\ &= \left[\beta_p(z) + \beta_m(z)\right] T_m^2(0,z) T_p^2(0,z) \end{aligned}, \tag{2-2}$$

where the subscripts p and m indicate particles and molecules including ozone, respectively, and $T^2(0,z)$ is two-way transmittance from the top of atmosphere (TOA) to the altitude z.

2.1.1 Level 2 aerosol and cloud products

The CALIPSO level 2 data processing consists of the layer detection of aerosols and clouds, the scene classification which identifies these layers as clouds or aerosols, aerosol type, and cloud ice–water phase, and the retrieval of the profiles of particle backscatter and extinction coefficients [*Vaughan et al*., 2009; *Winker et al*., 2009].

First, the detection of aerosol and cloud layers is performed [*Vaughan et al*., 2009; *Winker et al*., 2009]. Dense clouds can be detected from single lidar shots, but detection of layers for aerosol and weakly scattering clouds usually requires averaging of multiple lidar shots. In production data processing, layer detection is performed on single shots (1/3 km) and on profiles horizontally averaged over 1, 5, 20, and 80 km. To detect tenuous aerosol layers and avoid cloud contamination, cloud and aerosol layers found at finer spatial resolutions (less averaging) are removed before further horizontal averaging.

Aerosol and cloud layers are detected in the atmospheric return signal as enhancements above the signal expected from the molecular background. The layer finding is performed using a threshold technique applied to a profile of attenuated scattering ratio $R'(z)$:

$$R'(z) = \frac{\beta'(z)}{\beta'_m(z)}, \tag{2-3}$$

where $\beta'_m(z)$ is attenuated backscatter coefficients at 532 nm for molecules (m). The profile of $\beta'_m(z)$ is estimated using the profile data of molecular and ozone number density from the Goddard Earth Observing System Model, version 5 (GEOS-5) analysis product available from the NASA's Global Modeling and Assimilation Office (GMAO).

Second, the scene classification is performed. Aerosols generally have relatively small values of $\beta'(z)$ and color ratio χ', while clouds have large values of $\beta'(z)$ and χ'. Color ratio χ' is

$$\chi' = \frac{\beta'_{532}}{\beta'_{1064}}. \tag{2-4}$$

The cloud-aerosol discrimination (CAD) [*Liu et al*., 2009] is driven by the following confident function:

$$f_{\text{CAD-3D}} = \frac{P_c(\beta'_{532}, \chi', z) - P_a(\beta'_{532}, \chi', z)}{P_c(\beta'_{532}, \chi', z) + P_a(\beta'_{532}, \chi', z)}, \tag{2-5}$$

where z is altitude. The function f_{CAD} is a normalized differential probability that ranges from -1 to 1. According to the definition of function f_{CAD}, the layer is classified as cloud

when $f_{CAD} \geq 0$ and as aerosol when $f_{CAD} < 0$. The CAD score reported in the CALIPSO level 2 products is a percentile of function f_{CAD} in the range from -100 to 100. The CAD score is the value of quality assurance of discrimination between aerosol and cloud for each layer and the absolute value of the CAD score provides a confidence level for the classification.

After aerosol and cloud layers are defined, the type of aerosols and clouds are determined. Aerosol layers are classified as one of the six CALIPSO aerosol types [*Omar et al*., 2009], while cloud layers are classified into two types, i.e. water or ice. The six CALIPSO aerosol types are desert dust, smoke, clean continental, polluted continental, marine, and polluted dust. Here, polluted dust is a mixture of dust and smoke aerosols. The aerosol types are determined by using the parameters (backscattering intensity, depolarization ratio, altitude, location, and surface type).

Finally, the extinction retrievals [*Young and Vaughan*, 2009] are performed by using the layer information of aerosols and clouds. Optical thickness of particles (aerosols and clouds) is defined as

$$\tau_p = \int_{z_1}^{z_2} \sigma_p(z)\, dz\,, \tag{2-6}$$

where σ_p is extinction coefficient and Z_1 and Z_2 are bottom and top altitudes of the particle layer. In the lidar retrieval, σ_p is defined as

$$\sigma_p(z) = \beta_p(z) \times S_p\,, \tag{2-7}$$

where S_p is the lidar ratio (extinction-to-backscatter ratio). S_p depends on particle type and S_p at 532 nm for CALIPSO retrievals is listed in Table 2-1. In the CALIPSO analysis, the iterative calculation is performed for estimation of $\beta_p(z)$.

2.1.2 Improvement from version 2 to version 3 product

Level 2 Lidar data V3 product was significantly improved over previous versions. The daytime calibration procedures [*Powell et al*., 2010] and the cloud-aerosol discrimination algorithms [*Liu et al*., 2010] were improved from V2 to V3 algorithms. In the V3 algorithms, the layer detection module was modified for determining base heights of low-level aerosol layers correctly [*Vaughan et al*., 2010], then a cloud thermodynamic phase is determined using the method of *Hu et al*., [2009].

In V2 product, the unexpected weakly scattering cumulus clouds are frequently included in the 5 km layer products. The layer detection algorithm using $R'(z)$ and the cloud clearing were performed properly at 1/3 km and 1 km resolutions. In layer

detection processing, cloud and aerosol layers found at finer spatial resolutions are removed before the coarser horizontal averaging of $R'(z)$. On the other hand, the CAD algorithm uses $\beta'(z)$ including cloud information, which is removed in the layer detection, at 5, 20, and 80 km resolutions and clouds are more classified in V2 algorithms. In V3 algorithms, the cloud clearing from the layer detection is also used in CAD algorithms [*Vaughan et al*., 2010]. From this bug fixing, small scale clouds embedded in the extensive aerosol layer are more accurately cleared.

In V2 product, very dense dust and smoke layers near source regions were frequently misclassified as clouds, because the scattering characteristics of dense dust layers are nearly identical to those of optically thin clouds in the 3-dimensional function $f_{\text{CAD-3D}}$ in Eq. (2-5), which is used for CAD algorithms. By adding dimensions of attenuated depolarization ratio δ' and latitude *lat*, a new 5-dimensional function $f_{\text{CAD-5D}}$ [*Liu et al*., 2010] was developed as

$$f_{\text{CAD-5D}} = \frac{P_c(\beta'_{532}, \chi', \delta', z, lat) - P_a(\beta'_{532}, \chi', \delta', z, lat)}{P_c(\beta'_{532}, \chi', \delta', z, lat) + P_a(\beta'_{532}, \chi', \delta', z, lat)}, \tag{2-8}$$

$$\delta' = \frac{\beta'_{perp}}{\beta'_{par}}. \tag{2-9}$$

Dense dust and smoke layers located near the source regions were misclassified as cloud by the 3D algorithm used in the V2 product, while they were well separated from clouds in the 5D algorithm. Note that some very dense parts of aerosol layer appeared to be still misclassified as clouds in the V3 product.

In the satellite lidar retrievals, the erroneous estimates of base altitude of highly absorbing and optically thick aerosol layers are occurred over bright surfaces during day time, because relatively weak backscattering from absorbing aerosols and very high noise can cause the return signal to fall below the detection limit. In V3 algorithms, aerosol base altitude is extended downward to 90 m above the top of the surface spike, if the following three conditions are satisfied [*Vaughan et al.*, 2010]. The first condition is that the lowest layer is an aerosol and the altitude of initial layer base is within 2.5 km of the surface. The second condition is that surface echo was detected below the aerosol layer. The third condition is that the integrated $\beta'(z)$ at 532 nm from the surface echo to the initial base altitude is positive. After the readjustment of the aerosol layer base altitude, the retrievals of extinction and optical properties are conducted. Compared with the airborne high spectral resolution lidar (HSRL) measurement, AOT in V2 product is obviously underestimated. AOT in V3 product is uniformly larger than that in the previous version and closer to the HSRL observation, due to the effects of base

extension procedure.

In V2 algorithms, the cloud thermodynamic phase discrimination to classify water and ice particles is based on the layer-integrated δ'. It assumes that backscattered light from ice crystals is depolarizing, whereas water clouds, which are spherical particles, result in minimal depolarization. For water clouds, δ' can be large in CALIPSO observations because of multiple scattering, whereas horizontally oriented ice particles depolarize only weakly and behave similarly to water clouds. Based on theoretical and modeling studies, an improved cloud phase determination algorithm had been developed [*Hu et al*., 2009]. This new algorithm differentiates cloud phase by using the spatial correlation of layer-integrated $\beta'(z)$ and layer-integrated particulate depolarization ratio. Three cloud types (ice clouds containing randomly oriented particles, ice clouds with horizontally oriented particles, and water clouds) are included in V3 product.

From these improvements, the misclassification of aerosols as clouds and overestimation of low-level cloud fraction are improved. In the V3 product, more aerosols are primarily detected in the boundary layer over the regions where dust, smoke, and polluted aerosols are frequently emitted. In addition, marine aerosols are more frequently observed over the ocean in southern hemisphere [*Liu et al*., 2010].

In this study, aerosol and cloud layers are defined when the absolute value of CAD score is higher than 70 for quality assurance of aerosol and cloud data in V2 and V3 products. In Fig. 2-1, fractions of aerosols and clouds identified in my quality control procedure using V2 and V3 products from 2007 to 2009 for 1 km vertical bins from surface to 6 km altitude. The sum of fractions of aerosols and clouds are similar at all altitudes between V2 and V3 products. The aerosol fraction increases from V2 to V3 product by 16% between 0 and 1 km altitude and by 9% between 1 and 2 km altitude. The change of fraction below 2 km was caused by a cloud clearing bug in the V2 algorithm and improvement of aerosol base height identification scheme and CAD algorithms [*Vaughan et al.*, 2010; *Liu et al*., 2010].

2.1.3 Validation studies

Kittaka et al. [2011] compared CALIPSO V2 AOT and Aqua MODIS Collection 5 AOT. The global mean of MODIS AOTs, which were collocated with CALIPSO AOTs, was 0.08 to 0.12 depending on the applied cloud clearing method. When the most stringent cloud clearing was used, the global means of collocated CALIPSO and MODIS AOT were in good agreement, and the differences of AOTs were 0.007 and 0.012 over ocean and land, respectively. However, regional differences are found, i.e.,

CALIPSO AOT was lower than MODIS AOT over China, Middle East, and Europe, and was higher than MODIS AOT over central and southern Africa. *Redemann et al.* [2012] compared both CALIPSO V2 and V3 AOTs against Aqua MODIS AOT. CALIPSO V3 AOT was higher than V2 AOT and the monthly-mean AOT of CALIPSO V3 was comparable to that of MODIS within 0.03 and 0.04 over the ocean. CALIPSO AOT was generally lower than MODIS AOT. *Omar et al.* [2013] compared CALIPSO V3 AOT at 532 nm with the ground-based AERONET AOT at 500 nm. The mean difference of AOT for the two instruments was 25%. CALIPSO AOT was lower than AERONET AOT, when AERONET AOT was lower than 0.1. Possible reasons of AOT difference were cloud contamination, difference of viewing angles of two instruments, and inhomogeneity of aerosols. *Winker et al*. [2013] pointed out that the magnitudes of aerosol extinction of CALIPSO product might be underestimated in the upper troposphere, due to detection limits of the CALIPSO level 2 retrieval algorithms.

2.2 Data

In this study, aerosol and cloud products, surface albedo, and meteorological data are averaged to a horizontal resolution of 1°×1°. Analysis and radiation computations have also been performed with a horizontal resolution of 1°×1°.

2.2.1 CALIPSO Level 2 layer products

The CALIPSO Lidar Level 2 Cloud and Aerosol Layer Products Version 2 and Version 3 (https://eosweb.larc.nasa.gov/project/calipso/calipso_table) of 5 km horizontal resolution are used for the radiation calculation. CALIPSO level 2 products consist of the properties of the atmospheric features (e.g., cloud and aerosol layers). In this study, AOT at 532 nm, cloud optical thickness (COT), top and base altitudes of aerosol and cloud layers, cloud-aerosol discrimination (CAD) score, and types of aerosols and clouds are used. The vertical stratification of aerosol and cloud layers can be examined by using these products, because aerosol and cloud layer altitudes are included in these products. The CAD score, in the range between -100 and 100, is the value of quality assurance of discrimination between aerosol and cloud for each layer [*Liu et al*., 2009]. The higher the absolute value of CAD score, the more confident the classification of the feature is. *Liu et al.* [2009] reported that the success ratio of classification of aerosols and clouds is larger than 90% in V2 product and 83% of the classified aerosols and 95% of the classified clouds have absolute values of the CAD score greater than 70. In V3 product, the features tend to have higher and lower CAD scores than V2 product and most of unconfident products can be screened out by rejecting layers with $|CAD| \leq 20$

[*Liu et al*., 2010]. In this study, aerosol and cloud layers are defined when the absolute value of CAD score is higher than 70 for quality assurance of aerosol and cloud data in V2 and V3 products.

For computation of SWDARF from CALIPSO observations, refractive indices and size distributions of the six aerosol types of the CALIPSO aerosol model [*Omar et al*., 2009] and cloud particles (water and ice) are used. Two ice particles, which are randomly and horizontally oriented particles, are included in V3 product. In this study, cloud mean radii for water and ice particles are 8 and 20 μm and ice particles are assumed as spherical particles in radiation calculation. The external mixture is assumed for obtaining the optical cross section of air mass including aerosol and cloud components. SSA of aerosol particles is calculated with reference to refractive indices and size distributions of the CALIPSO aerosol model. Mean radius, geometric standard deviation (GSD), and calculated SSA of each aerosol component are listed in Table 2-2. Values of SSA derived from CALIPSO aerosol model may not be always realistic. For example, the SSA of the clean continental model is smaller than that of the polluted continental model, that is inconsistent with reported ground truth values; that of the mineral dust aerosol model is smaller than recent reported values from passive satellite remote sensing and ground-based measurements [*Kaufman et al.*, 2001; *Dubovik et al.*, 2002; *Yoshida and Murakami*, 2008].

2.2.2 MODIS observations

The lidar beam is completely attenuated by optically thick clouds with COT larger than 3; thus the CALIPSO lidar is unable to detect aerosols and clouds under the cloud top of such an optically dense cloud layer. Instead, I use the COT derived by a passive satellite sensor, i.e., MODIS on Aqua satellite. The MODIS sensor, aboard the NASA Earth Observing System Terra and Aqua satellites, measures radiances in 36 channels including infrared and visible bands with spatial resolution between 250 m and 1 km. MODIS-derived COT in the daily product of Aqua MODIS Collection 5.1 level 3 atmosphere product (MYD08_D3) [*Platnick et al*., 2003; *Hubanks et al*., 2008] is applied to the CALIPSO cloud profile when aerosols exist above clouds (above-cloud case) in radiation calculation from observation (see section 2.4).

Surface albedo is one of important parameters that change the aerosol forcing at TOA [*Nakajima et al*., 2007; *Kim and Ramanathan*, 2008]. The MODIS surface albedo product, MCD43C3, is used in radiative calculation for observation. MODIS provides surface albedo data in 7 narrow bands and in three broad bands (visible, near-infrared, and shortwave). MODIS global albedo data are at a 0.05° by 0.05° spatial resolution

[*Schaaf et al*., 2002; *Roesch et al*., 2004]. The albedo products include black-sky and white-sky albedos for direct and diffuse beam, respectively. Since the MODIS black-sky albedo and white-sky albedo represent the extreme cases under completely direct and completely diffuse illumination, the actual ground albedo can be computed as a function of white-sky and black-sky albedo, solar zenith angle, and AOT [*Yu et al*., 2004; *Satheesh et al*., 2006; *Román et al.*, 2010]. *Yu et al*. [2004] examined the dependence of the clear-sky SWDARF on black-sky and white-sky albedo. Compared with SWDARF estimated by the actual albedo, a simplification of using the white-sky albedo causes an uncertainty that is 5% of estimated SWDARF over land. Therefore, I use the white-sky albedo for clear-sky and cloudy-sky conditions. Surface albedo values for radiation calculation are interpolated from 0.3 to 4.0 μm using 7 narrow bands and visible and near-infrared broadband land surface albedos of the MODIS product. Figure 2-2 shows the annual mean shortwave broadband surface albedos from 2007 to 2009 at 1° by 1°. Over central Eurasia around 50°N and North America, the seasonal variation is large, because of snow covers in winter and spring seasons. The ocean surface albedo is calculated by FSTAR radiation code in using the surface wind velocity of MERRA reanalysis data [*Rienecker et al.*, 2011]. The ocean surface albedo is assumed to be dependent on the surface wind velocity [*Nakajima and Tanaka*, 1983]; the ocean surface albedo decreases with increasing the wind velocity. The surface albedo is about 0.04 over most part of the ocean.

2.2.3 MERRA meteorological data

The Modern Era Retrospective-analysis for Research and Applications (MERRA) is a NASA atmospheric data reanalysis using the Goddard Earth Observing System Model Version 5 (GEOS-5) and Data Assimilation System (DAS) [*Rienecker et al.*, 2011]. MERRA meteorological data product, instM_3d_ana_Np, is used for constructing the model atmosphere (pressure, temperature, specific humidity, and surface wind speed) for radiative transfer computation.

2.3 Radiation code

A radiative transfer code FSTAR5c is a flux version of the System of Transfer of Atmospheric Radiation (STAR) [*Ruggaber et al.*, 1994]. The FSTAR model calculates radiative fluxes with a range from 0.2 to 200 μm using a multi-stream flux approximation under the plane-parallel layers with water vapor and other trace gases, various types of aerosol and cloud polydispersions, and ground/ocean surfaces with radiative transfer algorithms of *Nakajima and Tanaka* [1983, 1986, 1988]

(OpenCLASTR http://ccsr.aori.u-tokyo.ac.jp/~clastr/). We set 4 streams for our calculation.

I performed 40 band calculations from 0.3 to 4 μm for monthly averaged broadband SWDARF. The three-term *k*-distribution method of AFGL/Lowtran [*Kneizys et al.*, 1988] is used for gaseous absorption. This calculation is performed every one hour using solar zenith angles on the 15th of each month. The vertical resolutions of radiation calculation are 0.25 km from ground surface to 5 km altitude, 0.5 km from 5 to 10 km altitude, 1 km from 10 to 25 km altitude, 2.5 km from 25 to 50 km altitude, and 5 km from 50 to 70 km altitude. The observation data is interpolated onto these vertical resolutions in the radiation calculation.

2.4 Method of SWDARF calculation

I investigate four scenarios for evaluating the all-sky SWDARF at TOA using CALIPSO products and data of MODIS sensor. One is clear-sky condition and the others are cloudy-sky conditions.

In clear-sky condition, column AOTs are observed by passive remote sensing and aerosol profiles are most reliably observed by CALIPSO. The first scenario is defined as the clear-sky case.

High cloud reflectance changes the DARF from negative to positive [*Haywood and Shine*, 1997]. Hence, in this study, three scenarios are assumed under cloudy-sky condition: the second scenario is a case of aerosols existing above clouds (above-cloud case), and the third scenario is a case of aerosols existing below high-level clouds such as cirrus (below-cloud case), but with no clouds below the significant aerosol layers. The above-cloud scenario also includes the case of aerosol layers with low-level clouds and high-level clouds existing at the same time, because high-level clouds decrease the absolute value of aerosol radiative effect, but do not change its sign.

Aerosols widely exist from surface to the upper troposphere and are mixed with clouds. Nevertheless, the CALIPSO lidar is unable to detect aerosols under optically thick clouds, because the limitation of optical thickness observed by CALIPSO is about 3. The aerosols undetected by CALIOP sensor exist below/within the optically thick clouds. This case is the fourth scenario, which is defined as the cloudy-undetected scenario. In this study, the DARF of the cloudy-undetected case is assumed to be close to zero, because optically thick clouds significantly scatter the incident sunlight.

The above-mentioned four scenarios are schematically illustrated in Fig. 2-3. The cloudy-sky SWDARF, $SWDARF_{\text{cloudy-sky,}}$ which is the weighted mean of forcings in the above-cloud, below-cloud, and cloudy-undetected cases with weights of occurrence

probabilities for the three cases, is expressed as

$$SWDARF_{cloudy-sky} = \sum_{i=ac,bc,uc} P_i \times SWDARF_i \approx \sum_{i=ac,bc} P_i \times SWDARF_i + 0 = \sum_{i=ac,bc} P_i \times SWDARF_i , \quad (2\text{-}10)$$

where P_{ac} , P_{bc}, and P_{uc} are the occurrence probabilities of above-cloud, below-cloud, and cloudy-undetected cases, respectively:

$$P_{ac} = \frac{N_{ac}}{N_{cloudy-sky}}, \quad P_{bc} = \frac{N_{bc}}{N_{cloudy-sky}}, \quad \text{and} \quad P_{uc} = \frac{N_{cloudy-sky} - N_{ac} - N_{bc}}{N_{cloudy-sky}} , \quad (2\text{-}11)$$

$$P_{ac} + P_{bc} + P_{uc} = 1 , \quad (2\text{-}12)$$

where N_{ac}, N_{bc}, and $N_{\text{cloudy-sky}}$ are the pixel counts of above-cloud, below-cloud, and cloudy-sky cases, respectively. $SWDARF_{ac}$, $SWDARF_{bc}$, and $SWDARF_{uc}$ are SWDARFs of above-cloud, below-cloud, and cloudy-undetected cases, respectively. In this study, $DARF_{uc}$ is assumed as zero, because optically thick clouds dominantly scatter the incident sunlight and the absorption by aerosols that exist within thick clouds cancels aerosol scattering.

The all-sky DARF, $DARF_{\text{all-sky}}$, which is a combination of the clear-sky and cloudy-sky forcings in a similar way to the cloudy-sky forcing calculation:

$$DARF_{\text{all-sky}} = P_{\text{clear-sky}} \times DARF_{\text{clear-sky}} + P_{\text{cloudy-sky}} \times DARF_{\text{cloudy-sky}} , \quad (2\text{-}13)$$

where $P_{\text{clear-sky}}$ is the occurrence probability of clear-sky condition and $P_{\text{cloudy-sky}}$ is that of cloudy-sky condition. Details of this calculation method are described in the Appendix A.

Figure 2-4 shows the occurrence probabilities of four scenarios for CALIPSO V2 and V3 products. The geographical patterns of occurrence probability of four scenarios are similar between V2 and V3 products. The occurrence probability of clear-sky case is high over desert regions and bare ground, for example, Saharan and Arabian deserts, Australia, and South Africa. Because CALIOP can observe optically thin clouds that are undetected in the ISCCP product [*Winker et al.*, 2010], high-level clouds are detected more accurately than by passive remote sensing and thus aerosols existing below clouds tend to be observed around the Intertropical Convergence Zone (ITCZ).

From V2 to V3 product, the occurrence probability of clear-sky case increase and that of above-cloud case decrease, because the cloud clearing and CAD algorithms are improved [*Vaughan et al.*, 2010; *Liu et al*., 2010]. Increase of the occurrence probability

for below-cloud case from V2 to V3 product is mainly caused by the improvement of CAD algorithm. The figure shows that the occurrence probabilities of clear-sky and below-cloud cases in V2 product are smaller than those of V3 product, especially, over the ocean between 40°S and 40°N. The occurrence probability of below-cloud case may be underestimated, because aerosols existing below/within optically thick clouds are undetected by CALIOP.

Aerosols emitted by biomass burning and fossil fuel burning are transported above low-level clouds off southern Africa and South America and over North Pacific. Over land, aerosols existing above clouds are hardly observed, except for East Asia where low-level clouds are frequently formed [*Li et al*., 2004]. The occurrence probability of above-cloud case in V2 product is overestimated, because low-level aerosols are frequently misclassified as clouds by V2 algorithms when aerosols are adjacent to clouds [*Liu et al*., 2010]. The regions where aerosols are observed above clouds are limited over ocean near aerosol source regions in V3 product.

CAD algorithm is improved and aerosols are more frequently detected by V3 algorithms [*Liu et al*., 2010]. As a result, the occurrence probability of cloudy-undetected case becomes smaller from V2 to V3 product. Over the ocean around 60°S, aerosols are hardly observed by CALIOP, because optically thick clouds usually exist.

Figure 2-5 shows the annual mean values of probability occurrences for four scenarios between 60°S and 60°N. The mean value of cloudy-undetected case decreases by 16% from V2 to V3 product. This indicates that 16% of the vertical profiles that clouds are only detected in V2 product change to the profiles that includes also or only aerosols in V3 product. In V3 product, the sum of the mean values of clear-sky, above-cloud, and below-cloud cases is 58%. On the basis of the results of V3 product, 58% of the all-sky SWDARF are calculated by using the observation data in this study.

The procedure of the separation of the above-mentioned four scenarios for CALIPSO data is described below. At first, whether aerosol layers and/or cloud layers exist is examined in each 5 km product. If only aerosol layers exist, this case is defined as the clear-sky scenario. If the base altitude of the lowest aerosol layer is higher than that of the lowest cloud layer, this case is defined as the above-cloud scenario. In this scenario, aerosols usually exist above low-level clouds. If the base altitude of the lowest aerosol layer is lower than that of the lowest cloud layer, this case is defined as the below-cloud scenario. In this scenario, aerosols usually exist below high-level clouds such as cirrus. The mixed layers of aerosols and clouds are included in both above-cloud and below-cloud cases, as understood by the definition of each scenario. Each aerosol layer is classified as one of the six aerosol types and each cloud layer is

classified as water or ice by the CALIPSO algorithms. The randomly oriented and horizontally oriented ice particles are included in V3 product, but ice particles are assumed as spherical particles in this study. The column AOT of the selected aerosol type, COT of the selected cloud type, profile information of aerosols and clouds for each scenario are aggregated and averaged at 1° by 1° horizontal resolution every month from 2007 to 2009.

The AOT above the cloud height of the MODIS product is obtained from the CALIPSO product. MODIS-derived COT, $\tau_{\text{cloud, MODIS}}$, is applied to the CALIPSO cloud profile when aerosols exist above clouds (above-cloud case) in radiation calculation. The monthly mean COT of above-cloud case is estimated using MODIS daily-mean cloud product with reference to *Zhang et al.* [2014]. As illustrated in Fig. 2-6, at first, the monthly mean cloud top pressure (p_{cloud}) and cloud top height (h_{cloud}) of the lowest cloud layer in CALIPSO profile are calculated in above-cloud case. After that, MODIS daily-mean COT of clouds, which have the cloud top pressure higher than p_{cloud}, are averaged. This averaged COT is defined as $\tau_{\text{above-cloud}}$. Similarly, CALIPSO COT, $\tau_{\text{cloud, CAL}}$ is the sum of CALIPSO-derived COTs below h_{cloud}, $\tau_{\text{low-cloud, CAL}}$ and above h_{cloud}, $\tau_{\text{high-cloud, CAL}}$, so that the following relation holds:

$$\tau_{\text{cloud, CAL}} = \tau_{\text{low-cloud, CAL}} + \tau_{\text{high-cloud, CAL}} . \tag{2-14}$$

The vertical profile of extinction coefficient observed by CALIPSO $\sigma_{\text{cloud,CAL}}(z)$ is multiplied by the scaled factor $(\tau_{\text{above-cloud}} - \tau_{\text{high-cloud, CAL}})/\tau_{\text{low-cloud, CAL}}$ below h_{cloud} to obtain the extinction coefficient of clouds in above-cloud case $\sigma_{\text{cloud}}(z)$:

$$\sigma_{\text{cloud}}(z) = \frac{\tau_{\text{above-cloud}} - \tau_{\text{high-cloud, CAL}}}{\tau_{\text{low-cloud, CAL}}} \times \sigma_{\text{cloud, CAL}}(z) . \tag{2-15}$$

Figure 2-7 shows the monthly mean profiles of extinction coefficient for aerosols and clouds retrieved in CALIPSO V3 product in above-cloud case at grid point (5°W, 15°S) in September 2007. The aerosol layer exists from 1.5 to 4.5 km altitude and the cloud layer exists below 1.5 km. The figure shows two cloud profiles of extinction coefficient $\sigma_{\text{cloud,CAL}}$ and σ_{cloud}. The cloud layer exists below 1.5 km altitude and the maximum value of σ becomes about 15 by applying the MODIS COT. Because CALIPSO lidar beam completely attenuates above the bottom height of optically-thick clouds, the bottom height of the cloud layer may be overestimated by the above-mentioned method. Here, however, I do not presume that this overestimation will cause a large error in the evaluated TOA fluxes as far as the values of MODIS COT are suitably retrieved.

2.5 Results

2.5.1 Geographical distributions of AOT and SSA

Figures 2-8 and 2-9 show annual mean distributions of AOT and SSA at 532 nm for clear-sky, above-cloud, below-cloud, and all-sky cases in CALIPSO V2 and V3 products. Annual mean AOTs at 532 nm between 60°S and 60°N for the CALIPSO six aerosol types and for total aerosols in CALIPSO V2 and V3 products are summarized in Table 2-3. AOTs of clear-sky and all-sky cases increase and those of above-cloud and below-cloud cases decrease from V2 to V3 product. The clear-sky AOT becomes larger and the fraction of marine type increases from V2 to V3 product, so that the clear-sky SSA becomes larger over ocean. In above-cloud and below-cloud cases, the smoke and polluted dust types, which are highly absorbing aerosols, are less detected in V3 product, so that AOT becomes smaller and SSA becomes larger from V2 to V3 product. The all-sky AOT is calculated by a combination of AOT and the occurrence probability for each scenario (see Appendix A). Compared with V2 product, the all-sky AOT in V3 product becomes larger, because the clear-sky AOT and the occurrence probabilities of clear-sky and below-cloud cases increase.

AOT in below-cloud case is obviously larger than that of clear-sky case in CALIPSO products. I can raise two possible reasons why the below-cloud AOT is larger than the clear-sky AOT. One is aerosol particle growth in a high relative humidity in the cloudy-sky condition to increase AOT. The other is retrieval errors propagated downward from the upper cloud layers. The lower part of the profile always has higher uncertainty and contains more retrieval artifacts in satellite lidar retrievals [*Winker et al*., 2013]. The reason of the larger below-cloud AOT should be studied more carefully in future.

2.5.2 Vertical profiles of aerosols and clouds

Figures 2-11, 2-12, and 2-13 show the seasonal mean extinction profiles for aerosols and clouds of CALIPSO V2 and V3 products in clear-sky, above-cloud, and below-cloud cases in three selected areas illustrated in Fig. 2-10. MODIS COT is applied to the cloud profile of CALIPSO in above-cloud case (see section 2.4).

In clear-sky condition, the aerosol profiles are very similar in V2 and V3 products. Off southern Africa, aerosols emitted from biomass burning in central Africa are transported to the Atlantic Ocean and aerosol layers are detected up to 4 km altitude throughout the year. Over the North Pacific Ocean, industrial aerosols and Asian dust are transported to the North Pacific in the boreal spring and summer seasons, while

aerosols are suppressed below 2 km altitude in the boreal autumn and winter seasons. Over the central Pacific, maritime aerosols are dominantly distributed below 2 km altitude throughout the year.

In above-cloud case, the aerosol extinction coefficient is smaller than those of clear-sky and below-cloud cases. In addition, the aerosol extinction coefficient of V3 product is smaller than that of V2 product, especially below 2 km altitude, because the cloud clearing and CAD algorithms are improved [*Vaughan et al.*, 2010; *Liu et al.*, 2010]. Though either aerosol or cloud is classified at each vertical bin in the profile of single shot, aerosols seem to exist within the clouds as shown in Fig. 2-12 by the temporal and spatial averaging procedure. Compared with V2 product, the optically thin high-level aerosols are more detected and the cloud extinction coefficient at high altitude is larger in V3 product. Off southern Africa, the top altitude of the aerosol layer is similar to that of clear-sky case, but the aerosol extinction is smaller than the clear-sky condition. Over the North Pacific, the low-level clouds exist and aerosol layers below 2 km are hardly detected. Over the Central Pacific, the elevated aerosol layers rarely observed and the heights of aerosol and cloud layers are different in each event; thus, the cloud extinction coefficient is larger than those over the North Pacific and off southern Africa above 3 km altitude.

In below-cloud case, the extinction coefficients of aerosols and clouds in V3 product are smaller than those of V2 product, in particular, at the height where aerosols and clouds are overlapped in V2 product. The column AOT and COT decrease by 80% and 36%, respectively (Figs. 2-8 and 2-14 and Table 2-5), due to the improvement of the cloud-aerosol discrimination algorithms [*Liu et al.*, 2010]. Off southern Africa and over the central Pacific, the aerosol extinction coefficient is similar to that of clear-sky condition and two cloud layers are detected below 2 km and above 4 km altitude. On the other hand, aerosol layers are vertically spread and the aerosol extinction coefficient is higher than that of the clear-sky case over the North Pacific. This suggests that it is difficult to classify aerosol and cloud layers correctly in case that aerosol and cloud layers exist in the near distance.

2.5.3 Shortwave direct aerosol radiative forcing

Figure 2-15 shows the annual mean distribution of SWDARF in clear-sky, above-cloud, and below-cloud cases, derived from for CALIPSO V2 and V3 products. The magnitude and sign of SWDARF is determined not only by AOT but also by SSA, asymmetry factor, and underlying surface albedo [*Fraser and Kaufman*, 1985; *Nakajima et al.*, 2007]. On the other hand, the absolute value of SWDARF is

approximately proportional to AOT, so that the following radiative forcing efficiency (RFE), β, is defined to scale out the AOT dependence:

$$\beta = \frac{SWDARF}{\tau}, \quad (2\text{-}16)$$

where τ is AOT. Figure 2-16 shows annual mean distributions of the radiative forcing efficiency in clear-sky, above-cloud, and below-cloud cases in the zonal regions from 60°S to 60°N for CALIPSO V2 and V3 products.

In clear-sky condition, aerosols cause a negative forcing, except for Saharan and Arabian deserts where the SWDARF is positive value of about +3 Wm^{-2} due to the high surface albedo of 0.3 and low SSA of 0.9. In winter and spring seasons, the ground surface is covered by snow over Russia, United States, and Canada, so that the SWDARF takes a small positive value due to the high surface albedo of snow and ice surface. Over ocean, AOT, SSA, and RFE become larger from V2 to V3 product because of the larger AOT of marine type aerosol. Desert dust is transported over the ocean around Saharan and Arabian deserts and industrial aerosols emitted from East Asia are transported to the North Pacific; therefore, SSA and RFE in these regions are lower than those of other ocean areas. The RFE over land is relatively smaller than that over ocean, because the ground albedo is higher than the ocean albedo.

It is found that the above-cloud SWDARF is positive over most parts of the globe. This point is important to be recognized, because previous studies only reported that the absorbing aerosols above low-level clouds have a positive SWDARF off southern Africa [*Keil and Haywood*, 2003; *Chand et al*., 2009; *De Graaf et al.*, 2012]. As for the contrast of land and ocean, the figure shows SWDARF takes a positive value over land larger than that of over ocean, because AOT is larger near source regions than over the remote oceans. It should be noted, however, that the occurrence probability is less than 5% in most parts of the land. Consequently, the positive SWDARF of above-cloud case has small effect on the estimation of the cloudy-sky and all-sky SWDARFs, except for regions of Atlantic Ocean off southern Africa, East Asia, and North Pacific. In these regions, aerosols emitted from biomass burning and air pollution are loaded above or within the low-level clouds (Fig. 2-12) and absorb the light scattered by clouds [*Haywood and Shine*, 1997; *Takemura et al*., 2005]. The SWDARF value is especially large over East Asia, because aerosol absorption due to higher AOT and COT than those off southern Africa and over the North Pacific. Off Saharan and Arabian deserts, SWDARF shows negative forcing, because COT is less than 5 and aerosol absorption is not enough to change the sign of the forcing from negative to positive. In V3 product, SWDARF is negative over the Central Pacific. This is because SSA of aerosols is more

than 0.95 in this region, so that the aerosol absorption effect is smaller than the scattering effect despite an increase of aerosol absorption by lower clouds. The AOT is overestimated in V2 product, so that the SWDARF in V2 product is more positive than that of V3 product, but the above-cloud RFE in V2 product is less positive than V3 product except for the Central Pacific. This can be explained by the fact that aerosols are less detected below 2 km altitude and are likely to exist above low-level clouds in V3 product (Fig. 2-12). The light absorption of aerosols above clouds is larger than that of aerosols within clouds, so that the RFE of V3 product is larger than that of V2 product.

In below-cloud case, the geographical pattern of SWDARF is similar to that of the clear-sky SWDARF. It is important to find that the below-cloud SWDARF is larger than the clear-sky SWDARF, because the below-cloud AOT is over 1.5 times larger than the clear-sky AOT (Fig. 2-8 and Table 2-3). The magnitude of below-cloud RFE is smaller than that of the clear-sky RFE, regardless of the sign of SWDARF. High-level clouds attenuate the incoming sunlight and suppress the light scattering by the lower aerosol layers, so that the radiative effects aerosols lower than the high-level cloud layer are smaller than the clear-sky situation. In V2 product, AOT and COT are overestimated in below-cloud case; thus, the SWDARF is more negative than that of V3 product because of the overestimation of AOT, but the negative RFE is smaller than that of V3 product because of the overestimation of COT.

CALIPSO only retrieves COT less than about 3; thus, the situation where the COT is larger than 3 is classified as the cloudy-undetected case in our study. On the other hand, aerosols are easily detected below optically thin cloud layers with COT lower than 1, so that there is a tendency that the occurrence probability of below-cloud case is higher at low latitudes than at high latitudes (Figs. 2-4 and 2-14).

Figure 2-17 shows annual mean distributions of the cloudy-sky and all-sky SWDARFs. The cloudy-sky SWDARF becomes more negative from V2 to V3 product, because the occurrence probability of above-cloud case decreases and that of below-cloud case increases (Figs. 2-4 and 2-5). In particular, SWDARF takes considerably large negative values in the regions where the occurrence probability of above-cloud case is overestimated in V2 product, such as off Africa, off Arabia, and the central Pacific. From V2 to V3 product, the sign of the cloudy-sky SWDARF changes from positive to negative over India, southern Africa, South America, and Europe. In V3 product, the cloudy-sky SWDARF is still positive in the source and outflow regions of smoke emitted from biomass burning and air pollution. Carbonaceous and dust aerosols emitted from East Asia cause a large positive forcing throughout the year. In particular,

they are transported to the North Pacific and produce a positive forcing.

Under all-sky condition, the SWDARF is negative over ocean, except for outflow regions of smoke aerosols where SWDARF is almost zero in V3 product. The effect of light absorption over the desert regions is caused by the high surface albedo of 0.3 and low SSA of 0.9, regardless of cloud fraction. Similarly, the all-sky SWDARF is slightly positive in the regions, where the ground covered by snow for more than half a year, i.e., Canada, Russia, and the Himalaya Mountains. In comparison with V2 product, the all-sky SWDARF of V3 product is more negative, because the SWDARF and occurrence probability of clear-sky case are larger and the above-cloud case is more limited over the ocean around aerosol source regions. In particular, the all-sky SWDARF changes from +1 Wm^{-2} to zero off southern Africa and over the North Pacific. These results indicate that the all-sky forcing largely depends not only on the column cloud fraction but also on the occurrence probabilities of clear-sky, above-cloud, and below-cloud cases.

2.5.4 Sensitivity tests of SWDARF

The sensitivity tests are performed to estimate the uncertainties of the estimated SWDARFs caused by the following two factors.

Previous studies reported that absorbing aerosols above clouds bias the cloud satellite retrievals to less COT and smaller effective radius [*Haywood et al*., 2004; *Coddington et al*., 2010]. Recent studies corrected the underestimation of the cloud reflectance caused by above-cloud absorbing aerosols and estimated more positive SWDARF in above-cloud case than SWDARF estimated by the radiative calculation using uncorrected COT off southern Africa [*Meyer et al*., 2013; *Zhang et al*., 2014]. *Coddington et al*. [2010] indicated that MODIS COT is underestimated by 4 as a result of comparison with the aircraft observation. This is the first uncertainty for estimating SWDARF; thus, the sensitivity tests that add COT increments of 0, 1, 3, and 5 to $\tau_{\text{above-cloud}}$ (4 patterns) are performed.

In this study, SWDARF of cloudy-undetected case is assumed to be zero. This is the second uncertainty for estimating SWDARF under cloudy-sky and all-sky conditions. Figure 2-18 shows SWDARFs for the CALIPSO six aerosol types depending on COT when aerosols exist from 0 to 3 km altitude and clouds exist from 1 to 5 km altitude, which is classified as cloudy-undetected case in this study. The SWDARFs are different values that depend on aerosol types and become more positive with increasing COT. The zonal mean values between 60°S and 60°N of MODIS COT is 14.7 and the mean SWDARF of the six aerosol types is –0.09 Wm^{-2} when COT is equal to 15. From these

results, the SWDARF of cloudy-undetected case is estimated to be within the range of ±0.5 Wm^{-2}. I, therefore, calculate the cloudy-sky and all-sky SWDARFs when the SWDARF of cloudy-undetected case is 0, ±0.25, and ±0.5 Wm^{-2} (5 patterns).

I perform totally 20-pattern calculations for the COT underestimation (4 patterns) and uncertainties of the cloudy-undetected SWDARF (5 patterns). Figure 2-19 shows annual mean distributions of SWDARFs in above-cloud, cloudy-sky, and all-sky cases for the average of 20-pattern calculations in the sensitivity tests. In comparison with the standard results in Figs. 2-15 and 2-17, the sign of SWDARF changes from negative to positive off Arabia and Saharan deserts in above-cloud case, because COT becomes larger and aerosol absorption is enhanced by higher albedo of low-level clouds. Over the Pacific off South America, AOT is lower than 0.03 and SSA is higher than 0.96 in above-cloud case. As a result, SWDARF is close to zero and does not depend on COT of cloud lowers than aerosol layers in above-cloud case. On the other hand, there are no large differences between the results of sensitivity tests and the standard results under cloudy-sky and all-sky conditions.

The annual mean SWDARFs between 60°S and 60°N for above-cloud, cloudy-sky, and all-sky cases in the sensitivity tests are +3.3±0.5, –1.0±0.2, and –2.0±0.2 Wm^{-2}. The errors are represented by standard deviations of the 20-pattern calculations. The underestimation of COT in above-cloud case and the uncertainties of cloudy-undetected SWDARF cause errors of 0.2 Wm^{-2} in the estimation of the cloudy-sky and all-sky SWDARFs, which is smaller than the error of the above-cloud SWDARF. In above-cloud case, the occurrence probability of above-cloud case is low and there are few samples except for off Africa and South America and over the Pacific and East Asia, so that SWDARF depends on few observation data of the vertical distributions of aerosols and clouds and the error of SWDARF is large.

2.5.5 SWDARF of fine mode and anthropogenic aerosols

There are many studies that estimated DARF of anthropogenic aerosols by model simulation [e.g., *Myhre et al.*, 2013], but on the other hand, there are very few observational evaluation of DARF caused by anthropogenic aerosols. This is because aerosols are not retrieved in cloudy-sky condition by the passive satellite sensing and also it is difficult to separate anthropogenic aerosols from natural aerosols from satellite observation. There is one approach to use fine mode aerosols which include most of anthropogenic aerosols. Recently, AOT of fine mode aerosols has been retrieved by the satellite-based MODIS sensor [*Levy et al.*, 2007, 2010]. and *Bellouin et al*. [2008] assumed an anthropogenic fraction of AOT, F_{anth}, which is the ratio of AOT for

anthropogenic aerosols, AOT_{anth}, to AOT for the total aerosols, AOT_{total}, for estimating the anthropogenic AOT and SWDARF. The SWDARF of anthropogenic aerosols estimated by the observation-based method is more negative than those estimated by models [*Bellouin et al*., 2008; *Myhre, 2009*].

I calculate SWDARF for fine mode and anthropogenic aerosols using CALIPSO V3 product by the same calculation method of SWDARF for the total aerosols (see section 2.4). Table 2-4 shows the fine mode fraction of AOT (FMF) at 532 nm for the CALIPSO six aerosol types. FMF is the fraction of AOT for fine mode aerosols to that for the total (fine and coarse mode) aerosols. FMFs for the CALIPSO six aerosol types are calculated using refractive indices and size distributions of the CALIOP aerosol models [*Omar et al*., 2009]. CALIPSO smoke and polluted continental types are dominated by fine mode aerosols, so that the value of FMF is high, while CALIPSO marine and clean continental types are dominated by coarse mode aerosols and FMF is low.

The anthropogenic fraction of AOT, F_{anth}, is then given as

$$F_{anth} = \frac{AOT_{anth}}{AOT_{total}}. \tag{2-17}$$

According to the AeroCom model comparison of aerosol transport models, the mean value of F_{anth} is 24 % [*Myhre et al.*, 2013]. I estimate AOT_{anth} using this value of F_{anth} and FMF and AOT_{fine}:

$$\begin{aligned} AOT_{anth} &= F_{anth} \times AOT_{total} = f_{af} \times AOT_{fine} \\ &= f_{af} \times FMF \times AOT_{total} \end{aligned}, \tag{2-18}$$

where f_{af} is the ratio of AOT_{anth} to AOT_{fine}. The zonal mean values between 60°S and 60°N of AOT_{fine}, FMF, and f_{af} are 0.043, 0.5, and 0.49, respectively.

Figure 2-20 shows annual mean distributions of SWDARF and AOT and SSA at 532 nm for fine mode aerosols and anthropogenic aerosols. SSAs of fine mode aerosols and anthropogenic aerosols are same, because AOT_{anth} is defined by AOT_{fine} and f_{af} and the fraction of the CALIPSO six aerosol types for anthropogenic aerosols is same as that for fine mode aerosols. The regions of large AOT for fine mode aerosols are limited around aerosol sources over land and AOT is less than 0.03 over the Pacific. Over ocean, AOT and SSA are small compared to those of the total aerosols (Figs. 2-8 and 2-9), because marine type aerosol, which is non light-absorbing particle with SSA larger than 0.99, almost consists of coarse mode particles. Over land, SSA of fine mode aerosols is higher than that of total aerosols (Fig. 2-9), because the absorption of fine mode aerosols is weaker than that of total aerosols, which include fine and coarse mode

particles. SWDARF is negative in all regions under clear-sky and all-sky conditions. Over Saharan and Arabian deserts, SWDARF of total aerosols is positive under clear-sky and all-sky conditions, while that of fine mode aerosols is negative, because SSA of fine-mode aerosols is 0.95. The zonal average values between 60°S and 60°N of the all-sky SWDARF for fine mode aerosols and anthropogenic aerosols are –1.19 and –0.57 Wm^{-2}, respectively. It is found that our estimated anthropogenic SWDARF is more negative than the AeroCom model mean value of –0.22 Wm^{-2} [*Schulz et al.*, 2006].

2.6 Summary of SWDARF from satellite observation

Aerosol observation by passive remote sensing is limited in clear-sky condition, so that SWDARFs in above-cloud and below-cloud cases have never been estimated in the global scale. On the other hand, CALIOP lidar system can observe aerosols in clear-sky, above-cloud, and below-cloud cases. In this study, the global scale estimation of the cloudy-sky SWDARF is performed by using observation data for the first time.

Table 2-5 shows annual mean values in the latitudinal area from 60°S to 60°N of occurrence probability, AOT, SSA of aerosols, COT, and SWDARF from CALIPSO V2 and V3 products. For the improvement of cloud clearing and CAD processes from V2 to V3 algorithm [*Vaughan et al.*, 2010; *Liu et al.*, 2010], the occurrence probabilities for the four scenarios of this study are changed. The occurrence probabilities in clear-sky, above-cloud, below-cloud, and cloudy-undetected cases are found to be 38%, 4%, 16%, and 42%, respectively, from the CALIPSO V3 product. CALIOP observes aerosols in clear-sky, above-cloud, and below-cloud cases, which are 58% of aerosols in all-sky condition.

For the improvement of the retrieval algorithms, the distributions of aerosols and clouds are changed from V2 to V3 product. In clear-sky case, V3 AOT is larger than V2 AOT, due to the effects of base extension procedure for the lowest aerosol layer in V3 algorithms [*Vaughan et al.*, 2010]. In clear-sky case, marine aerosols are more classified in V3 product (Table 2-3); thus, V3 SSA is larger than V2 SSA. For these two reasons, V3 SWDARF is more negative than V2 SWDARF in clear-sky case.

For the improvement of cloud clearing and CAD processes from V2 to V3 algorithm [*Vaughan et al.*, 2010; *Liu et al.*, 2010], AOT becomes smaller than V2 product in above-cloud and below-cloud cases. As a result, SWDARF in above-cloud case becomes smaller positive and that in below-cloud case becomes smaller negative from V2 to V3 product. The cloudy-sky SWDARF becomes more negative, because the occurrence probability of below-cloud case increases and those of above-cloud and

cloudy-undetected cases decrease.

According to the sensitivity test of V3 product for the underestimation of COT in above-cloud case and the uncertainties of cloudy-undetected SWDARF, the errors of cloudy-sky and all-sky SWDARF are 0.2 Wm^{-2}, which is smaller than the difference between V3 and V2 SWDARFs. Through this sensitivity test, I found that the uncertainty caused by the difference in the version of lidar retrieval algorithms is larger than the other uncertainties. For these reasons, the retrieval errors are considered to be the main errors in the estimation of SWDARF. In my CALIPSO data analysis, the clear-sky, cloudy-sky, and all-sky SWDARFs are estimated as -3.7 ± 0.8, -1.0 ± 0.8, and -2.0 ± 1.2 Wm^{-2}.

CALIPSO observation is the first global lidar observation and the retrieval algorithms are still in a development phase, so that I should note even the version 3 product still needs more validations and comparison studies. This is my motivation of the present study.

Table 2-1. The lidar ratio S_p for each aerosol and cloud types in the CALIPSO retrievals [*Omar et al.,* 2009; *Winker et al*., 2009].

	Marine	Dust	Polluted continental	Clean continental	Polluted dust	Smoke	Water	Ice
S_p	20	40	70	35	65	70	18	25

Table 2-2. Mean radius, geometric standard deviation (GSD), and single scattering albedo (SSA) at 532 nm of the CALIPSO aerosol model. The size distribution of the CALIPSO model is the bimodal lognormal size distribution, which has fine mode (f) and coarse mode (c) [*Omar et al.,* 2009].

	Mean Radius (μm)	GSD	SSA (532 nm)
Dust	0.1165 (f)	1.4813 (f)	0.92
	2.8329 (c)	1.9078 (c)	
Smoke	0.1436 (f)	1.5624 (f)	0.83
	3.726 (c)	2.1426 (c)	
Clean	0.20556 (f)	1.61 (f)	0.90
Continental	2.6334 (c)	1.8987 (c)	
Polluted	0.1577 (f)	1.5257 (f)	0.93
Continental	3.547 (c)	2.065 (c)	
Clean Marine	0.150 (f)	1.600 (f)	0.99
	1.216 (c)	1.600 (c)	
Polluted Dust	0.1265 (f)	1.5112 (f)	0.85
	3.1617 (c)	1.9942 (c)	

Table 2-3. Annual mean AOTs at 532 nm between 60°S and 60°N for the CALIPSO six aerosol types and total aerosols in CALIPSO Version 2 and Version 3 products.

	Marine	Dust	Polluted continental	Clean continental	Polluted dust	Smoke	Total
Version 2							
Clear-sky	0.019	0.024	0.005	0.002	0.037	0.017	0.106
Above-cloud	0.016	0.045	0.004	0.005	0.061	0.051	0.182
Below-cloud	0.066	0.062	0.014	0.004	0.131	0.070	0.351
Version 3							
Clear-sky	0.039	0.026	0.009	0.002	0.035	0.015	0.127
Above-cloud	0.012	0.034	0.003	0.004	0.033	0.029	0.116
Below-cloud	0.047	0.041	0.012	0.003	0.061	0.027	0.194

Table 2-4. Fine mode fraction of AOT (FMF) at 532 nm for the CALIPSO six aerosol types [*Omar et al*., 2009]. FMF is the fraction of AOT for fine mode aerosols to total (fine and coarse mode) aerosols.

	Marine	Dust	Polluted continental	Clean continental	Polluted dust	Smoke
FMF	0.058	0.527	0.890	0.244	0.666	0.836

Table 2-5. Annual mean values of parameters between 60°S and 60°N for the CALIPSO Version 2 (V2) and Version 3 (V3) products: the occurrence probability, AOT at 532 nm, SSA at 532 nm, COT, and SWDARF [Wm^{-2}] in clear-sky, above-cloud, below-cloud, cloudy-sky, and all-sky cases. In Version 3 product, SWDARF(std) is SWDARF of the standard results, SWDARF(ave) is the average of SWDARF for sensitivity tests and △SWDARF is the difference between V3 SWDARF(ave) and V2 SWDARF.

	Clear-sky	Above-cloud	Below-cloud	Cloudy-undetected	Cloudy-sky	All-sky
Version 2						
Occurrence probability	0.23	0.10	0.10	0.58	0.77	1
AOT (532nm)	0.106	0.182	0.351	-	0.065	0.073
SSA (532nm)	0.90	0.88	0.89	-	0.89	0.89
COT	-	10.12	0.71	-	-	-
SWDARF	-2.9	+4.0	-5.3	0	-0.2	-0.8
Version 3						
Occurrence Probability	0.38	0.04	0.16	0.42	0.62	1
AOT (532nm)	0.127	0.116	0.194	-	0.065	0.086
SSA (532nm)	0.93	0.89	0.91	-	0.91	0.92
COT	-	10.85	0.53	-	-	-
SWDARF(std)	-3.7	+2.6	-4.2	0	-1.1	-2.0
SWDARF(ave)	-3.7	+3.3±0.5	-4.2	0	-1.0±0.2	-2.0±0.2
△SWDARF	0.8	0.7	1.1	0	0.8	1.2

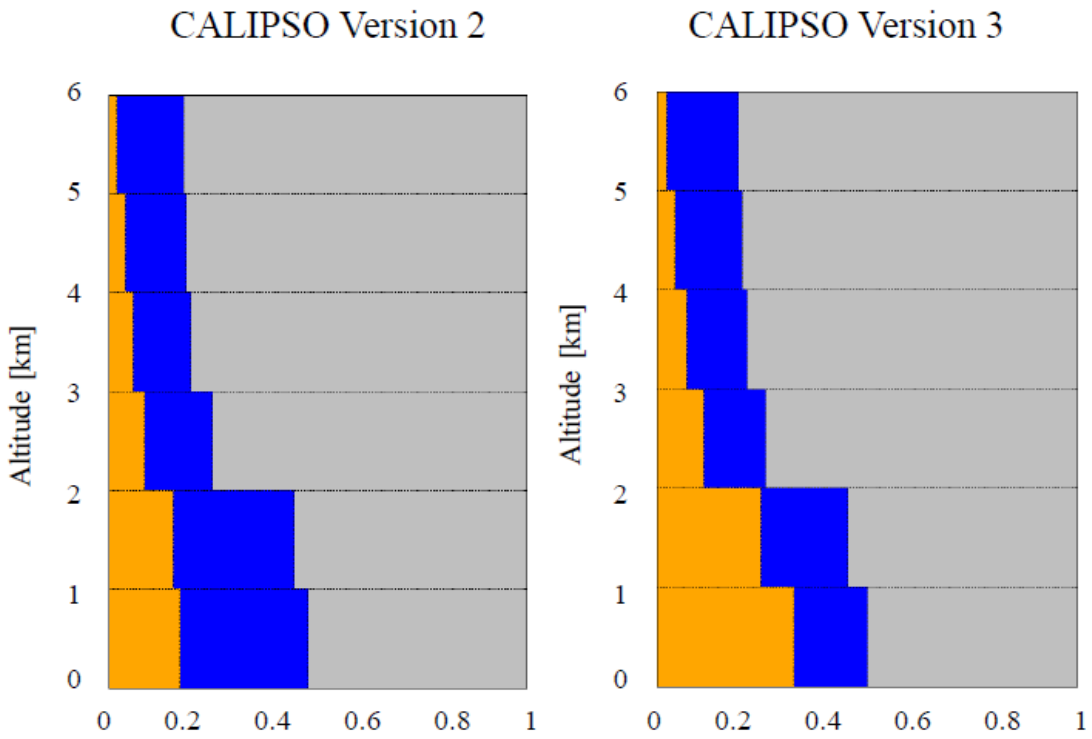

Fig. 2-1. The fraction of aerosols (orange), clouds (blue), and others (gray) from 2007 to 2009 identified in the CALIPSO Version 2 and Version 3 products. The fraction is shown at 1 km vertical bin from surface to 6 km altitude. The feature of "others" consists of clean air, low-confident aerosols and clouds, the non-retrieved data, etc.

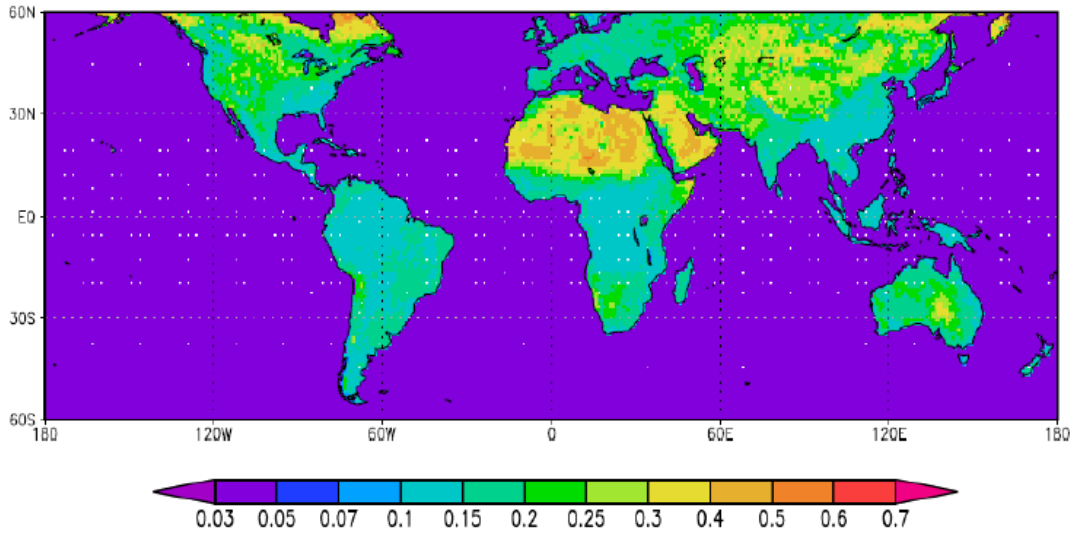

Fig. 2-2. Annual mean distributions of the MODIS land surface albedo and sea surface albedo at 1 by 1 degrees. Sea surface albedo is calculated by the FSTAR radiation code using MERRA surface wind velocity.

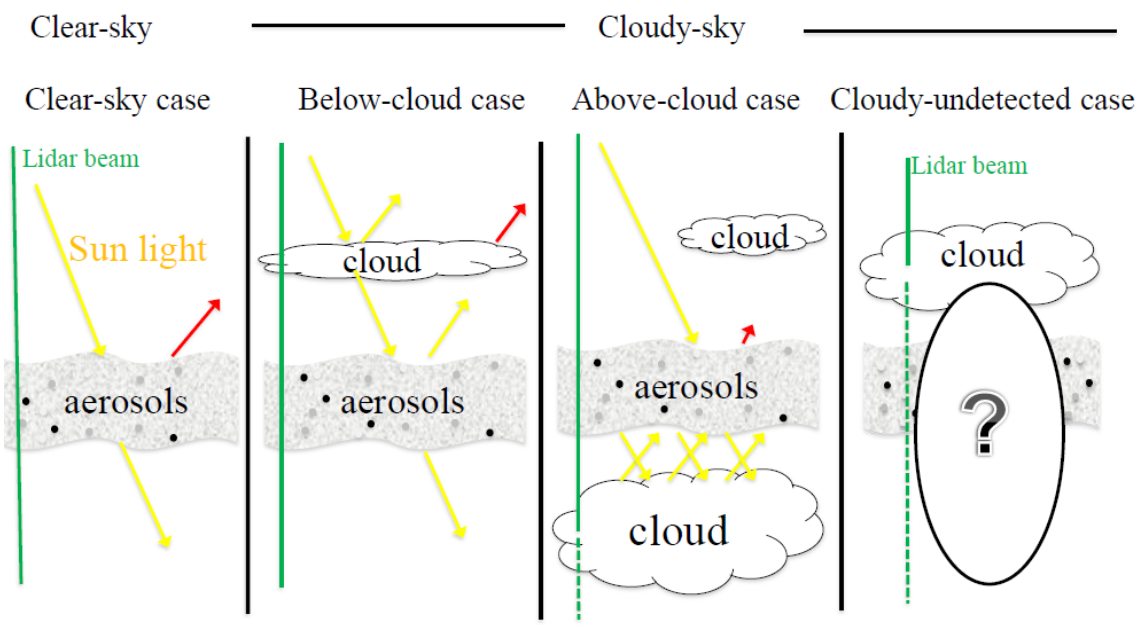

Fig. 2-3. Four scenarios for radiation calculation: clear-sky (left) and cloudy-sky conditions with cases of aerosols below high clouds such as cirrus but without clouds below the aerosol layers (left-middle), aerosols existing above clouds (right-middle), and aerosols not observed in cloudy-sky condition (right). The above-cloud case is the case that aerosols exist above low-level clouds, with or without high-level clouds. The cloudy-undetected case is the case that aerosols, which exist below or within optically thick clouds, are not detected by the satellite lidar.

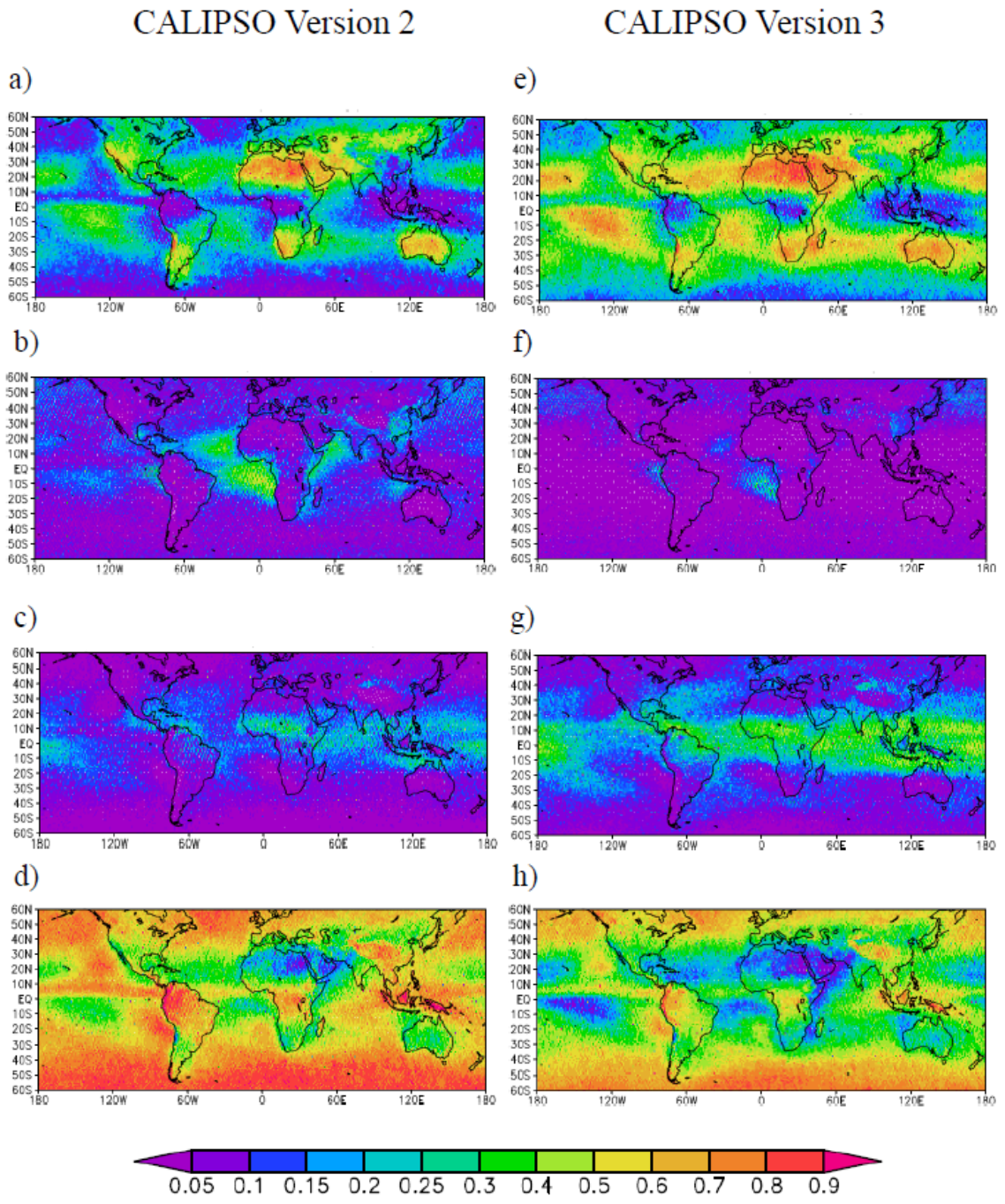

Fig. 2-4. Annual mean distributions of the occurrence probabilities for four scenarios (clear-sky (a, e), above-cloud (b, f), below-cloud (c, g), and cloudy-undetected cases (d, h)). The occurrence probabilities of CALIPSO Version 2 (left) and Version 3 (right) products.

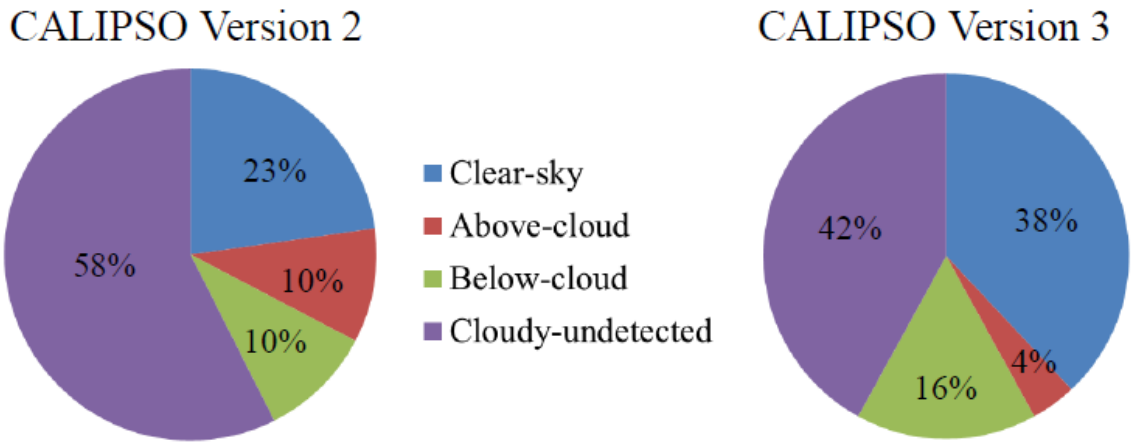

Fig. 2-5. The rate of the ocurrence probabilities for four scenarios (clear-sky, above-cloud, below-cloud, and cloudy-undetected cases) of CALIPSO Version 2 (left) and Version 3 (right) products.

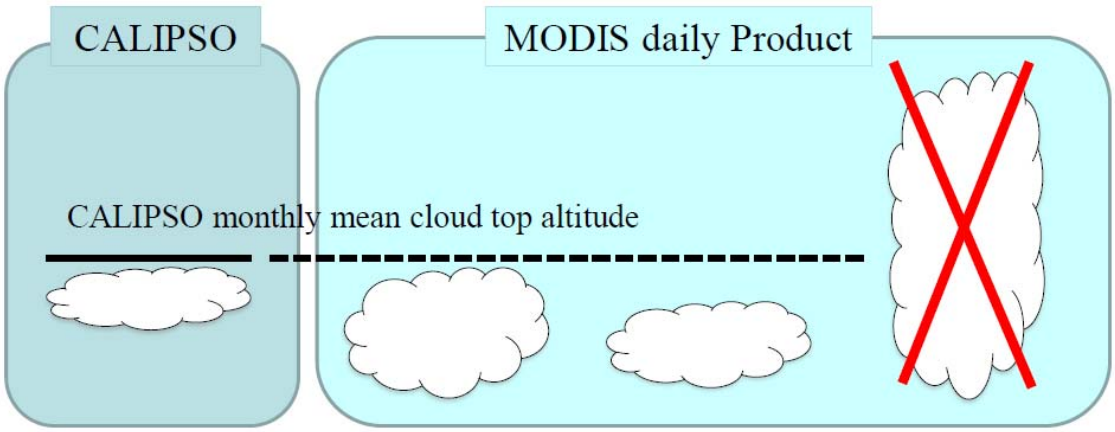

Fig. 2-6. An image of the application methodology to determine cloud optical thickness lower than the CALIPSO cloud top altitude of the lowest cloud layer in order to exclude optically thick high clouds, such as stratocumulus.

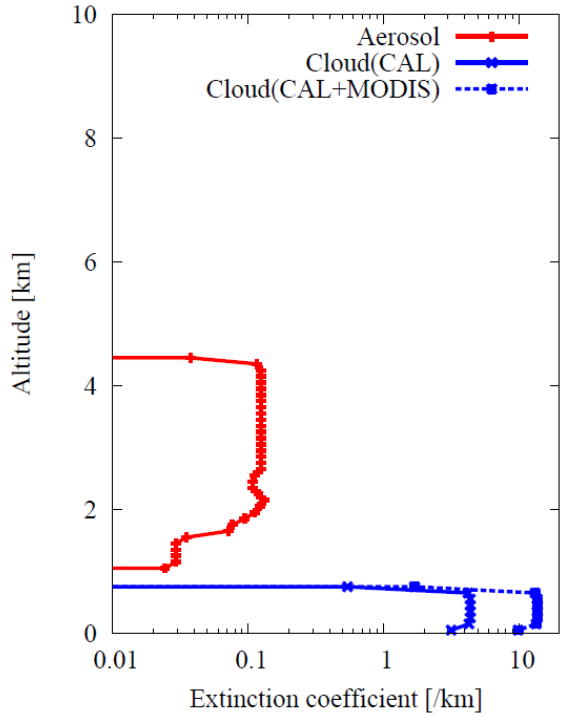

Fig. 2-7. The monthly mean profiles of extinction coefficients for aerosols and clouds retrieved in CALIPSO Version 3 product in above-cloud case at grid point (4.5°W, 15.5°S) in September 2007. Two cloud profiles are shown; one is CALIPSO observed profile and the other is the CALIPSO profile applied with MODIS COT. The *x*-axis shows the logarithmic scale of the extinction coefficient [km^{-1}] and the *y*-axis shows the altitude [km].

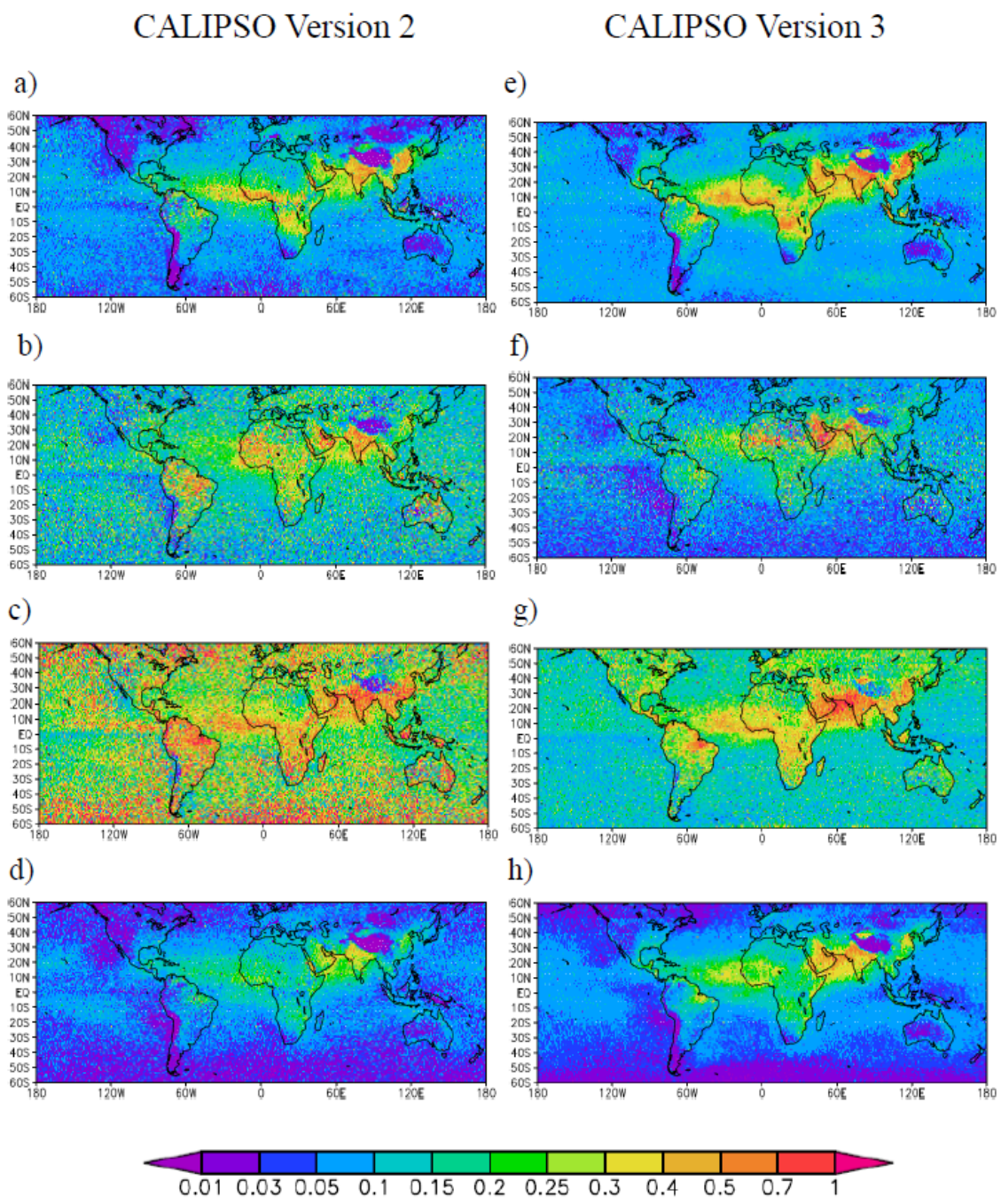

Fig. 2-8. Annual mean distributions of AOT at 532 nm for clear-sky (a, e), above-cloud (b, f), below-cloud (c, g), and all-sky (d, h) cases for CALIPSO Version 2 (left) and Version 3 (right) products.

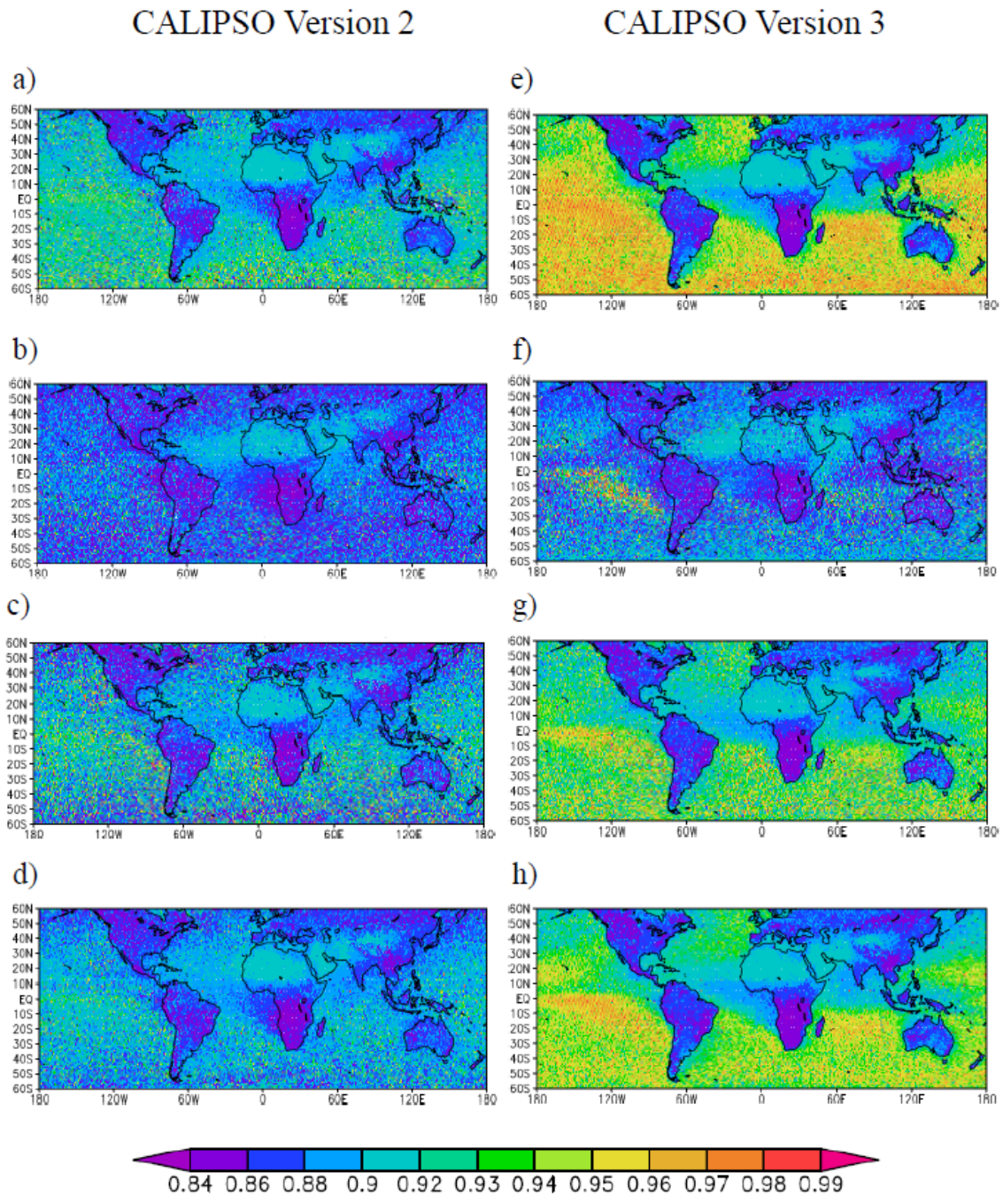

Fig. 2-9. Annual mean distributions of the single scattering albedo (SSA) for aerosols at 532 nm for the clear-sky (a, e), above-cloud (b, f), below-cloud (c, g), and all-sky (d, h) cases for CALIPSO Version 2 (left) and Version 3 (right) products.

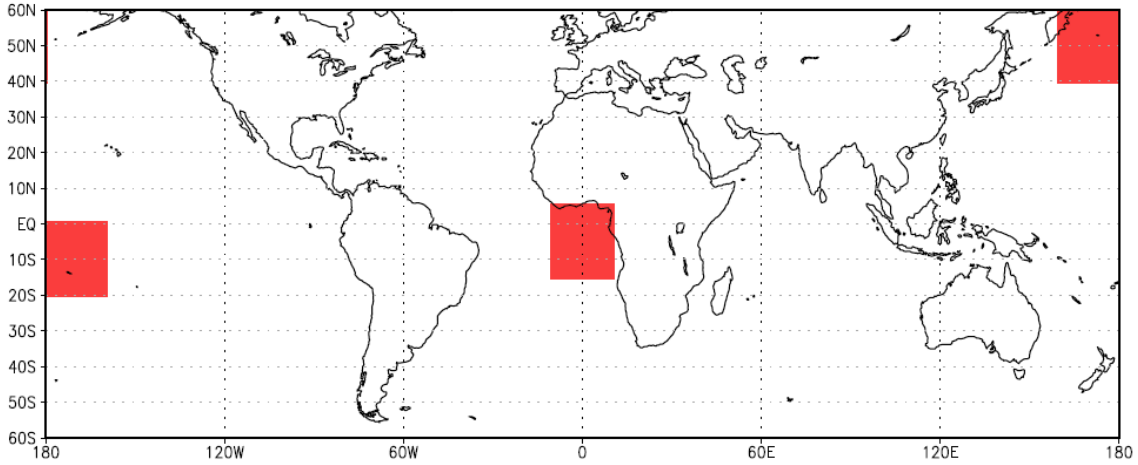

Fig. 2-10. Illustration of three sections selected for the comparison of the aerosol and cloud profiles in clear-sky, above-cloud, and below-cloud cases. One section at red grid box covers 20° by 20°, and the seasonal mean profiles of aerosols and clouds are averaged in these regions.

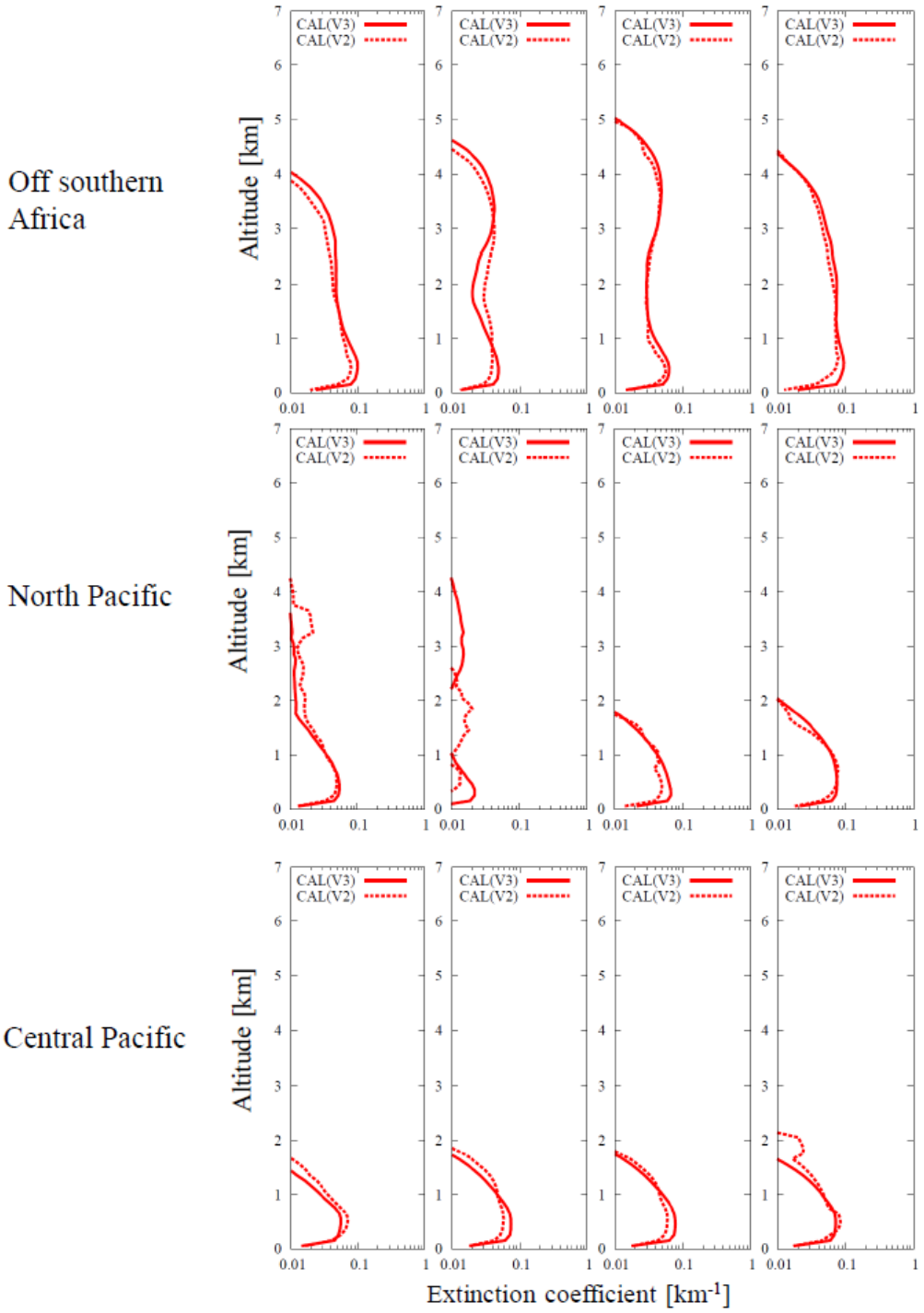

Fig. 2-11. The seasonal mean extinction profiles for aerosols of CALIPSO Version 2 (dashed line) and Version 3 (solid line) products in clear-sky condition. These profiles are averaged in the three sections of Fig. 2-10 and in the seasons (boreal spring (left), summer (left-middle), autumn (right-middle), and winter (right)). The *x*-axis shows the logarithmic scale of the extinction coefficient [km^{-1}] and the *y*-axis shows the altitude [km].

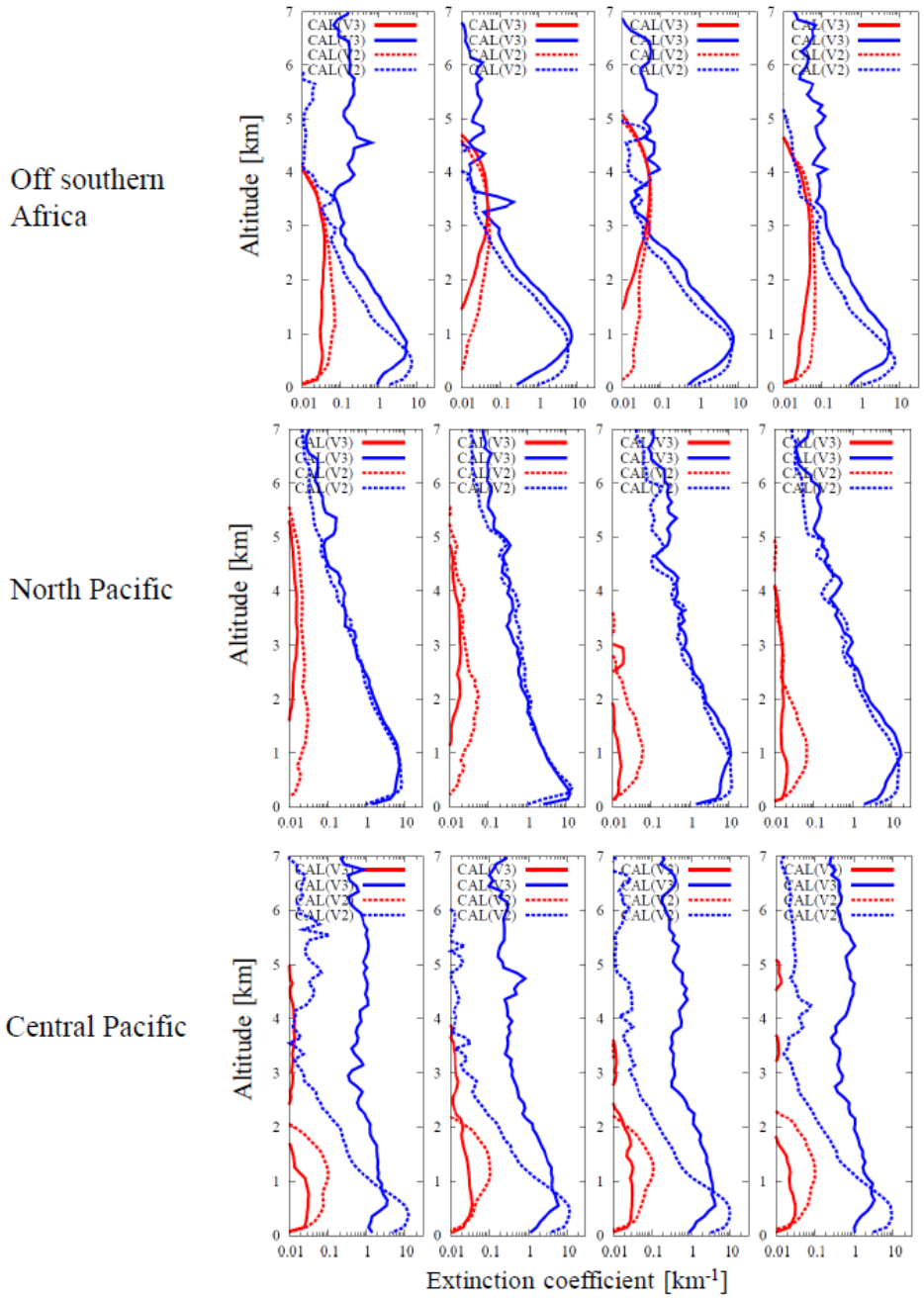

Fig. 2-12. Same as Fig. 2-11, but the seasonal mean extinction profiles for aerosols (red) and clouds (blue) in above-cloud case. MODIS COT is applied for the cloud profile of CALIOP in above-cloud case (see section 2.4). The range of *x*-axis is from 0.01 to 30 [km^{-1}].

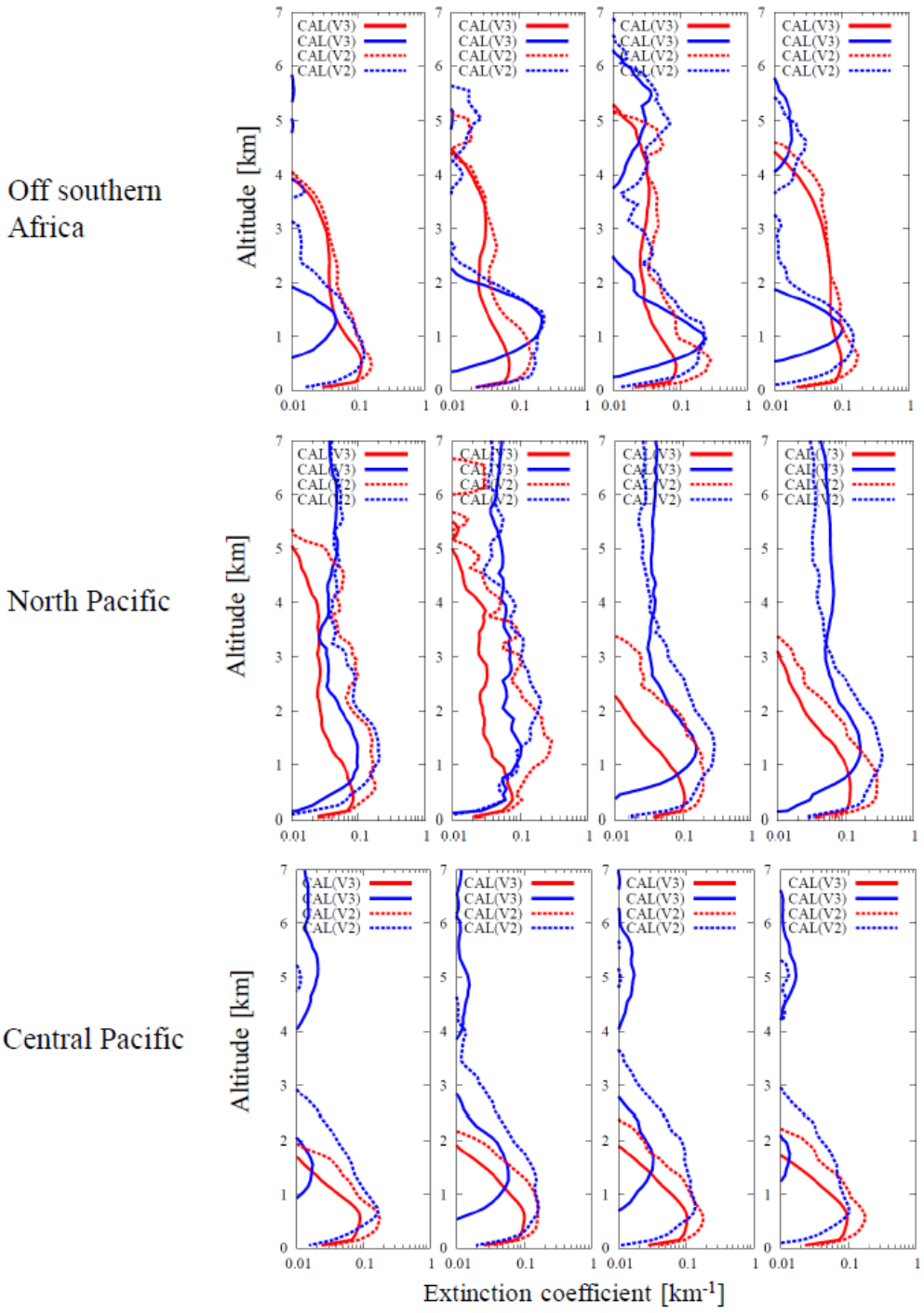

Fig. 2-13. Same as Fig. 2-12, but the seasonal mean extinction profiles for aerosols (red) and clouds (blue) in below-cloud case. The range of *x*-axis is from 0.01 to 1 [km^{-1}].

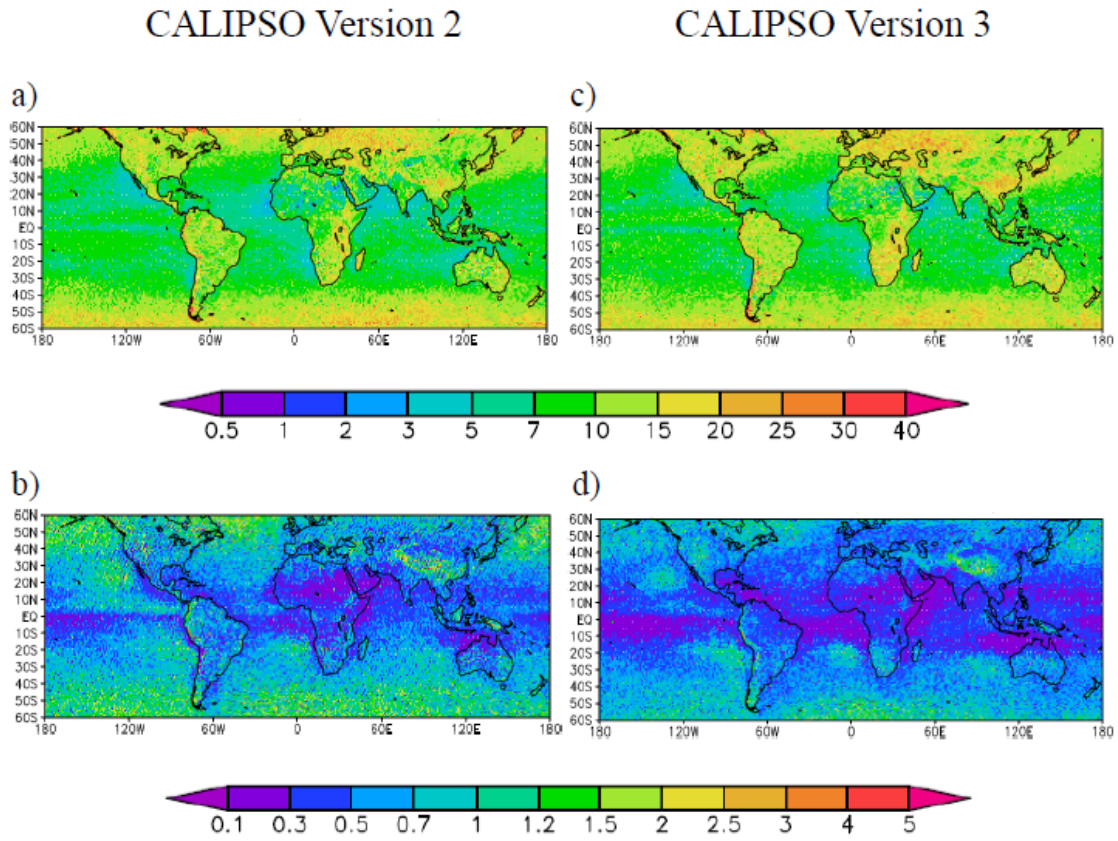

Fig. 2-14. Annual mean distributions of cloud optical thickness (COT) of above-cloud (top) and below-cloud (bottom) cases for CALIPSO Version 2 (left) and Version 3 (right) products.

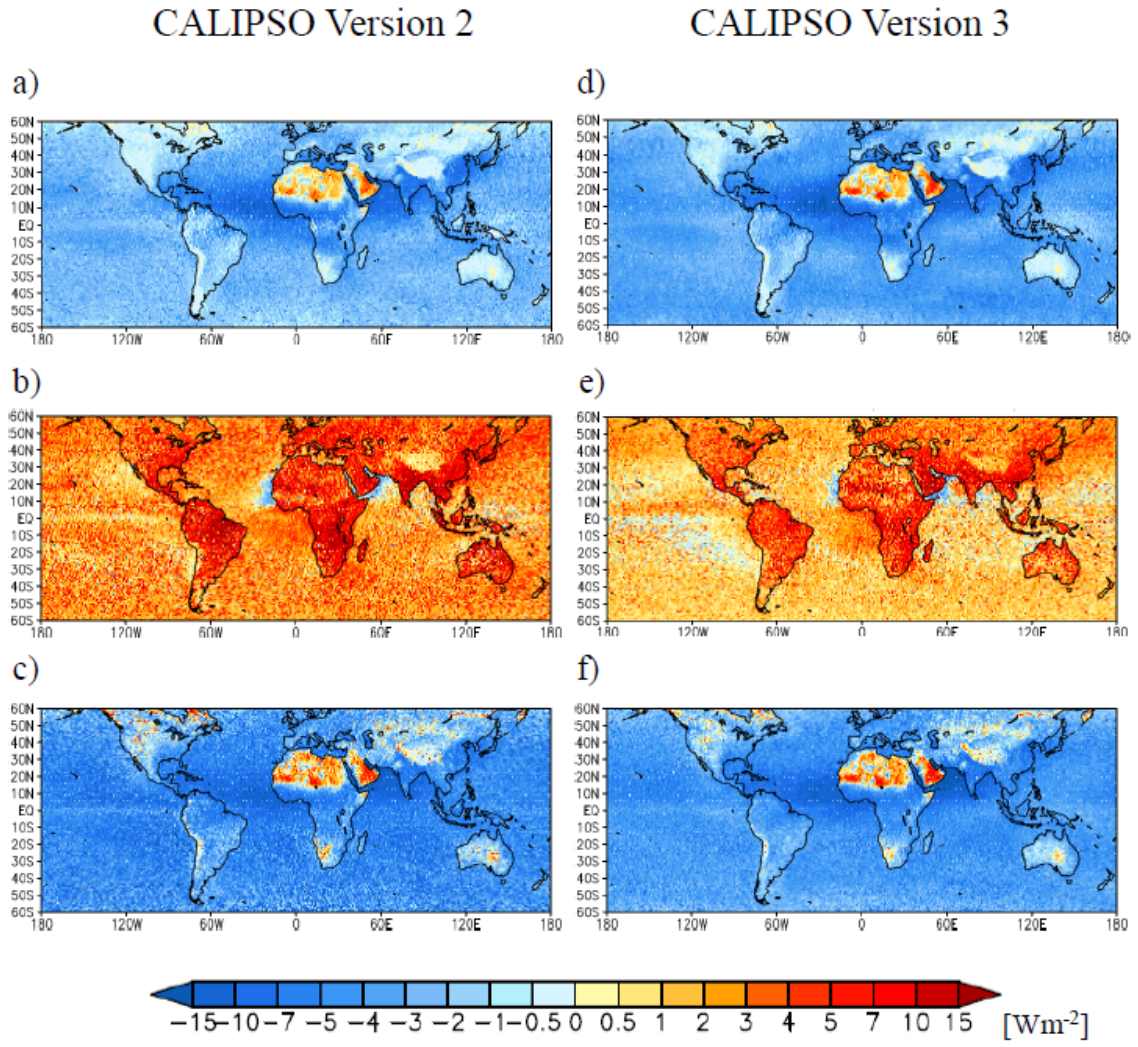

Fig. 2-15. Annual mean distributions of SWDARF for clear-sky (a, d), above-cloud (b, e), and below-cloud (c, f) cases for CALIPSO Version 2 (left) and Version 3 (right) products.

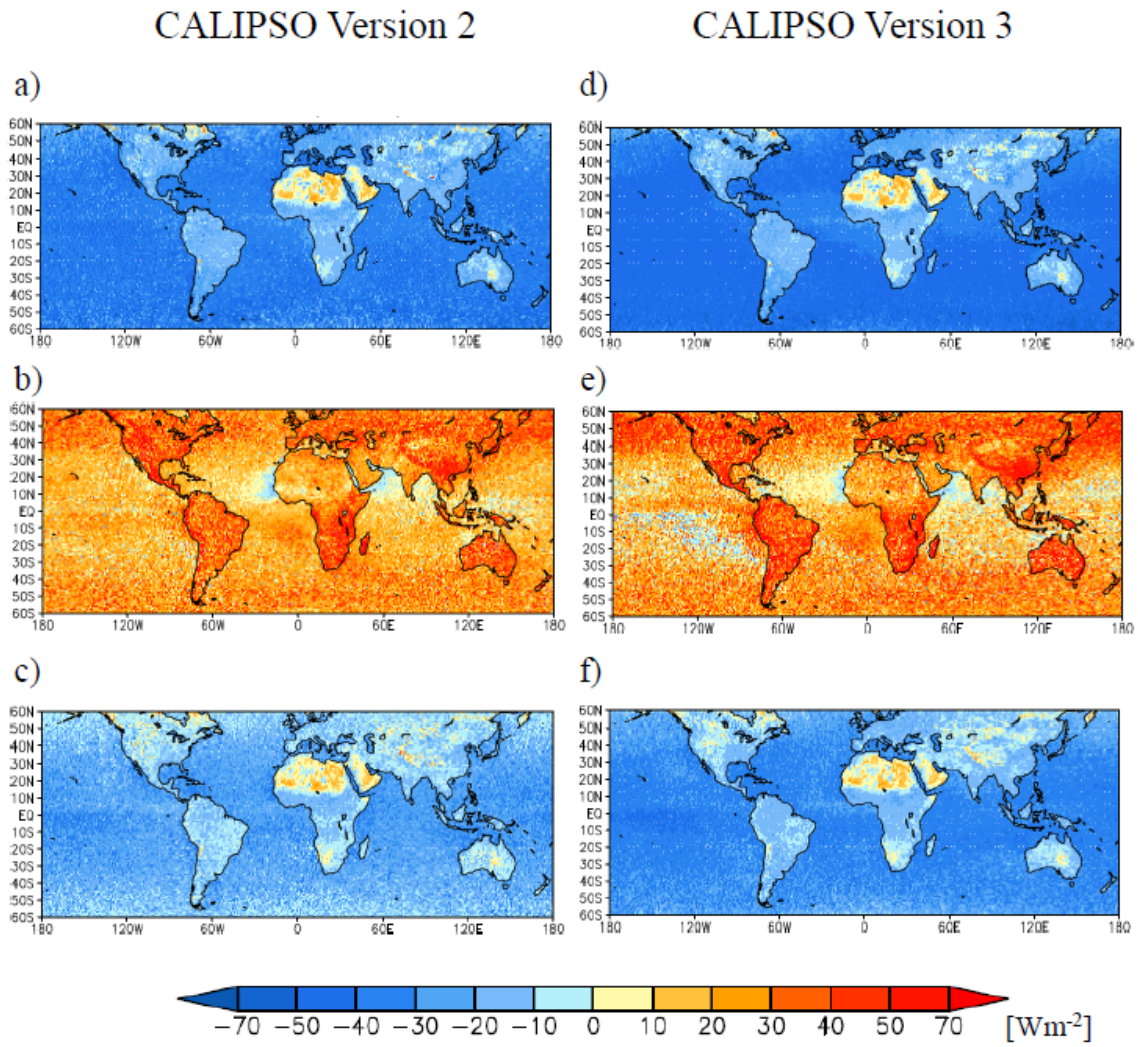

Fig. 2-16. Annual mean distributions of the radiative forcing efficiency (RFE) for clear-sky (a, d), above-cloud (b, e), and below-cloud (c, f) cases for CALIPSO Version 2 (left) and V3 (right) products.

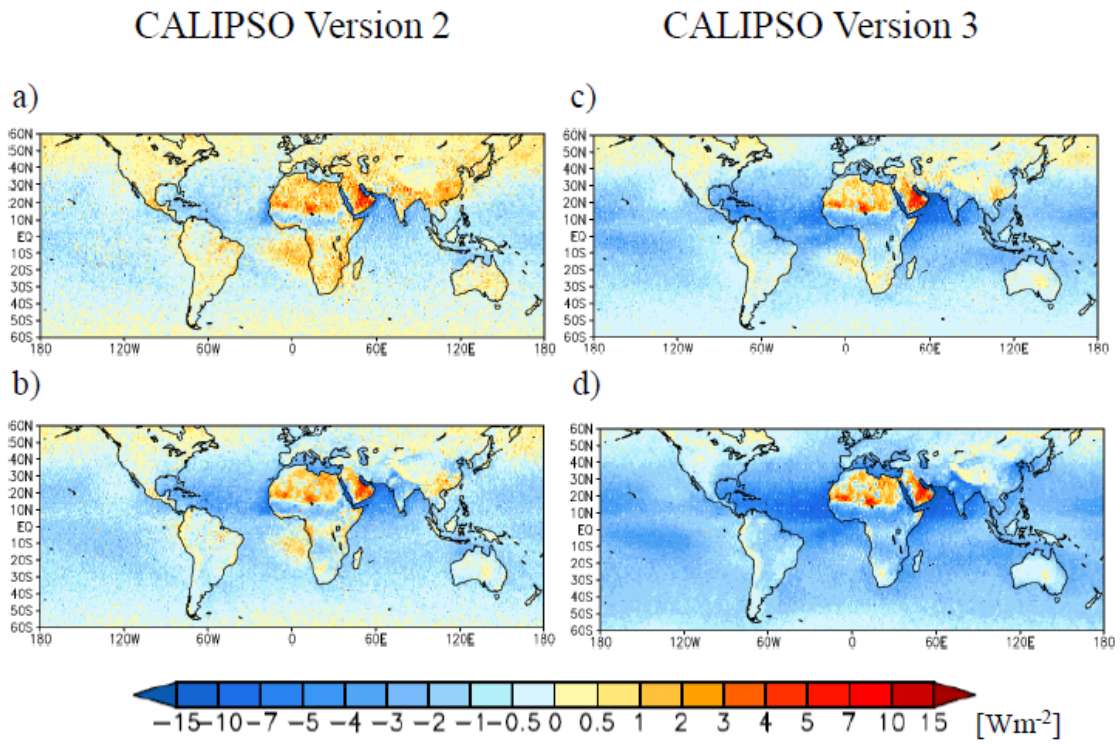

Fig. 2-17. Annual mean distributions of SWDARF for cloudy-sky (top) and all-sky (bottom) conditions for CALIPSO Version 2 (left) and Version 3 (right) products.

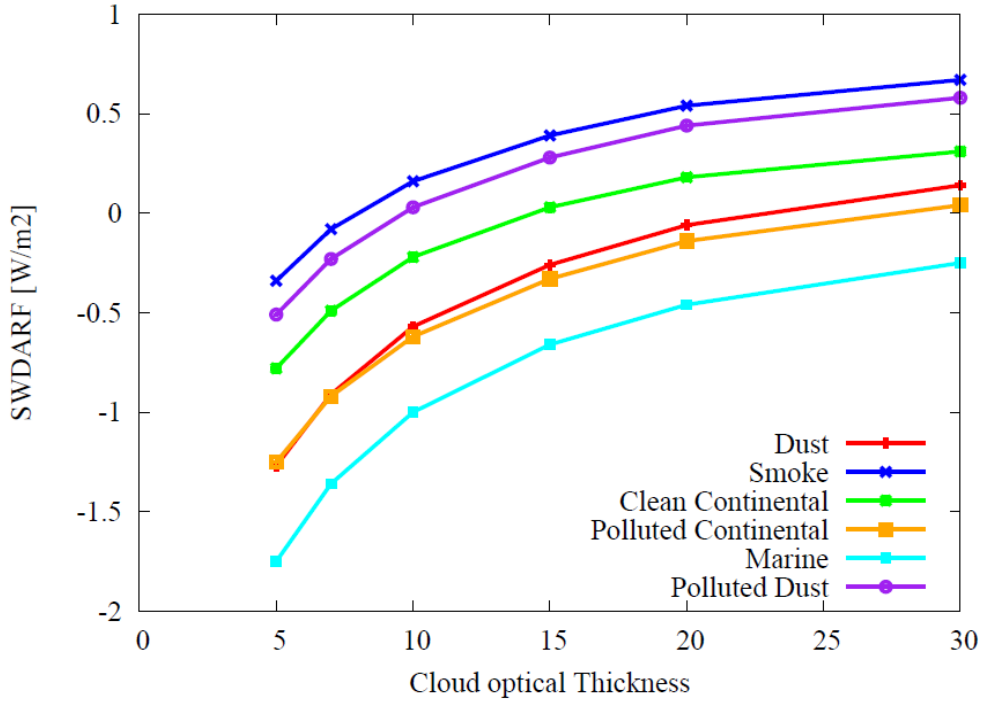

Fig. 2-18. SWDARF of the CALIPSO six aerosol types depending on COT when aerosols exist from 0 to 3 km altitude and clouds exist from 1 to 5 km altitude. This situation is classified as the cloudy-undetected case in this study. Cloud layer is the mixed layer of water and ice particles and aerosol and cloud layers are homogeneous layers. AOT at 532 nm is 0.1.

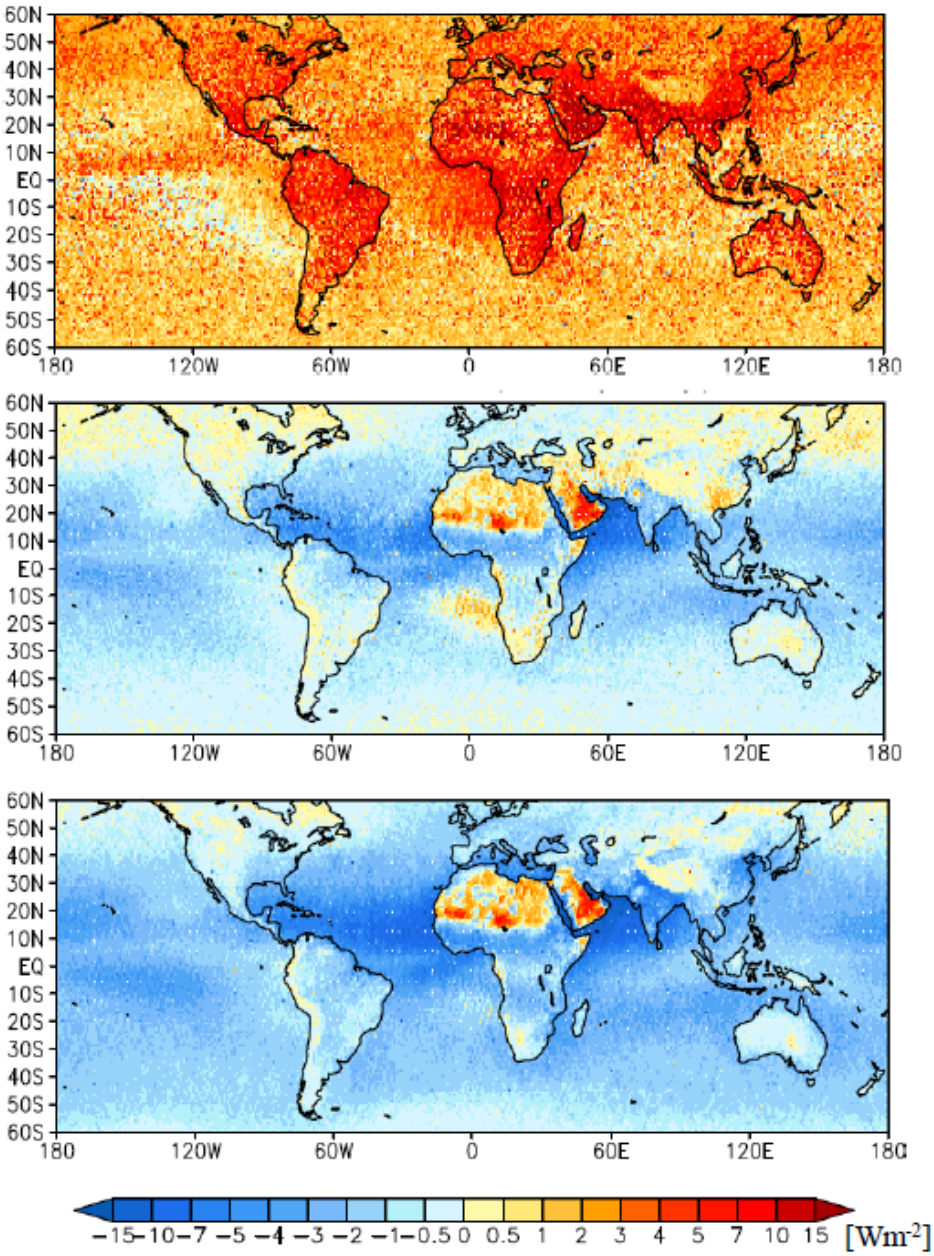

Fig. 2-19. Annual mean distributions of SWDARF for the average of the sensitivity tests in above-cloud (top), cloudy-sky (middle), and all-sky (bottom) cases.

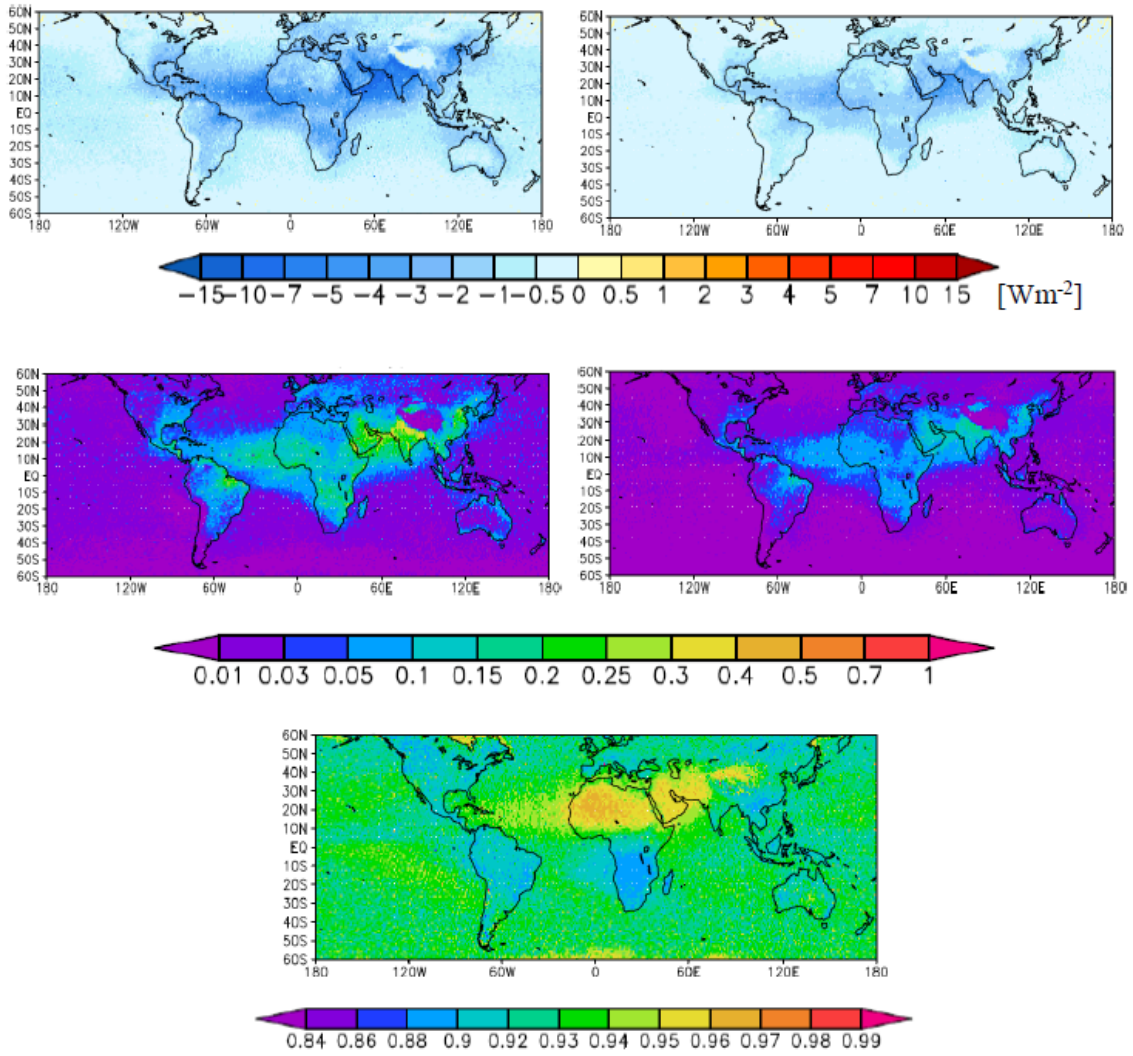

Fig. 2-20. Annual mean distributions of SWDARF (top), AOT at 532 nm (middle), and SSA at 532 nm (bottom) for fine mode aerosols (left) and anthropogenic aerosols (right) from CALIPSO Version 3 retrievals. SSAs of fine mode aerosols and anthropogenic aerosols are same, because the fraction of the CALIPSO six aerosol types for anthropogenic aerosols is the same as that of fine mode aerosols in the definition of this study (see section 2.5.5).

3. Direct aerosol radiative forcing of AGCM

3.1 Model description

The atmosphere–ocean general circulation model, Model for Interdisciplinary Research on Climate (MIROC), has been cooperatively developed at the Atmosphere and Ocean Research Institute (AORI) of the University of Tokyo, National Institute for Environmental Studies (NIES), and Japan Agency for Marine-Earth Science and Technology (JAMSTEC). MIROC5 is the latest version of MIROC model [*Watanabe et al*., 2010], which has been used for the Intergovernmental Panel on Climate Change (IPCC) Fifth Assessment Report (AR5) [*IPCC*, 2013]. Here, I introduce the schemes of aerosols, clouds, and land components which are intimately related to the DARF.

The aerosol transport model, SPRINTARS, calculates global distributions and climate effects of the main tropospheric aerosols, and is coupled with MIROC5. MIROC-SPRINTARS calculates mass mixing ratios of the main tropospheric aerosols, i.e., soil dust, carbonaceous aerosol (black carbon (BC) and organic carbon (OC)), sulfate, sea salt, and the precursor gases of sulfate (sulfur dioxide (SO_2) and dimethyl sulfide (DMS)) [*Takemura et al.*, 2000, 2005, 2009]. The aerosol transport processes include emission, advection, diffusion, sulfur chemistry, deposition, and gravitational settling. SPRINTARS is coupled with the radiation code, mstrn, to estimate DARF of total aerosols and simulate seasonal and geographical distribution patterns of aerosols which are consistent with AVHRR retrievals [*Takemura et al*., 2002]. SPRINTARS also includes the cloud microphysics schemes to calculate the direct and indirect effects of anthropogenic aerosols [*Takemura et al*., 2005].

The cloud scheme of MIROC5 consists of the prognostic conventional large-scale condensation (LSC) scheme [*Watanabe et al*., 2009] for cloud water and the bulk microphysical scheme [*Wilson and Ballard*, 1999] for cloud ice. By combining the two schemes, the fraction of cloud liquid and ice is no longer just a simple function of temperature. The LSC scheme solves prognostic equations for the subgrid scale variance and skewness of a conservative quantity associated with temperature and total water, and hence represents various cloud regimes having different optical properties. The cloud microphysical scheme explicitly deals with the warm and cold rain processes, i.e., nucleation, deposition and sublimation, riming, ice melting, and raindrop capturing by falling ice,.

The broadband radiative transfer code mstrnX [*Sekiguchi and Nakajima*, 2008] has been implemented in MIROC5. MstrnX in MIROC5 calculates 15 bands in shortwave radiation and 14 bands in longwave radiation, total 29 bands, and 111 integration points in the correlated *k*-distribution method based on spectroscopic parameters of gas line

absorption of HITRAN (HI-resolution TRANsmission) 2004 database [*Rothman et al*., 2004]. MstrnX can also be used to treat Rayleigh and Mie scattering and absorption/emission of aerosols and clouds using the two-stream flux approximation.

The ground albedo is related to the vegetation type simulated in the updated version of the land surface model, Minimal Advanced Treatments of Surface Interaction and Runoff (MATSIRO) [*Takata et al.*, 2003]. The ice sheet albedo for both visible and near-infrared radiation is expressed as a function of the water content above the ice following *Bougamont et al*. [2005] and that for infrared radiation, which is a fixed value of 0.05. The values of surface albedo for bare sea ice are fixed at 0.8 and 0.65 for the visible and near-infrared bands, respectively. Over the sea ice covered with snow, the surface albedo depends on temperature by considering the existence of partial snow cover at a relatively high temperature. The visible albedo changes from 0.9 at lower than −5 °C to 0.8 at 0 °C and the near-infrared albedo changes from 0.8 at lower than −5 °C to 0.65 at 0 °C.

Optical properties of aerosols and clouds depend on wavelength, refractive indices, size distribution, and hygroscopic growth of sulfate and carbonaceous aerosols. The same values of refractive indices of dry aerosols and cloud particles (water and ice) are used in SPRINTARS and mstrnX. Refractive indices of dry aerosols and cloud particles (water and ice) are based on *Deepak and Gerber* [1983], *d'Almeida et al.* [1991], and *Sutherland and Khanna* [1991], except for the imaginary part of soil dust. The imaginary part of the refractive index for soil dust is assumed as a quarter of values as given by *Deepak and Gerber* [1983], because recent studies [e.g., *Kaufman et al*., 2001; *Dubovik et al.*, 2002] indicated smaller value than that as given by *Deepak and Gerber* [1983]. The fixed mode radius of each dry particle and standard deviation are based on the work of *Martins et al.* [1996] for carbonaceous aerosols and *d'Almeida et al.* [1991] for other aerosols. Carbonaceous aerosols are assumed as pure BC, pure OC and the internal mixture of BC and OC for the radiation transfer calculation. The hygroscopic growth of aerosol particles is according to *Tang and Munkelwitz* [1994] for sulfate and *Hobbs et al.* [1997] for carbonaceous particles. The detailed information is described in *Takemura et al.* [2005].

In this study, aerosol emissions of the Representative Concentration Pathway (RCP) 4.5 scenario [*Thomson et al.*, 2011] are used. RCP 4.5 is a scenario of long-term, global emissions of greenhouse gases, short-lived species, and land-use-land-cover, which stabilizes increment of radiative forcing at 4.5 Wm^{-2} (approximately 650 ppm CO_2-equivalent) in the year 2100 from pre-industrial era. Model simulation is performed with a horizontal resolution of T42 (approximately 2.8° × 2.8°) with 20

vertical layers (sigma levels based on the surface pressure at 0.995, 0.980, 0.950, 0.900, 0.830, 0.745, 0.650, 0.549, 0.454, 0.369, 0.295, 0.230, 0.175, 0.124, 0.085, 0.060, 0.045, 0.035, 0.025, and 0.008). The time step is set at 20 minutes. The simulation is done for three years from 2007 to 2009, after one year spin-up, with nudged meteorological fields (wind speed, water vapor, and temperature) of reanalysis data provided by the NCAR/NCEP [*Kalney et al.*, 1996]. Sea surface temperature (SST) and sea ice distribution are also nudged by the Met Office Hadley Centre's sea ice and SST data set (HadISST) [*Rayner et al*., 2003].

3.2 A new method for the radiation process of the MIROC model

In MIROC AGCM, optical properties of aerosols and clouds are separately calculated in the aerosol transport module, SPRINTARS, and the radiation module, mstrnX. MstrnX calculates the representative value at wider bands of optical properties for the radiation field calculation. Radiation calculation is performed every 3 hours in order to save CPU time. On the other hand, SPRINTARS calculates optical properties at particular wavelengths such as 355, 440, 532, 550, 870, and 1064 nm at every time step of 20 minutes. Aerosol optical parameters calculated by SPRINTARS are used for the detailed comparison to the observation. In this view, optical parameters of aerosols and clouds need to be calculated in both SPRINTARS and mstrnX. In SPRINTARS, mass emission fluxes of dust and sea salt are calculated depending on surface wind velocity. Small particles are easily emitted from ground/ocean surface; therefore, 6 size bins of dust and 4 size bins of sea salt are taken into account in SPRINTARS [*Takemura et al.,* 2009]. On the other hand, the size-dependent information of dust and sea salt is ignored in mstrnX for saving CPU time, because CPU time of radiation calculation is about 34% of that of MIROC AGCM simulation. Information of the volume size distribution and mass per unit volume m_a for each dry aerosol component is summarized in Table 3-1. Values of m_a for dust and carbonaceous aerosols are different between SPRINTARS and mstrnX, i.e. m_a in SPRINTARS is based on the version of SPRINTARS in *Takemura et al.* [2009], whereas that of mstrnX is based on the version of SPRINTARS in *Takemura et al.* [2005]. This model is referred to as the SPstd model.

In order to improve the inconsistency of optical models in SPRITNARS and mstrnX, I develop a new interface between SPRINTARS and mstrnX for investigating the radiative impact on aerosol optical properties such as AOT, SSA, and SWADARF of size index. In this study, the new model is referred to as the SPnew model. In SPnew model, 6 size bins of dust, 4 types of carbonaceous aerosols (pure BC, pure OC, and 2 types of internal mixture of BC and OC), sulfate, and 4 size bins of sea salt are treated

in SPRINTARS and mstrnX for calculation of the optical properties for aerosols. The size indices and m_a of mstrnX match those of SPRINTARS (Table 3-2). GSDs of volume size distribution for dust and sea salt are set to 1.1 and 1.2 (see Appendix B). Water-soluble aerosols can take up water and become larger particles. The mode radius of the volume size distribution for hygroscopic growth, r_{RH}, is expressed by

$$r_{RH} = FRH \times r_{dry}, \tag{3-1}$$

where r_{dry} is dry mode radius and FRH is the growth ratio depending on the relative humidity. Table 3-3 shows FRH of carbonaceous aerosols (pure OC and internal mixture of BC and OC), sulfate, and sea salt. In SPnew model, cloud optical parameters of water and ice particles of SPRINTARS and mstrnX are calculated corresponding to 12 different size radii of volume size distribution. The sizes of water cloud are set to 4, 6, 8, 10, 12, 14, 16, 18, 20, 22, 24, and 26 μm and those of ice cloud are set to 5, 10, 15, 20, 25, 30, 35, 40, 50, 60, 70, and 80 μm.

Due to increase in the number of particle component from 9 (7 aerosol types and 2 cloud types) to 17 (15 aerosol types and 2 cloud types), CPU time of radiation calculation increases by 75% and that of total model simulation increases by 25%.

3.3 Results

3.3.1. Optical parameters of aerosols and clouds in SPstd and SPnew models

In this section, I compare AOT and SSA at 550 nm from SPRITNARS and the representative values of AOT and SSA between 435 and 678 nm from mstrnX in both SPstd and SPnew models. Figure 3-1 shows annual mean distributions of AOT for dust, carbonaceous aerosols, sulfate, and sea salt from SPRINTARS and mstrnX in SPstd model. If fine mode and coarse mode aerosols have a same volume and a same composition, coarse mode aerosols have larger absorption and smaller AOT than fine mode aerosols. MstrnX AOT of dust is smaller than SPRINTARS AOT, because amount of fine mode dust is underestimated in mstrnX with SPstd model. For carbonaceous aerosols, mstrnX AOT is larger than SPRINTARS AOT, because m_a of mstrnX is smaller than that of SPRINTARS (Table 3-1) and the volume of carbonaceous aerosols is overestimated by SPstd model. The distribution of sulfate is similar in both SPRINTARS and mstrnX. The ratio of hygroscopic growth for sea salt in SPRINTARS is larger than that in mstrnX; therefore, sea salt particles and AOT become larger in SPRINTARS. Figure 3-2 shows annual mean distributions of AOT and SSA for total aerosols from SPRINTARS and mstrnX in SPstd model. In mstrnX, fine mode dust is underestimated, so that AOT and SSA are smaller than those from SPRINTARS over

Saharan and Arabian deserts. Over southern Africa, Indian, and East Asia, mstrnX AOT is larger and SSA is smaller than SPRINTARS, because mstrnX carbonaceous AOT is larger and indicates more absorption. SPRINTARS sea salt AOT is larger than mstrnX, so that SPRINTARS SSA is larger over ocean, except for the ocean around 60°S. In this region, sea salt is the major aerosol component and SSA is 0.99 in SPRINTARS and mstrnX.

Figure 3-3 shows annual mean distributions of AOT for dust, carbonaceous aerosols, sulfate, and sea salt from SPRINTARS and mstrnX in SPnew model. It is found that the distributions from SPRINTARS and mstrnX for each aerosol component are almost same. Sea salt AOT of mstrnX is slightly smaller than that of SPRINTARS over the North Atlantic. Optical properties of aerosols and solar irradiance change from 435 to 678 nm, so that the weighted averages of mstrnX are not exactly the same as SPRINTARS values at 550 nm. The geographical distributions of AOT and SSA for total aerosols are also almost same between SPRINTARS and mstrnX (Fig. 3-4). After this paragraph, I mainly show mstrnX AOT and SSA, because aerosol optical parameters of mstrnX are more important to discuss SWDARF.

Figure 3-5 shows annual mean distribution of COT for large scale clouds and cumulus from mstrnX in the SPstd and SPnew models. Compared with SPstd model, COT of large scale cloud is larger over the ocean at low-latitudes and larger over the ocean at mid-latitudes in SPnew model, because the size dependency of cloud optical parameters is more properly calculated using the look-up table of optical parameters for 12 different cloud sizes. COT of cumulus and cloud cover fraction of SPnew is almost same as those of SPstd (Fig. 3-6).

3.3.2 SWDARF under clear-sky, cloudy-sky, and all-sky conditions

The all-sky AOT and SSA are simulated by the model. For comparison with CALIPSO observations, averages of parameters (AOT and SSA) under clear-sky and cloudy-sky conditions are analytically calculated using column cloud cover fraction C. The column cloud fraction is calculated by the maximum random overlapping method at each time step in the model. The relationship of the parameter x, which means AOT and SSA, among $x_{\text{all-sky}}$, $x_{\text{clear-sky}}$, and $x_{\text{cloudy-sky}}$ is expressed by

$$x_{\text{all–sky}} = (1-C)\cdot x_{\text{clear–sky}} + C\cdot x_{\text{cloudy–sky}}\,. \tag{3-2}$$

From Eq. (3-2), time averages of $x_{\text{all-sky}}$, $x_{\text{clear-sky}}$, and $x_{\text{cloudy-sky}}$ are given by

$$\left\langle x_{\text{all-sky}} \right\rangle = \frac{\sum_{i=1}^{N} x_{\text{all-sky},i}}{N}$$

$$\left\langle x_{\text{clear-sky}} \right\rangle = \frac{\sum_{i=1}^{N} (1 - C_i) \cdot x_{\text{all-sky},i}}{\sum_{i=1}^{N} (1 - C_i)}, \tag{3-3}$$

$$\left\langle x_{\text{cloudy-sky}} \right\rangle = \frac{\sum_{i=1}^{N} C_i \cdot x_{\text{all-sky},i}}{\sum_{i=1}^{N} C_i}$$

where subscript i means i-th time step.

Figures 3-7 and 3-8 show the annual mean distributions of AOT and SSA under clear-sky, cloudy-sky, and all-sky conditions in SPstd and SPnew models. The cloudy-sky AOT is larger than the clear-sky AOT, because, in cloudy-sky condition, the relative humidity is higher and AOT becomes larger due to hygroscopic growth. In particular, the cloudy-sky AOT is twice as large as clear-sky AOT over East Asia. This region is a source region of industrial emissions and biomass burning and cloud fraction is high (Fig. 3-6); therefore, the effect of hygroscopic growth for high concentration aerosols is larger than other areas. The clear-sky SSA is lower than cloudy-sky SSA over Africa, South America and East Asia. These regions are source regions of dust and BC. In clear-sky condition, hygroscopic growth is suppressed and the fraction of dust and BC is larger, so that SSA is smaller than that of cloudy-sky condition.

Similarly, the clear-sky and all-sky SWDARFs are calculated by the model. The relationship among $SWDARF_{\text{all-sky}}$, $SWDARF_{\text{clear-sky}}$, and $SWDARF_{\text{cloudy-sky}}$ is expressed by

$$SWDARF_{\text{all-sky}} = (1 - C) \cdot SWDARF_{\text{clear-sky}} + C \cdot SWDARF_{\text{cloudy-sky}}, \tag{3-4}$$

and time averages of $SWDARF_{\text{all-sky}}$, $SWDARF_{\text{clear-sky}}$, and $SWDARF_{\text{cloudy-sky}}$ are given by

$$\left\langle SWDARF_{\text{all-sky}} \right\rangle = \frac{\sum_{i=1}^{N} SWDARF_{\text{all-sky},i}}{N}$$

$$\left\langle SWDARF_{\text{clear-sky}} \right\rangle = \frac{\sum_{i=1}^{N} (1 - C_i) \cdot SWDARF_{\text{clear-sky},i}}{\sum_{i=1}^{N} (1 - C_i)} \quad . \qquad (3\text{-}5)$$

$$\left\langle SWDARF_{\text{cloudy-sky}} \right\rangle = \frac{\sum_{i=1}^{N} \left(SWDARF_{\text{all-sky},i} - (1 - C_i) \cdot SWDARF_{\text{clear-sky},i} \right)}{\sum_{i=1}^{N} C_i}$$

Figure 3-9 shows the annual mean distributions of SWDARF under clear-sky, cloudy-sky, and all-sky conditions calculated by SPstd and SPnew models. In SPstd model, the amount of fine mode dust is underestimated and SSA is 0.93 over Saharan and Arabian deserts. In these regions, SWDARF is positive under clear-sky, cloudy-sky, and all-sky conditions, because aerosol absorption is enhanced by high surface reflectance of 0.3 (Fig. 3-10). In these regions, the cloudy-sky forcing is more positive than the clear-sky forcing, because the cloudy-sky AOT is larger than the clear-sky AOT. On the other hand, the SPnew SWDARF is negative, because SSA is larger than 0.94 and aerosol absorption is not enough to change the sign of forcing from negative to positive.

Compared with the results of SPstd model, the cloudy-sky SWDARF of SPnew model shows smaller positive forcing over southern Africa and South America, because AOT of black carbon becomes smaller and SSA becomes larger. Over Asia, fine mode dust increase and AOT of black carbon becomes smaller, the cloudy-sky SWDARF becomes smaller positive. For these reasons, the all-sky SWDARF becomes smaller positive forcing over the central Africa and East Asia.

The global averages of clear-sky, cloudy-sky, and all-sky SWDARFs are −1.79, −0.28, and −0.65 Wm^{-2} from SPstd model and −1.90, −0.09, and −0.97 Wm^{-2} from SPnew model. The SWDARFs become larger negative; however, the clear-sky SWDARF is still largely smaller than the satellite-based average, -5.3 ± 0.2 Wm^{-2}, and the model-based average, -3.3 ± 0.6 Wm^{-2} in *Yu et al*. [2006].

3.3.3 SWDARF of fine mode and anthropogenic aerosols

The DARF of anthropogenic aerosols is usually defined in terms of radiative flux changes at the top of the atmosphere (TOA) or at the climatological tropopause,

between pre-industrial era and present-day by the model simulation. In section 2.5.5, I calculate SWDARF of fine mode and anthropogenic aerosols using CALIPSO V3 Product using the assumption of the fine mode Fraction of AOT (FMF) and the anthropogenic fraction of AOT, F_{anth}. I also try to calculate SWDARF of fine-mode and anthropogenic aerosols from the present-day simulation in a similar way to the CALIPSO observations. In this simulation, the fine mode aerosols are defined as aerosols with dry particle radius of smaller than 1 μm: sulfate, BC, OC and dust (0.13, 0.33, and 0.82 μm), and sea salt (0.13 and 0.57 μm). According to the assumptions and equations in section 2.5.5, with the mean value of F_{anth} in AeroCom models, 24 % [*Myhre et al.*, 2013], the zonal mean values between 60°S and 60°N of AOT_{fine}, FMF, and f are 0.021, 0.77, and 0.33, respectively. The zonal mean value between 60°S and 60°N of anthropogenic AOT is 0.021, which is calculated by Eq. (2-18) using the values of AOT_{fine}, FMF, and f.

Figure 3-11 shows annual mean distributions of SWDARF and AOT for fine-mode aerosols and anthropogenic aerosols simulated by the SPnew model. The figure shows that the geographical distribution of fine mode AOT is similar to that of total AOT, except for the ocean in southern hemisphere, because dominating particles are fine mode aerosols in SPRINTARS with FMF = 0.77. On the other hand, anthropogenic AOT is one-third as large as fine mode AOT from the definition of this study. Significant anthropogenic aerosol forcings are located in limited areas in near source regions. Geographical patterns of SWDARF for fine mode and anthropogenic aerosols are similar to those of total aerosols. SWDARFs of fine mode and anthropogenic aerosols show positive forcings over central Africa and East Asia as well as SWDARF of total aerosols. Anthropogenic SWDARF is the larger negative forcing than –0.5 Wm^{-2} over near source regions. The global average of the all-sky SWDARF for fine-mode aerosols and anthropogenic aerosols are –0.76 and –0.24 Wm^{-2}, respectively. My estimate of the anthropogenic SWDARF thus obtained is comparable with the Aerocom model mean value, –0.22 Wm^{-2} [*Schulz et al.*, 2006].

3.4 Summary of SWDARF from modeling

In MIROC AGCM, the optical properties of aerosols and clouds are separately calculated in SPRINTARS and mstrnX. MstrnX AOT and SSA are smaller than those of SPRINTARS, because the aerosol size indices of mstrnX are different from those of SPRINTAS in order to save CPU time. In this study, this model is referred to as the SPstd model.

I developed a new aerosol optical model applicable to both SPRINTARS and

mstrnX for investigating the impact on aerosol optical properties such as AOT, SSA, and SWADARF of size index. In the new model, 6 different size dust, 4 types of carbonaceous aerosols, sulfate, and 4 different size sea salt are mutually taken into account in SPRINTARS and mstrnX for the calculation of optical properties for aerosols. The size index and m_a of mstrnX match those of SPRINTARS. In this study, the new model is referred to as the SPnew model.

Table 3-4 shows annual global mean values of AOT for dust, carbonaceous aerosols, sulfate, sea salt and total aerosols in SPstd and SPnew models. In SPstd model, MstrnX AOT of dust is smaller than SPRINTARS AOT, because the size bin of dust is taken into account in mstrnX and fine mode dust is underestimated. MstrnX AOT of carbonaceous aerosols is larger than SPRINTARS AOT, due to the smaller carbonaceous mass. SPRINTARS AOT of sea salt is larger than mstrnX AOT, because of the higher hygroscopic growth ratio. In SPnew model, AOT of each aerosol component and SSA of mstrnX are comparable to those of SPRINTARS.

Table 3-5 summarizes the annual global mean values of AOT, SSA, COT, and SWDARF under clear-sky, cloudy-sky, and all-sky conditions in SPstd and SPnew models. It is found that the cloudy-sky AOT is larger than the clear-sky AOT, because, in cloudy-sky condition, relative humidity is higher and AOT becomes higher due to large hygroscopic growth. SPnew SSA is larger than SPstd SSA, because size bin of dust are properly treated in SPnew model and the BC mass is larger than that of SPstd model. In SPstd model, SSA is 0.93 and SWDARF is positive over Saharan and Arabian deserts, because aerosol absorption is enhanced by a high surface reflectance of 0.3. On the other hand, the SPnew SWDARF is negative, because SSA is larger than 0.94 and aerosol absorption is not enough to change the sign of the forcing from negative to positive. The cloudy-sky SWDARF of SPnew model shows a smaller positive forcing over southern Africa and South America, because the BC AOT becomes smaller and SSA becomes larger. The all-sky SWDARF becomes smaller positive over the central Africa and East Asia. The global averages of clear-sky, cloudy-sky, and all-sky SWDARF are respectively −1.79, -0.28, and −0.65 Wm^{-2} from SPstd model and −1.90, -0.09, and −0.97 Wm^{-2} from SPnew model. The SWDARFs become larger negative; however, the clear-sky SWDARF is still largely smaller than the satellite-based value of -5.3 ± 0.2 Wm^{-2}, and the model-based average of -3.3 ± 0.6 Wm^{-2} [*Yu et al*., 2006].

The SPnew model helps us to understand the relationship between aerosol climate effect and aerosol optical properties and is useful for comparison with observations. Due to increase in the number of particle component from 9 (7 aerosol types and 2 cloud types) to 17 (15 aerosol types and 2 cloud types), CPU time of radiation

calculation increases by 75% and that of total model simulation increases by 25%. This is not negligible for long-term experiments, so that I need to address challenges for saving the increased CPU time in future.

Table 3-1. Mean radius [μm] and geometric standard deviation (GSD) of volume size distribution and mass per unit volume m_a [g/cm^3] for each dry aerosol component in SPRINTARS and mstrnX in SPstd model. Aerosol components of carbon1 and carbon2 are the internal mixture of BC and OC.

	SPRINTARS			mstrnX		
	Radius (μm)	GSD	m_a	Radius (μm)	GSD	m_a
Dust	0.13, 0.33, 0.82, 1.27, 3.2, and 8.02 (6 sizes)	1	2.6	4.0 (1 size)	2.5	2.5
BC	0.04	2.0	2.3	0.05	2.0	1.25
OC	0.28	1.8	1.8	0.28	1.8	1.5
Carbon1	0.28	1.8	1.853	0.28	1.8	1.468
Carbon2	0.28	1.8	1.895	0.28	1.8	1.442
Sulfate	0.31	2.03	1.769	0.31	2.03	1.769
Sea salt	0.178, 0.562, 1.78, and 5.62 (4 sizes)	1	2.2	2.0 (1 size)	2.51	2.2

Table 3-2. Same as Table 3-1, but mean radius, GSD, and m_a for each dry aerosol component in SPnew model.

	SPRINTARS			mstrnX		
	Radius (μm)	GSD	m_a	Radius (μm)	GSD	m_a
Dust	0.13, 0.33, 0.82, 1.27, 3.2, and 8.02 (6 sizes)	1.1	2.6	0.13, 0.33, 0.82, 1.27, 3.2, and 8.02 (6 sizes)	1.1	2.6
BC	0.04	2.0	2.3	0.04	2.0	2.3
OC	0.28	1.8	1.8	0.28	1.8	1.8
Carbon1	0.28	1.8	1.853	0.28	1.8	1.853
Carbon2	0.28	1.8	1.895	0.28	1.8	1.895
Sulfate	0.31	2.03	1.769	0.31	2.03	1.769
Sea salt	0.178, 0.562, 1.78, and 5.62 (4 sizes)	1.2	2.2	0.178, 0.562, 1.78, and 5.62 (4 sizes)	1.2	2.2

Table 3-3. The growth ratio depending on relative humidity. Carbonaceous aerosols (OC and internal mixture of OC and BC), sulfate, and sea salt are water soluble particles in SPstd and SPnew models.

	Relative humidity							
	0	0.5	0.7	0.8	0.9	0.95	0.98	0.99
Carbonaceous	1	1.08	1.10	1.44	1.68	1.96	2.74	3.12
Sulfate	1	1.22	1.37	1.48	1.76	2.26	2.81	3.32
Sea salt	1	1.07	1.28	1.99	2.38	2.88	3.76	4.69

Table 3-4. Annual global mean values of AOT for dust, carbonaceous aerosols, sulfate, sea salt, and total aerosols in SPstd and SPnew models.

	Dust	Carbonaceous	Sulfate	Sea salt	Total
		SPstd model			
SPRINTARS	0.020	0.024	0.023	0.044	0.111
MstrnX	0.006	0.036	0.027	0.025	0.093
		SPnew model			
SPRINTARS	0.014	0.030	0.023	0.018	0.085
MstrnX	0.014	0.029	0.023	0.018	0.084

Table 3-5. Annual global mean values of AOT, SSA, COT, and SWDARF [Wm^{-2}] under clear-sky, cloudy-sky, and all-sky conditions in SPstd and SPnew models. AOT, SSA, and COT of large scale cloud calculated by mstrnX are listed.

	Clear-sky	Cloudy-sky	All-sky
	SPstd model		
AOT	0.073	0.110	0.093
SSA	0.96	0.97	0.97
COT	-	12.0	-
SWDARF	–1.79	+0.28	–0.65
	SPnew model		
AOT	0.070	0.097	0.084
SSA	0.97	0.98	0.98
COT	-	13.2	-
SWDARF	–1.90	–0.09	–0.97

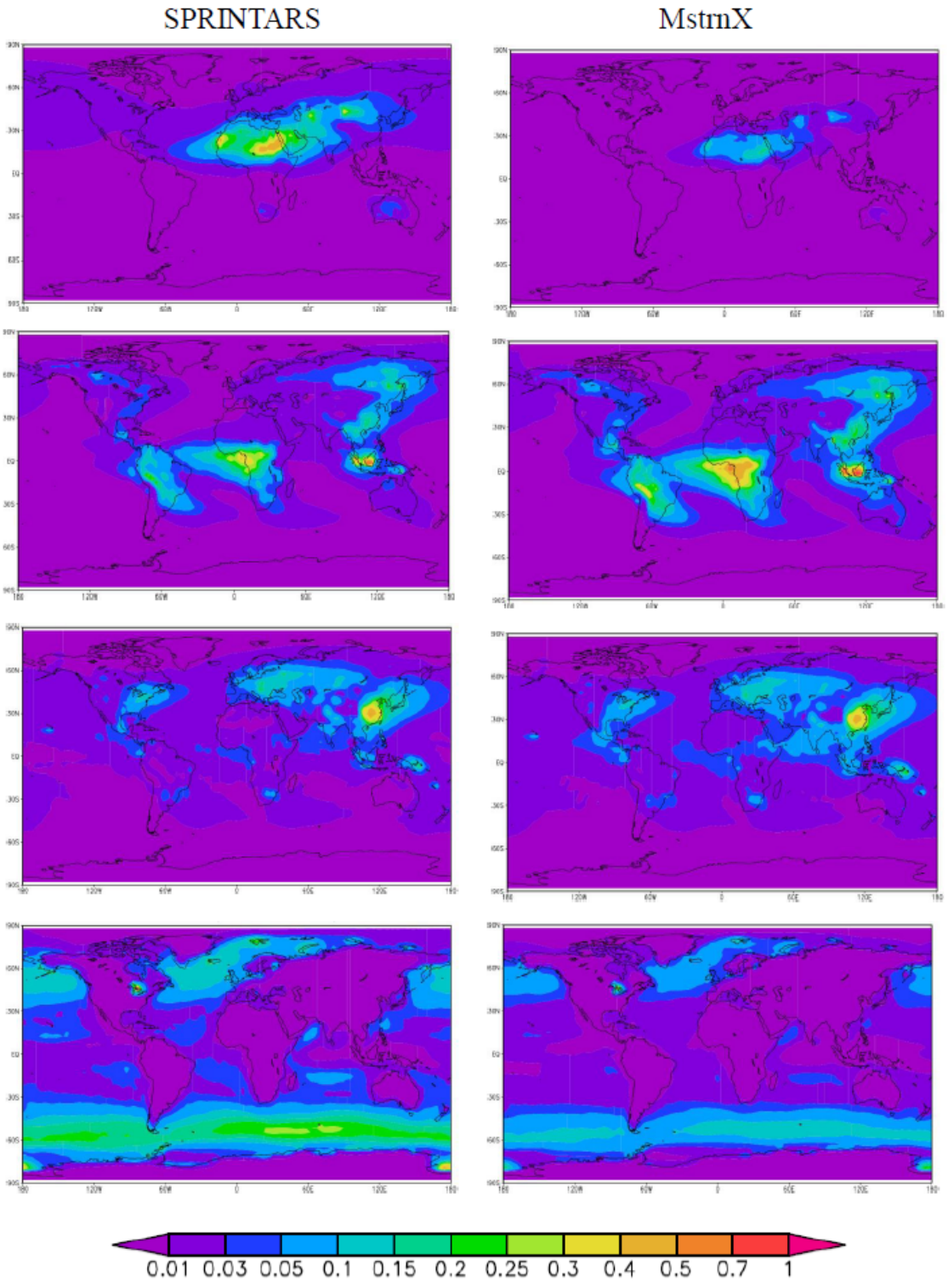

Fig. 3-1. Annual mean distributions of AOT for dust (top), carbonaceous aerosols (middle-high), sulfate (middle-low), and sea salt (bottom) from SPRINTARS (left) and mstrnX (right) in SPstd model.

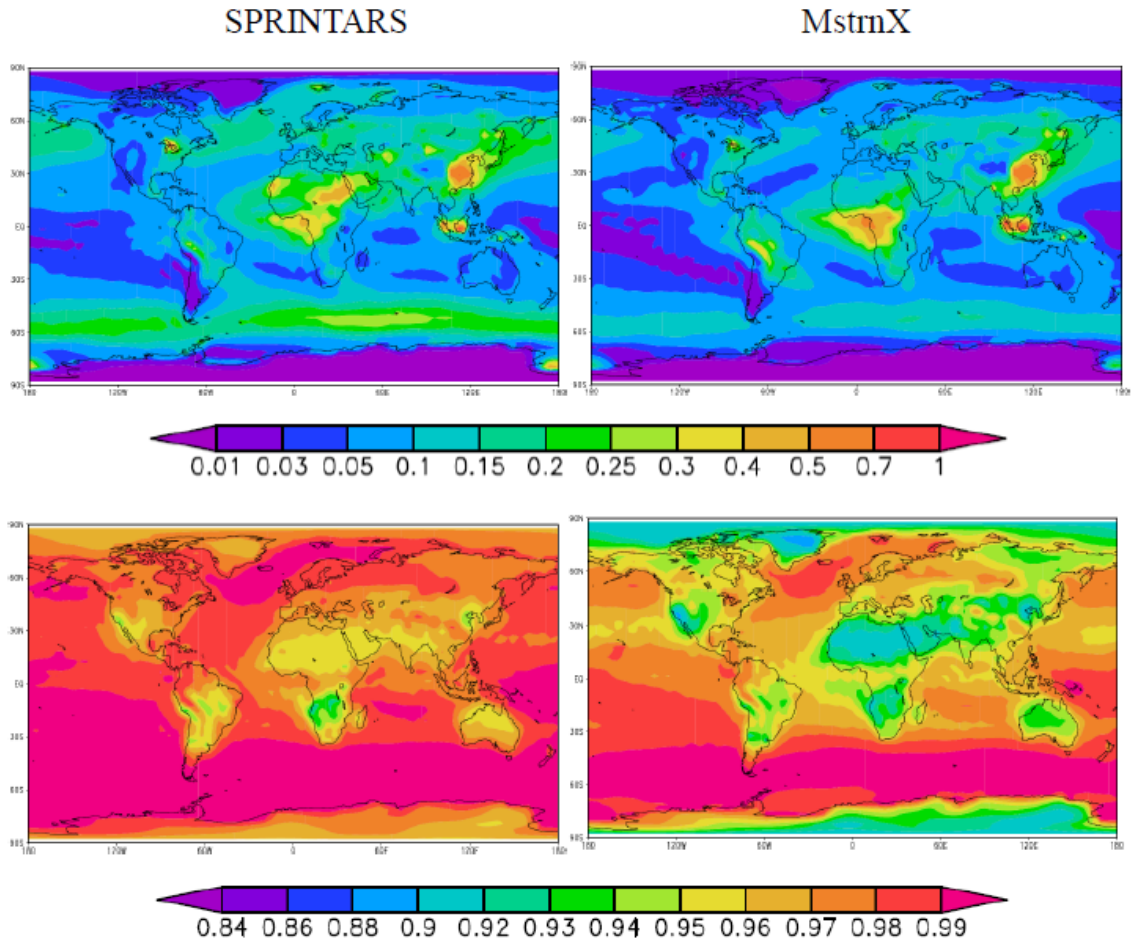

Fig. 3-2. Annual mean distributions of AOT (top) and SSA (bottom) for total aerosols from SPRINTARS (left) and mstrnX (right) in SPstd model.

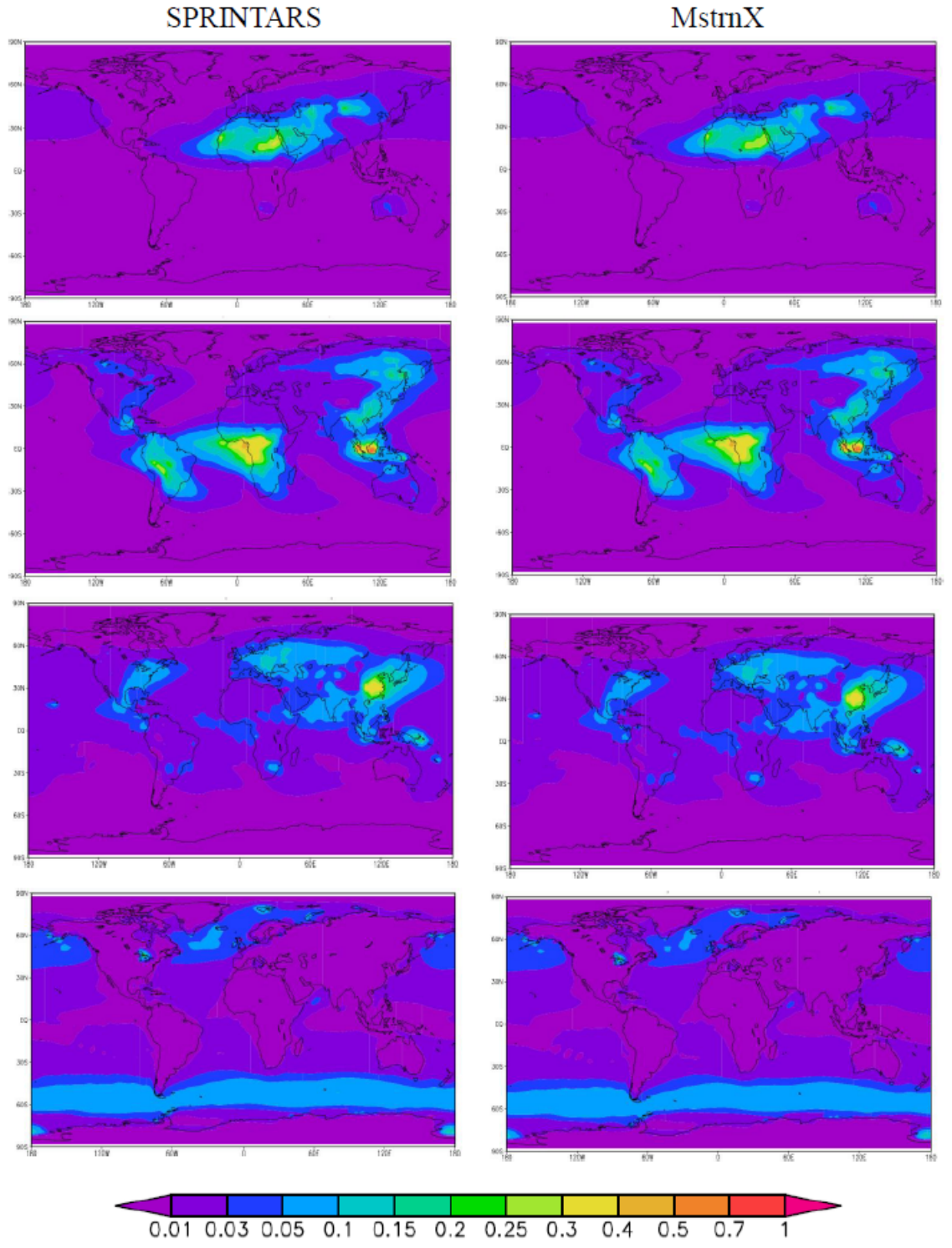

Fig. 3-3. Same as Fig. 3-1, but annual mean distributions of AOT for each aerosol component in SPnew model.

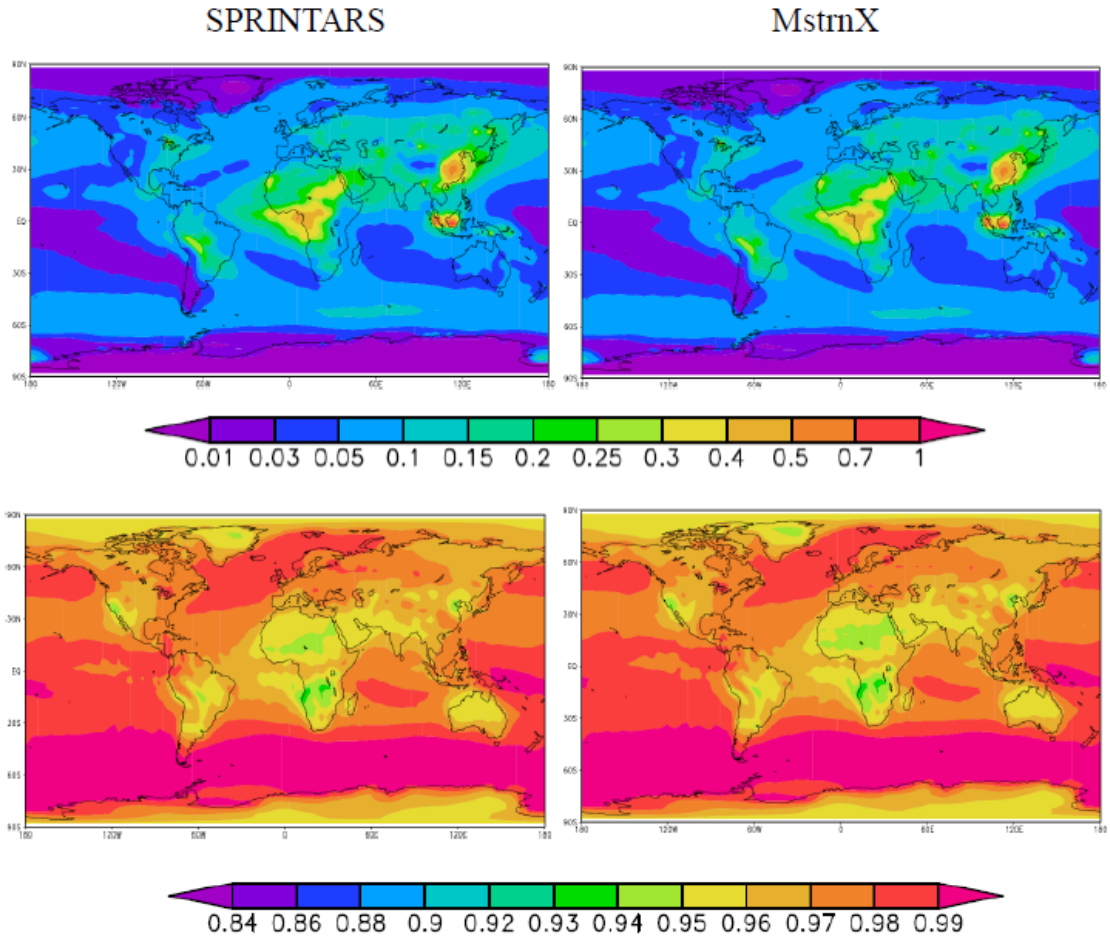

Fig. 3-4. Same as Fig. 3-2, but annual mean distributions of AOT and SSA for total aerosols in SPnew model.

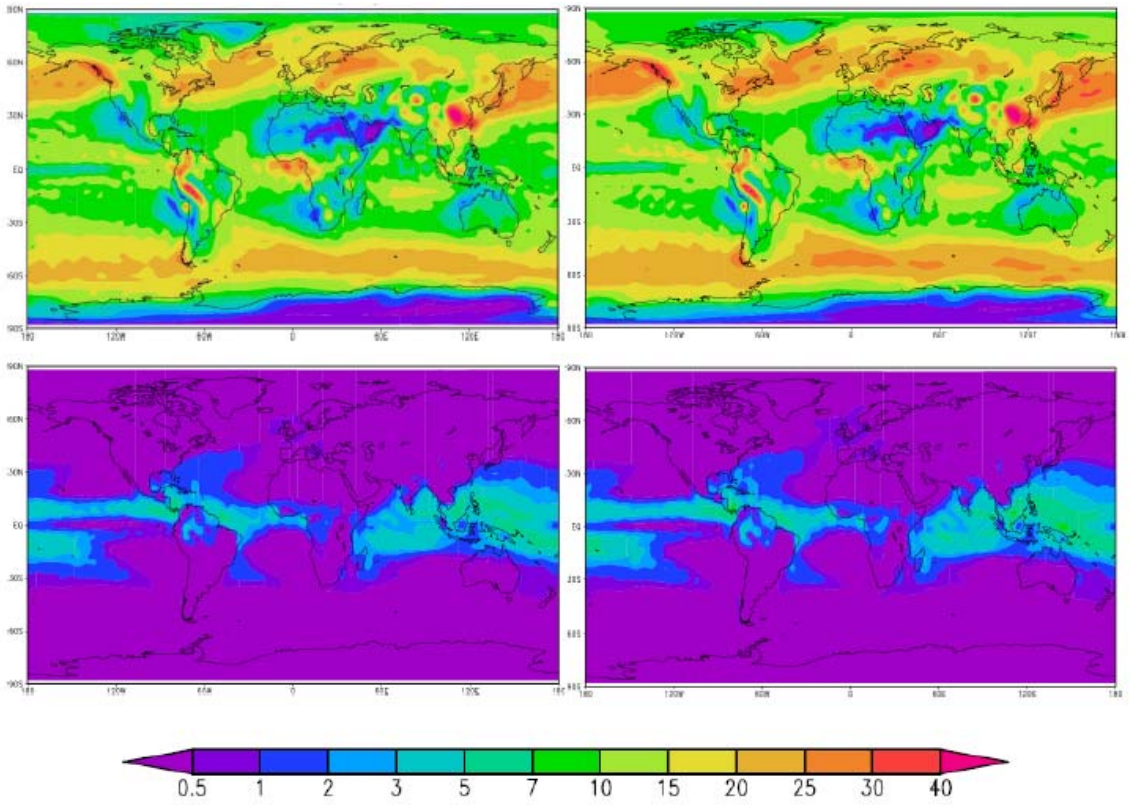

Fig. 3-5. Annual mean distributions of cloud optical thickness (COT) for large scale clouds (top) and cumulus (bottom) in SPstd (left) and SPnew (right) models.

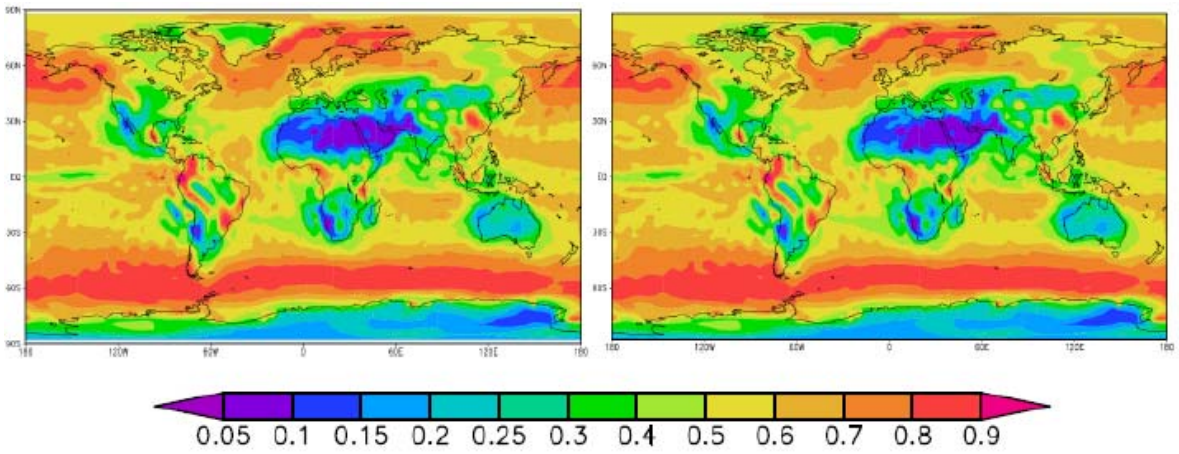

Fig. 3-6. Annual mean distributions of cloud cover fraction in SPstd (left) and SPnew (right) models.

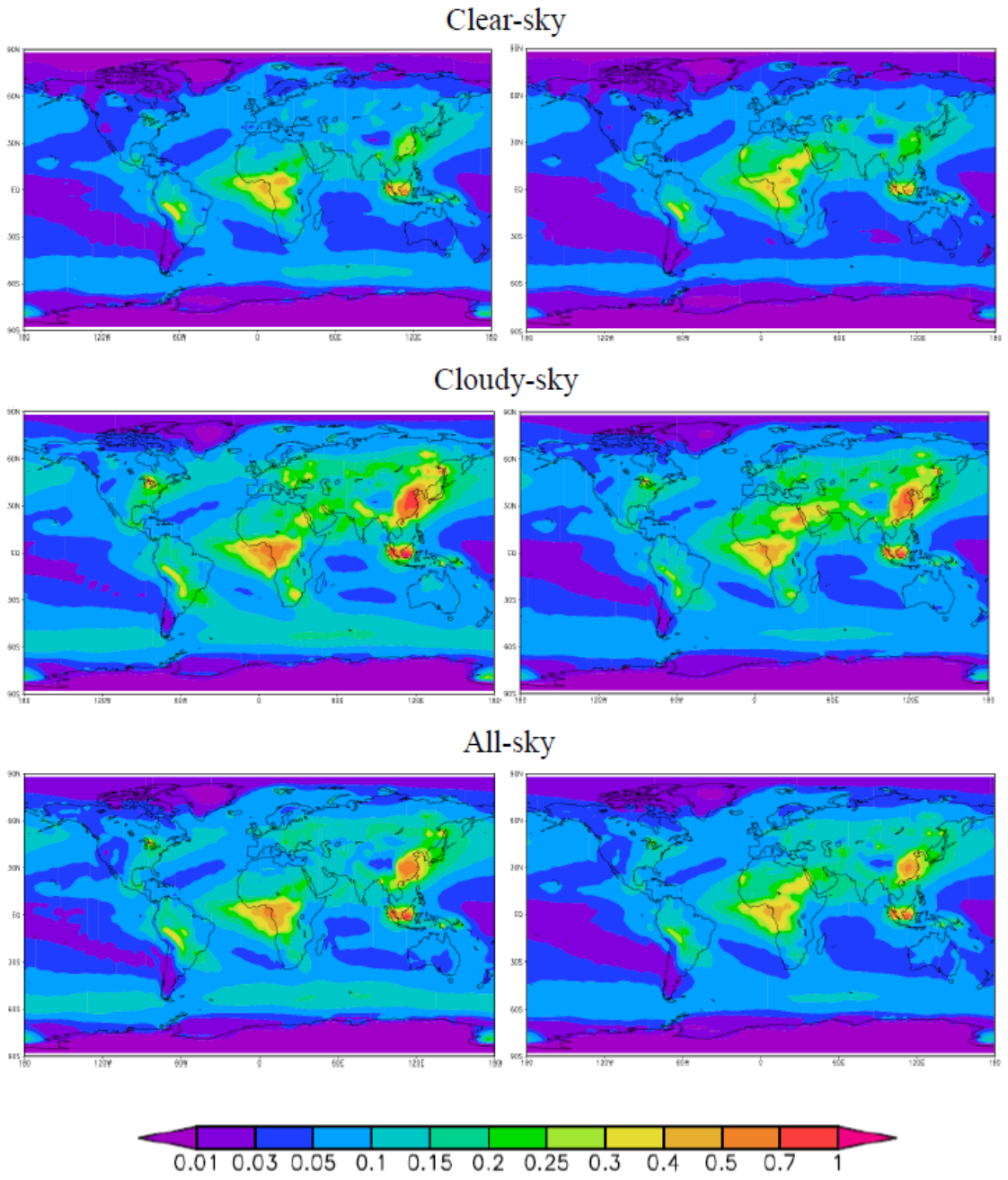

Fig. 3-7. Annual mean distributions of AOT (435-678 nm) under clear-sky (top), cloudy-sky (middle), and all-sky (bottom) conditions in SPstd (left) and SPnew (right) models.

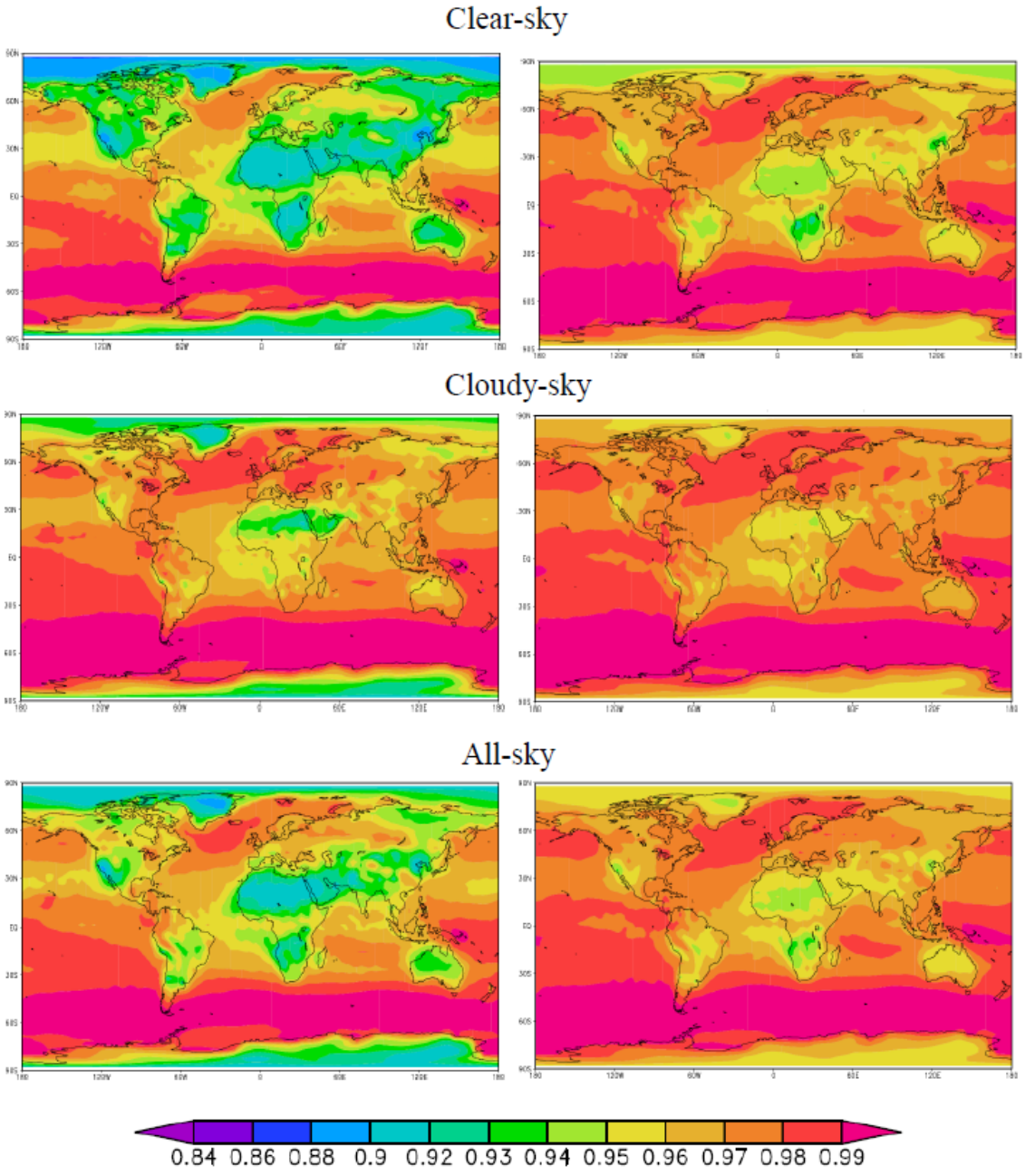

Fig. 3-8. Same as Fig. 3-7, but annual mean distributions of SSA (435-678 nm).

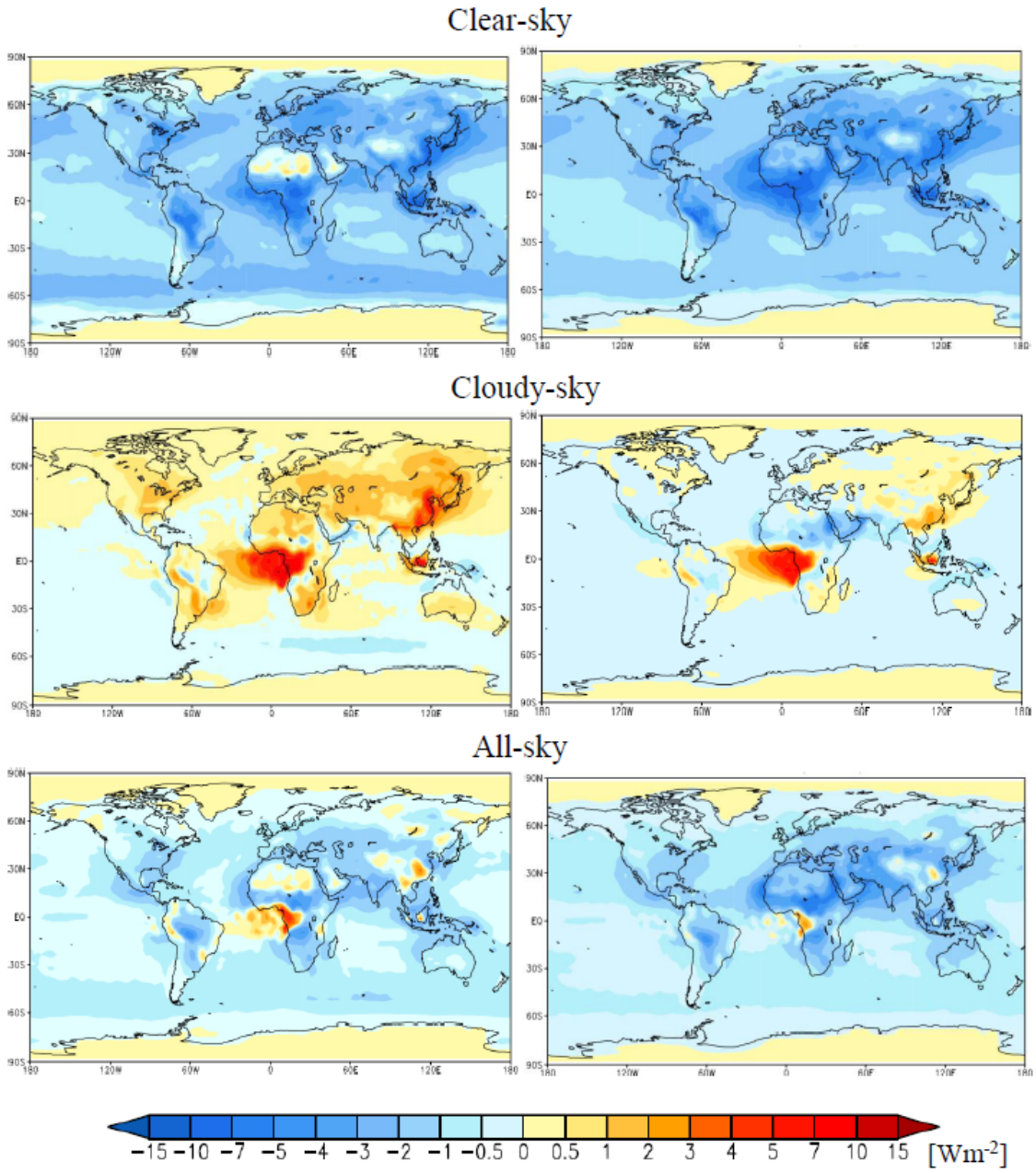

Fig. 3-9. Same as Fig. 3-7, but annual mean distributions of SWDARF.

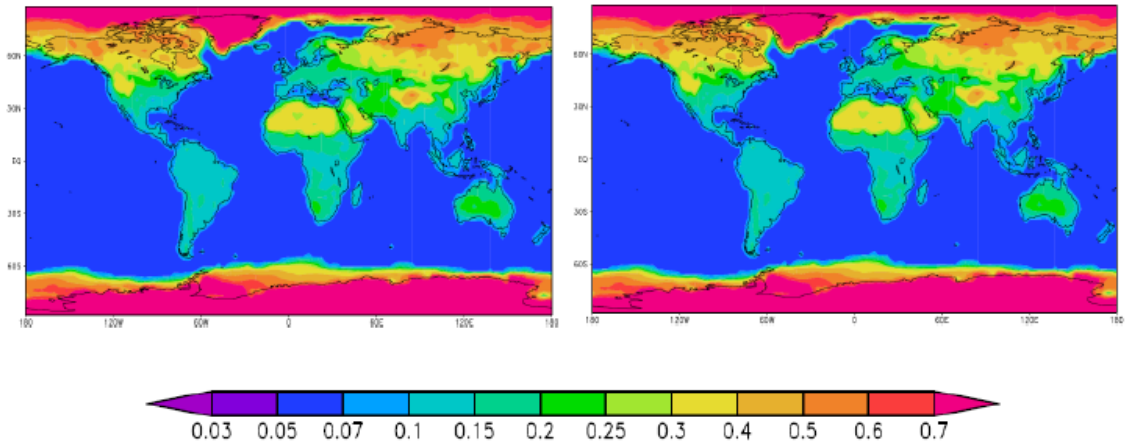

Fig. 3-10. Annual mean distributions of shortwave surface albedo in SPstd (left) and SPnew (right) models.

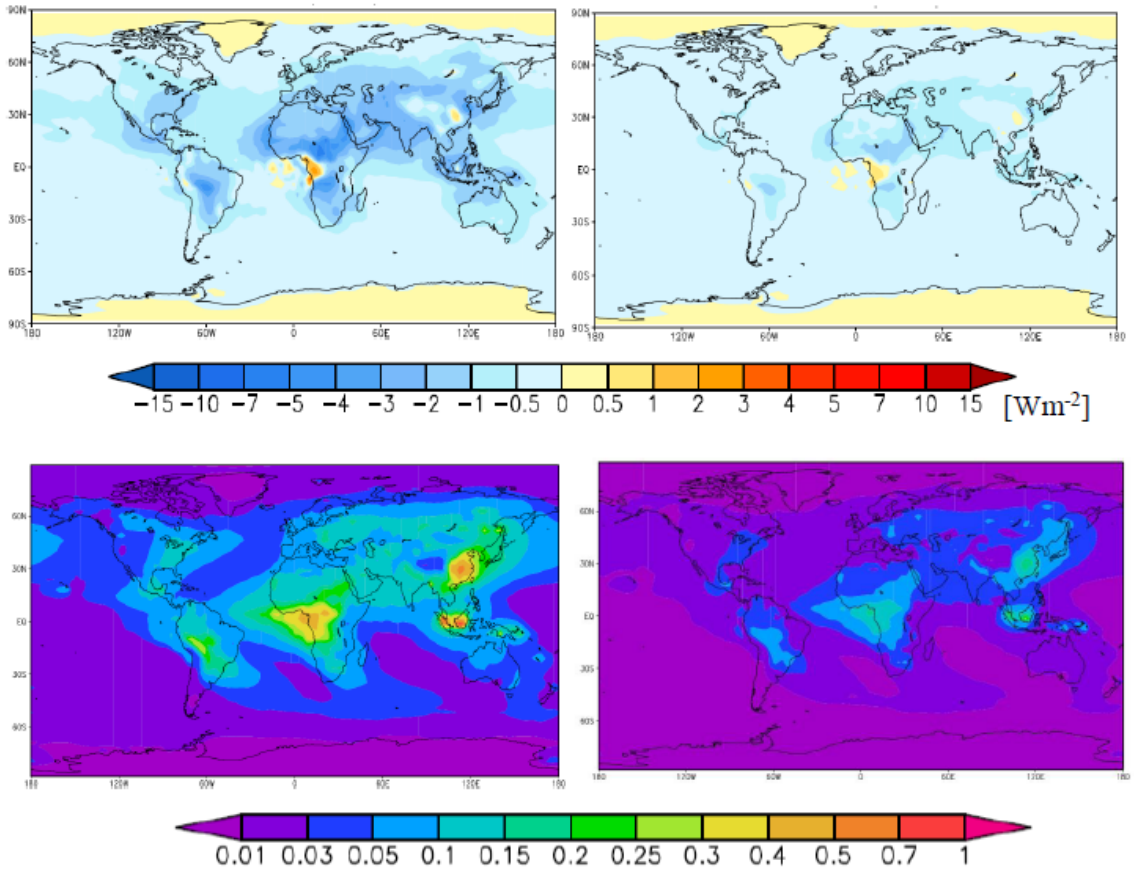

Fig. 3-11. Annual mean distributions of SWDARF (top) and AOT (435-678 nm) (bottom) for fine mode aerosols (left) and anthropogenic aerosols (right) in the SPnew model.

4. Comparison between the observation and model results

SWDARFs using CALIPSO and MODIS observations are calculated in chapter 2 and MIROC model simulation is performed in chapter 3. The clear-sky SWDARF of total aerosols from MIROC is smaller than other studies [*Yu et al*., 2006]. The reason for this discrepancy has not yet been revealed by past studies; thus, I tried to find out this reason by comparison of aerosol optical properties and SWDARFs among CALIPSO, MIROC model, and other studies.

In this chapter, some of key figures are shown again to summarize the findings in this thesis and for better understanding of our knowledge on the aerosol radiative forcing. All the figures cover the zonal regions between 60°S and 60°N for comparison of CALIPSO and MIROC results.

In this chapter, optical thickness, extinction coefficient, and SSA for aerosols are compared among some observations and the modeling. Wavelengths of aerosol optical properties are 532 nm for CALIPSO V3 product, the weighted average between 435 and 678 nm for mstrnX in the SPnew model, and 550 nm for MODIS and AERONET observations. These wavelength differences are ignored, because the differences of aerosol optical properties between the model and observations are much larger than those caused by the differences of the wavelengths.

4.1 Sensitivity test of the model for surface albedo

The surface albedo, which changes the outgoing radiative fluxes at the TOA, is one of important parameters for controlling the SWDARF. Figure 4-1 shows annual mean distributions of shortwave surface albedo of MODIS observation used in CALIPSO radiation calculation and those of SPnew model. In the CALIPSO radiation calculation, the ocean surface albedo is calculated by FSTAR radiation code with use of the surface wind velocity of MERRA reanalysis data. It is found that SPnew surface albedo is larger than CALIPSO surface albedo over Russia, Canada and Himalaya Mountains, where snow covers the ground over a long period of the year. The ocean albedo of CALIPSO is 0.04 and that of SPnew model is 0.05. A sensitivity test that changes surface albedo from the value of SPnew model to that multiplied by 0.8 (ALB*0.8) is performed. The ALB*0.8 experiment brings the ocean albedo to that of CALIPSO for examining the impact of surface albedo on SWDARF. The resulting annual mean values of SWDARF for the ALB*0.8 experiment between 60°S and 60°N are –2.33, –0.10, and –1.20 Wm^{-2} under clear-sky, cloudy-sky, and all-sky conditions. Compared with SPnew results, differences of the clear-sky and all-sky SWDARF are 0.2 and 0.1 Wm^{-2}, respectively, which are much smaller than the difference of the clear-sky SWDARF between SPnew

and the satellite-based and also model-based averages of *Yu et al*. [2006] as shown in Fig. 1-1. This indicates that the difference in surface albedo values between observation and model is not a major reason that explains the difference of SWDARF between MIROC-SPRINTARS and other studies.

4.2 Comparison of aerosol vertical distributions between CALIPSO and MIROC under clear-sky condition

The clear-sky AOT of SPnew is smaller than that of CALIPSO V3 (Tables 2-3 and 3-5). The vertical profiles of aerosol extinction coefficient from surface to 20 km altitude are retrieved by CALIPSO observations under clear-sky condition. Figure 4-2 shows the annual mean vertical profiles of aerosol extinction coefficient between 60°S and 60°N for CALIPSO and SPnew under clear-sky condition. The extinction coefficient of SPnew is smaller than that of CALIPSO below 4 km altitude, while that of SPnew is larger than that of CALIPSO above 4 km altitude. On the other hand, it is possible that CALIPSO extinction coefficient is underestimated above 4 km altitude, because the aerosol extinction is lower than the CALIPSO lidar detection threshold [*Winker et al*., 2013]. The ratios of CALIPSO AOT to SPnew AOT (CALIPSO AOT / SPnew AOT) are 2.14 below 4 km and 0.29 above 4 km altitude (Table 4-1). In order to study the effect of this difference, I simply performed a model simulation that aerosol concentrations are multiplied by the ratios of 2.14 below 4 km altitude and 0.29 above 4 km altitude in the SPnew model. This simulation is referred to as the SP4km experiment. Though it is possible that the CALIPSO extinction coefficient is underestimated above 4 km altitude, this is used in CALIPSO radiation calculation and this simple multiplying method is applied to the aerosol profile simulated in the model. The profile of SP4km experiment is similar to the CALIPSO profile, but is slightly smaller below 1.5 km altitude and slightly larger between 1.5 and 4.5 km altitudes than CALIPSO profile (Fig. 4-2).

Figure 4-3 shows annual mean distributions of AOT for CALIPSO V3 product and SPnew and SP4km experiments under clear-sky condition. These are compared with AOT retrieved by the Aqua-MODIS sensor. The geographical pattern of CALIPSO AOT is similar to that of MODIS observations, and the magnitude of CALIPSO AOT is smaller than that of MODIS AOT over ocean and North America. The past studies suggested that MODIS AOT tends to be overestimated by about 10 to 15% because of contamination of thin cirrus [*Kaufman et al.*, 2005]. On the other hand, CALIPSO AOT is likely to be underestimated due to the detection limit of CALIPSO lidar as already discussed above; hence, the CALIPSO AOT is generally smaller than MODIS AOT by

these reasons. In this regard, it should be noted that the SPnew AOT is further smaller than the observed CALIPSO AOTs in almost all regions. This suggests a high possibility of underestimation of AOT by the model. On the other hand, the geographical pattern and magnitude of SP4km AOT becomes close to those of the observed AOTs, though the modeled AOT is still underestimated over India and ocean atlow latitudes. The zonal average of AOT between 60°S and 60°N for SP4km experiment is 0.128, which is comparable to that for CALIPSO, 0.127, so that the vertical profile of SP4km is considered to be more realistic than the original profile in the SPnew.

Figure 4-4 shows annual mean vertical profiles of aerosol extinction coefficient, which are averaged in the 30 degrees latitudinal zone for CALIPSO, SPnew, and SP4km under clear-sky condition. On the basis of CALIPSO observations, high concentrated aerosols globally exist lower than 2 km altitude, in particular, aerosol extinction coefficient is larger than 0.05 lower than 1 km altitude. In addition, aerosols are elevated up to 5 km altitude over land. On the other hand, in SPnew model, aerosols are elevated up to 7 km altitude around the emissions of carbonaceous aerosols and dust, while aerosol extinction coefficient is globally underestimated below 2 km altitude. In SP4km experiment, aerosol concentrations are increased from surface to 4 km altitude due to the design of the SP4km experiment. The vertical distributions of aerosol extinction coefficient become close to CALIPSO. In more detail, the aerosol extinction coefficient is overestimated over East Asia, the Sahara, central Africa, Mexico, and from 2 to 4 km altitude over the North Pacific (Fig. 4-4(b)). These results indicate that aerosols are easily transported in a vertical direction, but are hardly transported in a horizontal direction in MIROC. It will be concluded that this bias of the aerosol transportation is caused by aerosol modeling process, not by circulation modeling, because the MIROC simulation is performed in this study with nudged meteorological fields of NCEP/NCAR reanalysis data.

4.3 Comparison of SWDARF from the observation and modeling

In the previous section, AOTs and aerosol vertical distributions under clear-sky condition for SPnew model and CALIPSO are compared. In this section, differences among the SWDARFs of CALIPSO V3 product and SPnew and SP4km experiments are discussed. For this purpose, I first study global distributions of SSAs and AOTs from the observations and modeling, because these parameters are the main parameters to determine the SWDARF.

Figure 4-5 shows annual mean distributions of SSA for CALIPSO V3 product (532

nm) and SPnew and SP4km experiments (435-678 nm) under clear-sky condition. These can be compared with SSA retrieved by the ground sun/sky radiometer observation of AERONET. AERONET SSA at 550 nm is interpolated using SSAs at 440 and 675 nm and the original quality control (see Appendix C). When compared with AERONET SSA, CALIPSO SSA is underestimated and SSAs of SPnew and SP4km are overestimated. CALIPSO SSA largely depends on the optical properties of the aerosol model assumed in the retrieval algorithm, because it is difficult to estimate the absorption properties of aerosols by a Mie lidar. For this reason, CALIPSO SSA is assumed to have a large uncertainty.

Table 4-2 summarizes the annual mean values of AOT for dust, carbonaceous aerosols, sulfate, sea salt, and total aerosols in SPnew and SP4km experiments. In MIROC, dust and carbonaceous aerosols are transported to the upper troposphere (Fig. 4-4). As a result, the ratios of increment of AOT from SPnew to SP4km for sea salt and sulfate are larger than those for dust and carbonaceous aerosols. The fractions of AOT for sea salt and sulfate to total aerosols relatively become larger, so that SSA becomes larger over ocean than SPnew results.

Figure 4-6 shows annual mean distributions of the clear-sky SWDARF for CALIPSO V3 product and SPnew and SP4km experiments. The SP4km SWDARF is more negative than SPnew SWDARF, because aerosol amount increases in the lower troposphere. The SPnew SWDARF is smaller negative than that of CALIPSO, except for Saharan and Arabian deserts. In these regions, CALIPSO SWDARF takes a positive value of +3 Wm^{-2} due to the high surface albedo of 0.3 and low SSA of 0.9. On the other hand, in SPnew model, the surface albedo is 0.3 but SSA is larger than 0.94, so that aerosol absorption is not enough to change the sign of the forcing from negative to positive.

The average values of resulting SWDARFs for total aerosols under clear-sky, cloudy-sky, and all-sky conditions for CALIPSO V3 product and the SPnew, SPnew(ALB*0.8), and SP4km experiments are listed in Table 4-3. A zonally averaged AOT between 60°S and 60°N of SP4km is comparable to CALIPSO AOT, and SSA of SP4km is larger than that of CALIPSO, but the zonal average SWDARF is less negative than CALIPSO by 0.5 Wm^{-2}. Over the North Pacific, the aerosol extinction coefficient of SP4km is larger than that of CALIPSO from 2 to 4 km altitude (Fig. 4-4), but column AOT and SWDARF are similar between SP4km and CALIPSO (Figs. 4-3 and 4-6). Over Saharan and Arabian deserts, the SPnew model shows a negative forcing, while CALIPSO SWDARF indicates positive. In these regions, the surface albedo is larger than 0.3 in both the observation and modeling, whereas the observation SSA is 0.9 and

the model SSA is 0.94. This SSA difference changes the sign of SWDARF, but this phenomenon is mainly caused in these regions and there is little effect of the global estimation of SWDARF. Over ocean in the southern hemisphere, the aerosol extinction coefficient of SP4km is smaller than that of CALIPSO below 2 km altitude and SWDARF of SP4km is less negative than that of CALIPSO. These results indicate that the SWDARF difference between SP4km and CALIPSO is mainly caused by the underestimation of aerosol extinction coefficient below 2 km altitude over ocean in the southern hemisphere.

Figure 4-7 shows annual mean distributions of the cloudy-sky and all-sky SWDARFs for CALIPSO V3 product and SPnew and SP4km experiments. Over Saharan and Arabian deserts, CALIPSO SWDARF is positive under clear-sky, cloudy-sky, and all-sky conditions. This positive value is caused by a dust SSA of 0.92 and surface albedo larger than 0.3, regardless of cloud existence. Figure 4-8 shows the seasonal mean extinction profiles for aerosols and clouds of SPnew and SP4km experiments in the cloudy-sky condition corresponding to the vertical profiles of CALIPSO in Figs. 2-12 and 2-13. Off southern Africa, aerosol layers are usually undetected below 1.5 km altitude by CALIPSO observations in above-cloud case, whereas aerosols are simulated from surface to 5 km altitude in the model. In cloudy-sky condition, the modeled SWDARF is more positive than the observation, because the aerosol absorption of elevated aerosols above the planetary boundary layer is enhanced by the higher cloud reflectance derived from optically thick clouds. Over the central and North Pacific, optically thick clouds are simulated in the free troposphere in the model, so that clouds mainly scatter sunlight and aerosols cause less negative forcing than the CALIPSO case. These results indicate that optically thick clouds simulated in MIROC lead large positive forcing of aerosols near source regions of black carbon and small negative forcing of transported aerosols.

From section 2.5.3, aerosols cause a small negative or positive forcings in above-cloud and cloudy-undetected cases, though the SWDARFs in clear-sky and below-cloud cases are negative except for the bright surfaces. I presume that the sum of the occurrence probabilities of above-cloud and cloudy-undetected cases is an important parameter for controlling the all-sky SWADARF. Figure 4-9 shows annual mean distributions of sum of the occurrence probabilities of above-cloud and cloudy-undetected cases in CALIPSO V3 product. This CALIPSO occurrence probability is corresponding to cloud fraction of clouds with COT larger than 3 in SPnew model. It is found from the figure that the CALIPSO occurrence probability is lower over ocean and higher over land than that of the model. In the model, the all-sky

SWDARF is positive over the central Africa and East Asia, where this occurrence probability is higher than 0.5. In CALIPSO case, the all-sky SWDARF in the regions, where this occurrence probability is lower than 0.3, is more negative than that in the regions where the occurrence probability is higher than 0.3. These results indicate that the reproducibility of COT in the modeling is important for the estimation of SWDARF.

From these results, I presume two major reasons that MIROC SWDARF is smaller negative than CALIPSO SWADARF. One is that aerosols are easily transported in a vertical direction, but are hardly transported in a horizontal direction in MIROC. The other is that MIROC frequently simulate optically thicker clouds than the observation. By these two reasons, carbonaceous aerosols elevated to a high altitude are transported above clouds and cause strong positive forcing over the central Africa and East Asia and few aerosols causes small negative forcing over remote oceans.

4.4 Comparison of anthropogenic SWDARF from observation and modeling

The DARF of anthropogenic aerosols is usually defined as a radiative flux changes at TOA or at the climatological tropopause, between pre-industrial and present-day by the model simulation [e.g. *Myhre et al.*, 2013]. Recently, *Bellouin et al*. [2008] estimated the anthropogenic SWDARF from the MODIS-derived AOT using their algorithms that calculate the anthropogenic fraction of AOT. In this study, SWDARFs of anthropogenic aerosols are derived using CALIPSO V3 product and the present-day model simulation of the SPnew model. The value of anthropogenic fraction of AOT is referred to the average value of AeroCom models in *Myhre et al*. [2013] (see sections 2.5.5 and 3.3.3).

From Figs. 2-20 and 3-11, anthropogenic AOT is found to be larger than 0.03 and SWDARF is larger negative than –0.5 Wm^{-2} in near source regions in the observation and model. On the other hand, AOT is less than 0.01 over the central Pacific. The modeled all-sky SWDARF shows a positive forcing over central Africa and East Asia, because the cloud fraction is larger than 0.6 and COT is larger than 20; therefore, aerosol absorption is enhanced by the high reflectance from clouds [*Haywood and Shine*, 1997; *Takemura et al*., 2005] in cloudy-sky condition. On the other hand, the occurrence probability of above-cloud case is less than 0.3 and AOT is larger than 0.3 in CALIPSO; therefore, SWDARF is larger negative than –0.5 Wm^{-2}. From these differences, the zonal averages between 60^{o}S and 60^{o}N of the all-sky anthropogenic SWDARF become different as –0.57 and –0.26 Wm^{-2} in the observation and the model.

Figure 4-10 shows a scatter plot between anthropogenic DARF and AOT under clear-sky and all-sky conditions for CALIPSO V3 product, SPnew model, and other

studies. Anthropogenic SWDARF of MODIS [*Bellouin et al*., 2008] is more negative than AeroCom studies [*Schulz et al.*, 2006; *Myhre et al*., 2013] under clear-sky and all-sky conditions. *Bellouin et al*. [2008] assumed the cloudy-sky SWDARF as zero, because aerosols are not retrieved by MODIS in cloudy-sky condition. *Schulz et al.* [2006] indicated the model average of cloudy-sky SWDARF is +0.05 Wm^{-2}, which is close to the cloudy-sky forcing of MODIS. The clear-sky SWDARF of MODIS is twice as large as those of AeroCom studies, so that the all-sky SWDARF of MODIS is also twice larger than that of AeroCom studies. The clear-sky SWDARFs of CALIPSO and SPnew are comparable to those of AeroCom studies within the margin of standard deviation for multi-model ensembles. The all-sky SWDARF of SPnew is comparable to those of AeroCom studies. On the other hand, the all-sky SWDARF of CALIPSO is more negative than those of AeroCom studies, because the cloudy-sky SWDARF is –0.37 Wm^{-2}. The all-sky SWDARF of CALIPSO is negative in all regions, while the SPnew model and some of AeroCom models show positive forcing off southern Africa and other regions. This difference is mainly caused by the model reproducibility of the stratification of aerosol and cloud layers, which is discussed in the previous section. These results show the uncertainty of the cloudy-sky SWDARF is larger than that of the clear-sky SWDARF.

The challenge to evaluate anthropogenic DARF from the present-day observation and simulation is useful to reduce uncertainties of anthropogenic DARF estimated by the flux changes at the TOA between pre-industrial and present-day model simulations.

4.5. Summary of comparison between the observation and modeling

The vertical profiles of aerosols are globally observed by CALIPSO lidar under clear-sky condition. High concentrated aerosols are globally observed lower than 2 km altitude by CALIPSO; in particular, aerosol extinction coefficient is larger than 0.05 at altitude lower than 1 km. On the other hand, the aerosol extinction coefficient in SPnew model is globally underestimated below 2 km altitude, while aerosols are elevated up to 7 km altitude around source regions of carbonaceous aerosols and dust in the model. These results indicate that aerosols are transported higher than the observation in a vertical direction, but are hardly transported in a horizontal direction in MIROC.

In clear-sky condition, CALIPSO AOT is smaller than MODIS AOT by 20%. MODIS AOT tends to be overestimated by about 10 to 15%, because of contamination of thin cirrus [*Kaufman et al.*, 2005]. On the other hand, CALIPSO AOT is likely to be underestimated due to the detection limit of CALIPSO lidar [*Winker et al*., 2013]. By these reasons, more realistic values of the clear-sky AOT and SWDARF seem to be the

values of CALIPSO AOT and SWDARF increased by 10%. I presume that the best estimate of the clear-sky SWDARF is –4.1 Wm^{-2}. The magnitude of the negative forcings for both CALIPSO and model seem to be underestimated under clear-sky condition.

There are many uncertainties in the estimation of the all-sky SWDARF. The vertical profiles of aerosols and clouds below the top of the optically thick clouds are not observed by CALIPSO. This uncertainty is included in the estimated CALIPSO SWDARFs in above-cloud, cloudy-undetected, and all-sky cases. On the other hand, the vertical profiles of aerosols and clouds are simulated from surface to the stratosphere in the model, but MIROC frequently simulate optically thinner aerosols and optically thicker clouds than the observation. By these reasons, the average of the all-sky SWDARF for CALIPSO V3 product and SP4km experiment may be better than the value estimated by only the observation or the model, so that I like to conclude that the best estimate of the all-sky SWDARF is –1.9 Wm^{-2}.

Figure 4-11 summarizes annual mean values of the clear-sky and all-sky SWDARFs derived from this study and previous studies. In reference to previous studies of *Liu et al*. [2007], *Kim and Ramanathan* [2008], *Ma et al.* [2012], *Zhang et al.* [2012], and *Kinne et al.* [2013], the average values of the clear-sky and all-sky SWDARFs are –4.8 $\pm$0.8 Wm^{-2} and –2.7$\pm$0.9 Wm^{-2}. These previous studies are referred to as Refs2007 and the errors are standard deviations. The best estimate of clear-sky SWDARF in this study, –4.1 Wm^{-2}, is between the multi-satellite observations and multi-models of *Yu et al*. [2006]. The best estimates of clear-sky and all-sky SWDARFs in this study are located in between the CALIPSO values in this study and that of Refs2007.

Table 4-1. Annual mean column AOT, AOT below 4 km altitude, AOT above 4 km altitude between 60°S and 60°N for CALIPSO V3 product and SPnew model under clear-sky condition. AOT (532 nm) for CALIPSO V3 product and AOT (435-678 nm) for SPnew model and the ratio of CALIPSO AOT to SPnew AOT (CALIPSO AOT / SPnew AOT) are listed.

	CALIPSO(V3)	SPnew	Ratio
AOT (column)	0.127	0.076	1.67
AOT (below 4km)	0.122	0.057	2.14
AOT (above 4km)	0.006	0.021	0.29

Table 4-2. Annual mean values of AOT (435-678 nm) between 60°S and 60°N for dust, carbonaceous aerosols, sulfate, sea salt, and total aerosols under clear-sky, cloudy-sky, and all-sky conditions in SPnew and SP4km experiments.

	Dust	Carbonaceous	Sulfate	Sea salt	Total
	SPnew experiment				
Clear-sky	0.015	0.028	0.019	0.014	0.076
Cloudy-sky	0.015	0.037	0.033	0.020	0.104
All-sky	0.015	0.032	0.025	0.018	0.091
	SP4km experiment				
Clear-sky	0.020	0.044	0.041	0.030	0.128
Cloudy-sky	0.019	0.055	0.045	0.042	0.169
All-sky	0.020	0.050	0.042	0.038	0.150

Table 4-3. Annual mean SWDARF [Wm^{-2}] between 60°S and 60°N under clear-sky, cloudy-sky, and all-sky cases for the average of CALIPSO V3 calculations and the SPnew, SPnew(ALB*0.8), and SP4km experiments.

	Clear-sky	Cloudy-sky	All-sky
CAL V3 (ave)	-3.7	-1.0	-2.0
SPnew	-2.1	-0.1	-1.1
SPnew(ALB*0.8)	-2.3	-0.1	-1.2
SP4km	-3.2	-0.3	-1.7

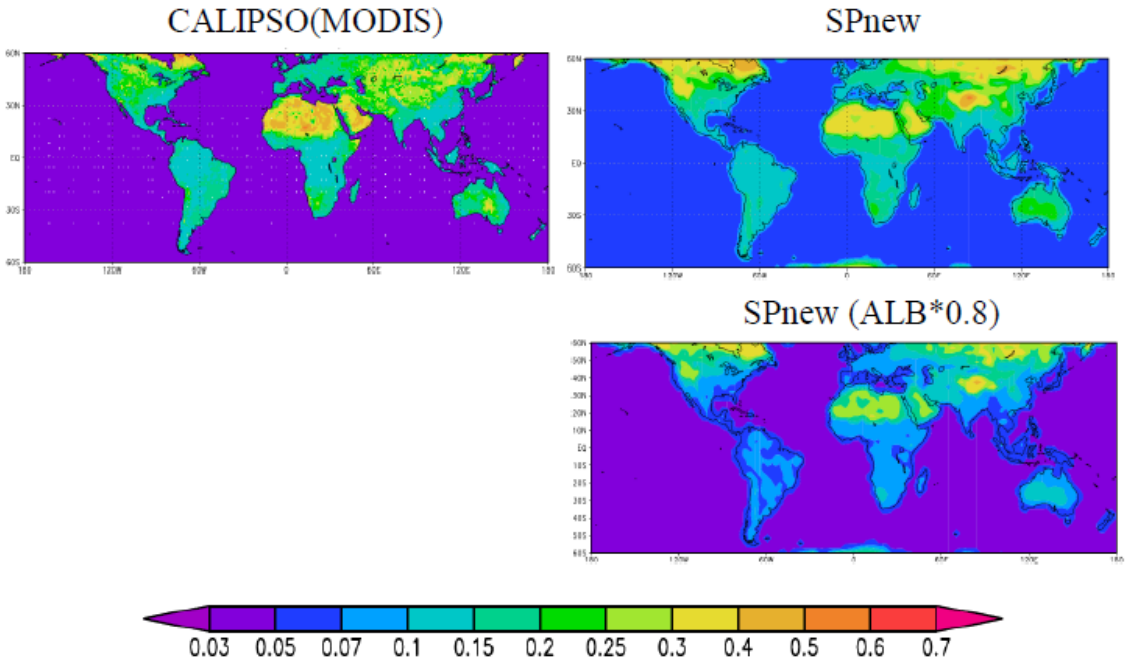

Fig. 4-1. Annual mean distributions of shortwave surface albedo for MODIS observation used in CALIPSO radiation calculation (left) and SPnew model (right top), and that of SPnew model multipled by 0.8 (right bottom).

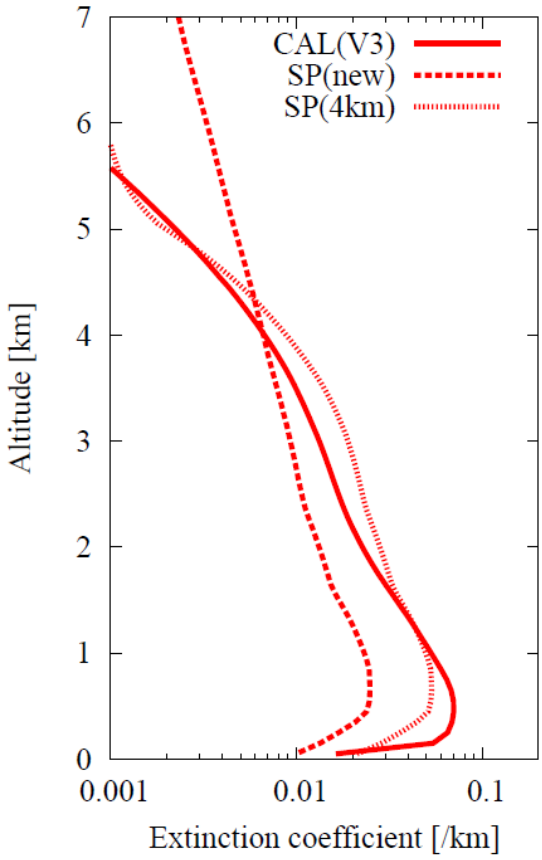

Fig. 4-2. Annual mean vertical profiles of aerosol extinction coefficient between 60°S and 60°N for CALIPSO V3 product (532 nm) and SPnew model (435-678 nm) under clear-sky condition.

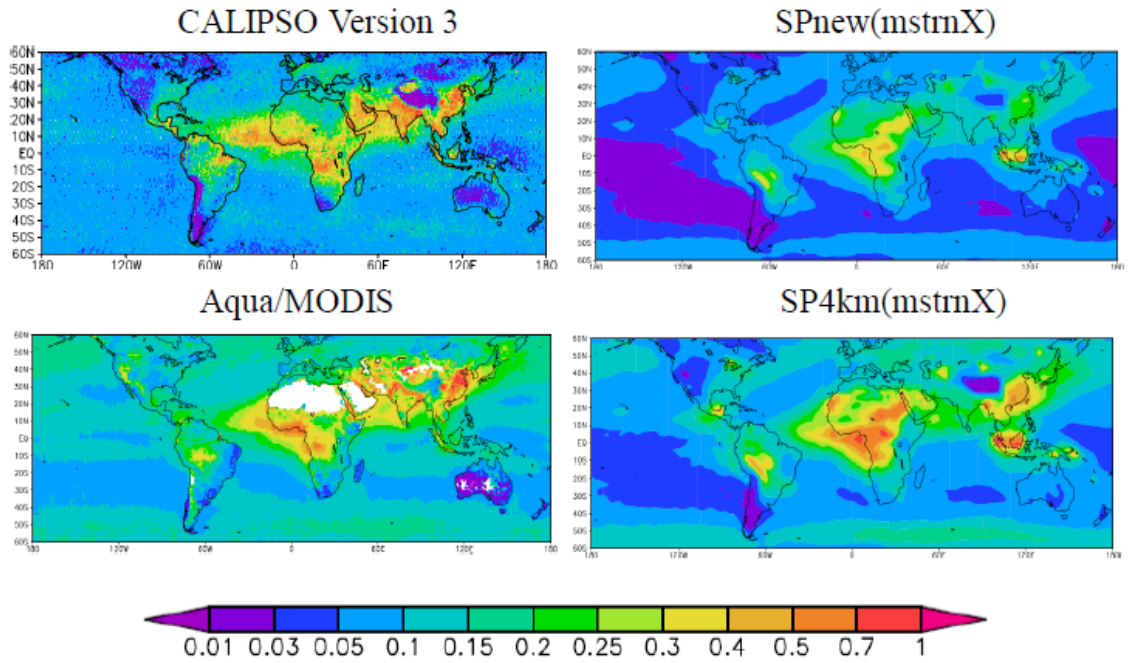

Fig. 4-3. Annual mean distributions of AOT for CALIPSO V3 product (532 nm), SPnew and SP4km experiments (435-678 nm), and Aqua MODIS (550 nm) under clear-sky condition.

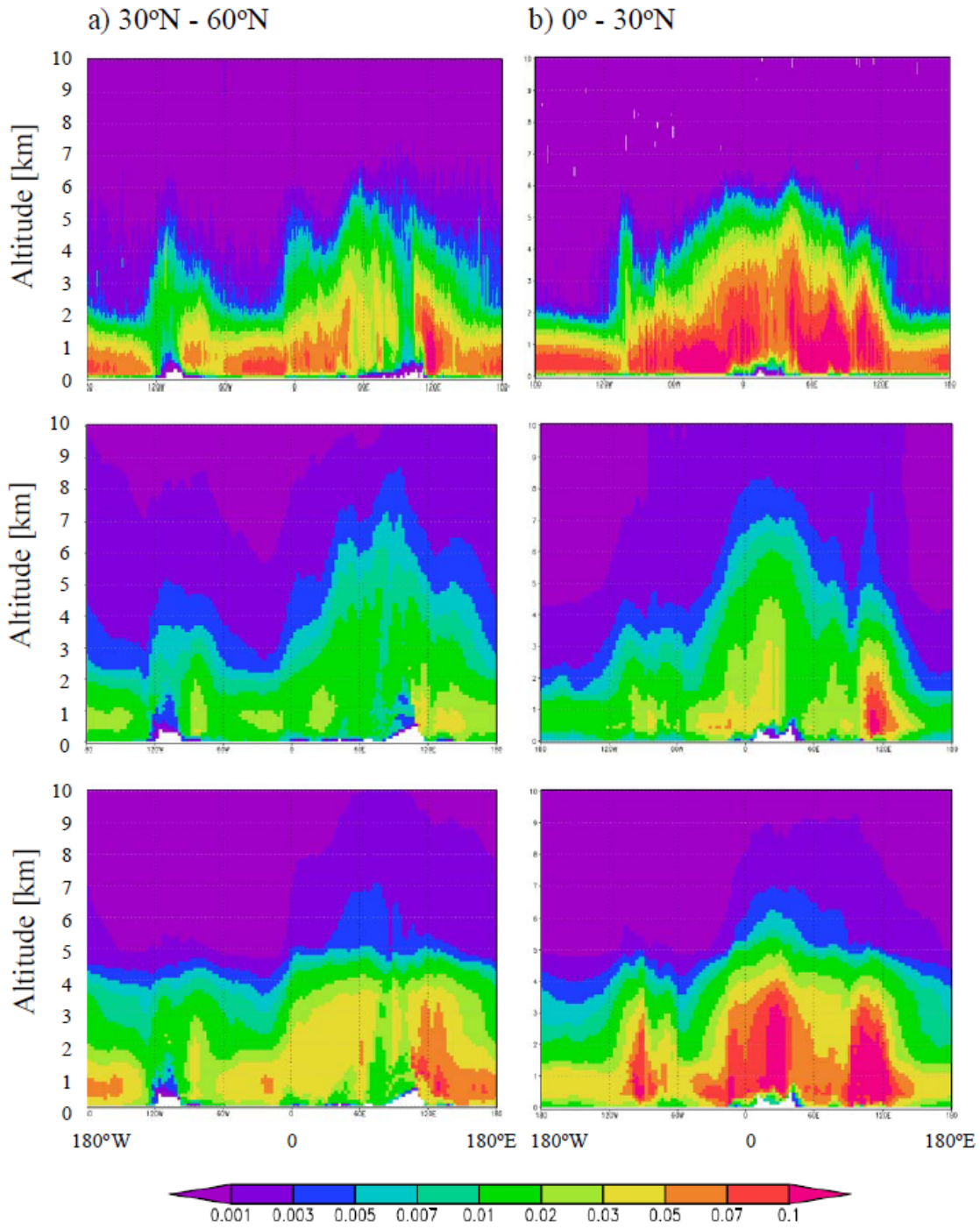

Fig. 4-4. Annual mean vertical profiles of aerosol extinction coefficient for CALIPSO (top), SPnew (middle), and SP4km (bottom) under clear-sky condition. These profiles are averaged in the 30 degrees latitudinal zone (60°S - 30°S (a), 30°S - 0° (b), 0° - 30°N(c), and 30°°N - 60°N (d)).

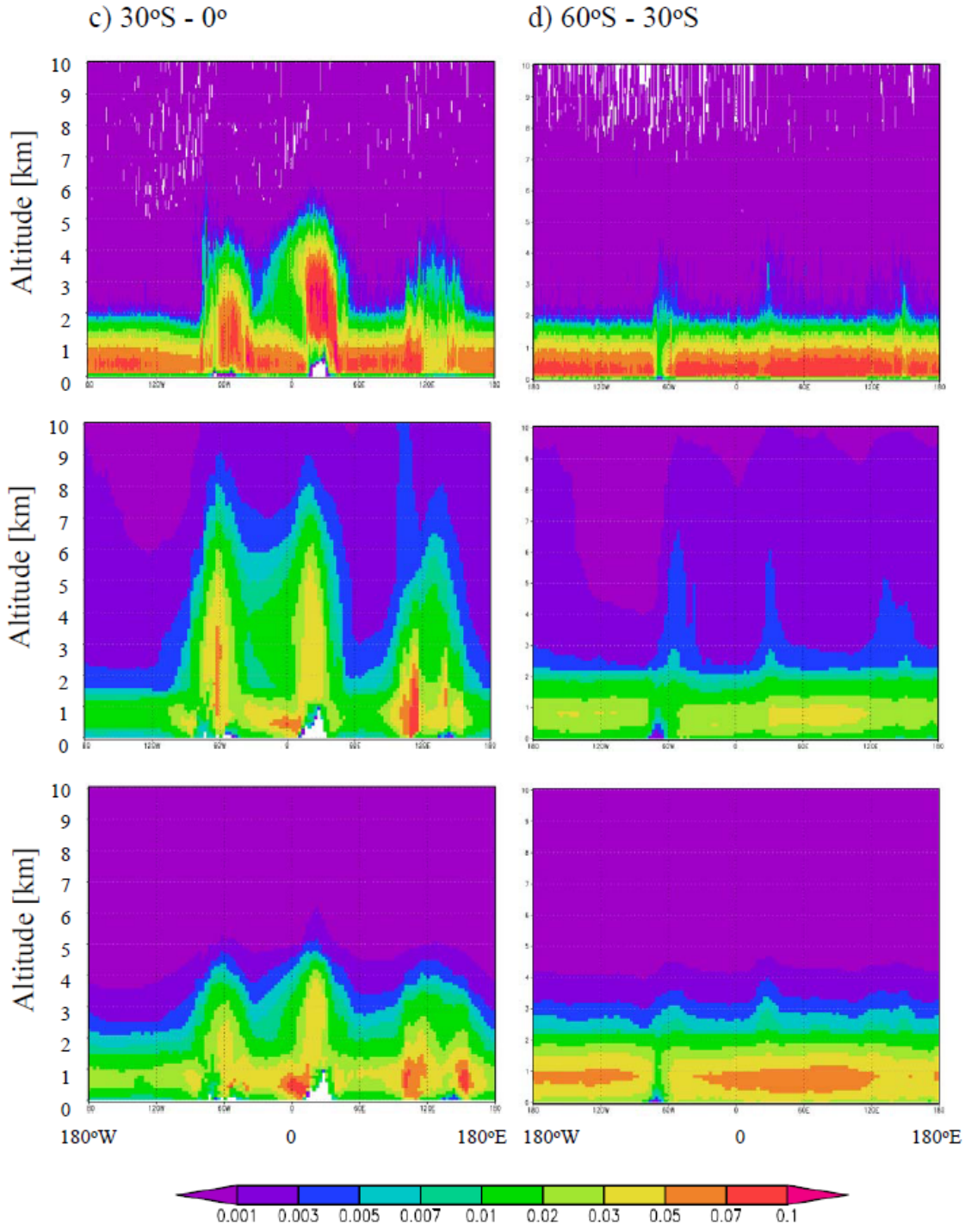

Fig. 4-4. (continued)

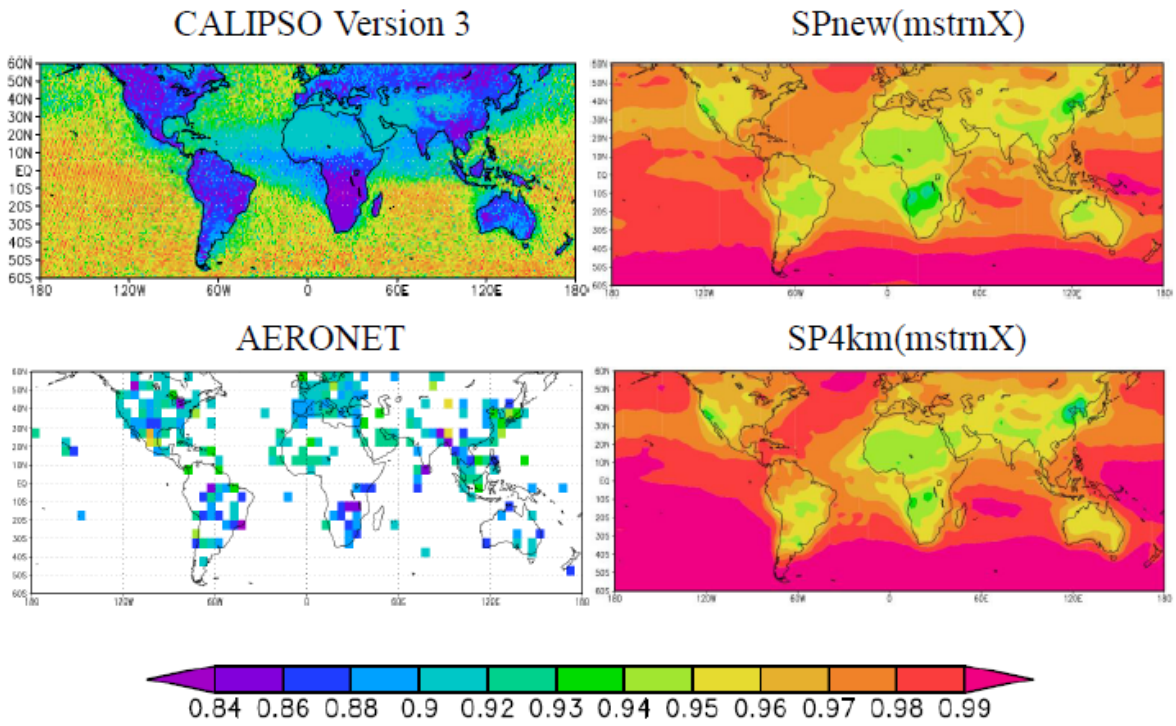

Fig. 4-5. Annual mean distributions of SSA of total aerosols for CALIPSO V3 product (532 nm), SPnew and SP4km experiments (435-678 nm), and AERONET (550 nm) under clear-sky condition.

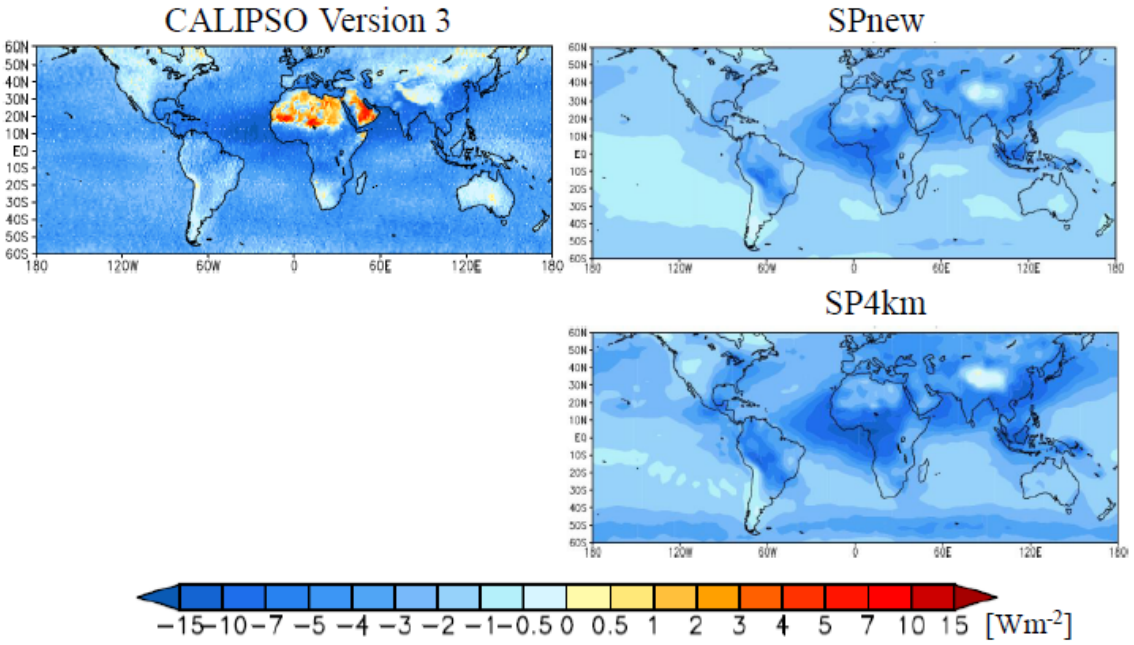

Fig. 4-6. Annual mean distributions of the clear-sky SWDARF for CALIPSO V3 product and SPnew and SP4km experiments.

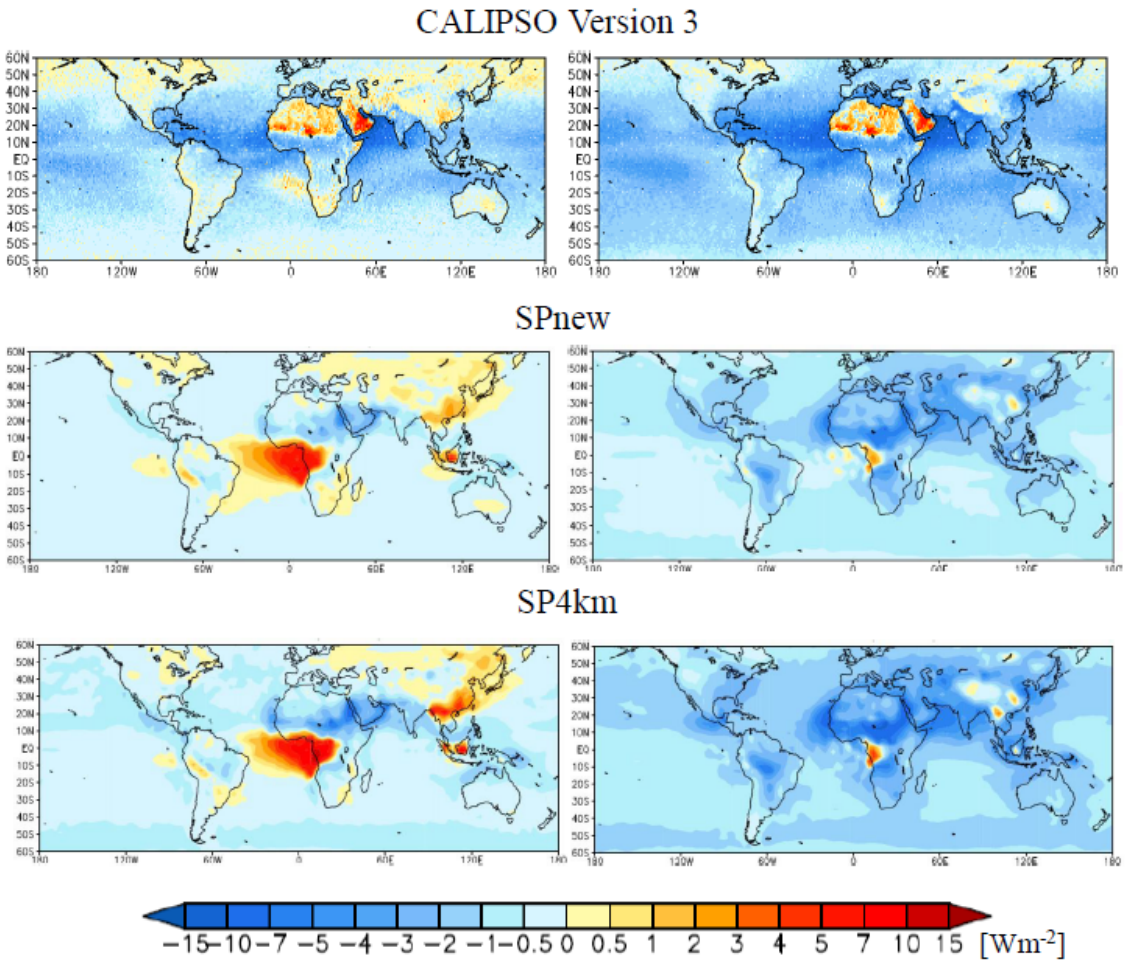

Fig. 4-7. Annual mean distributions of the cloudy-sky (leff) and all-sky (right) SWDARFs for CALIPSO V3 product (top) and SPnew (middle) and SP4km (bottom) experiments.

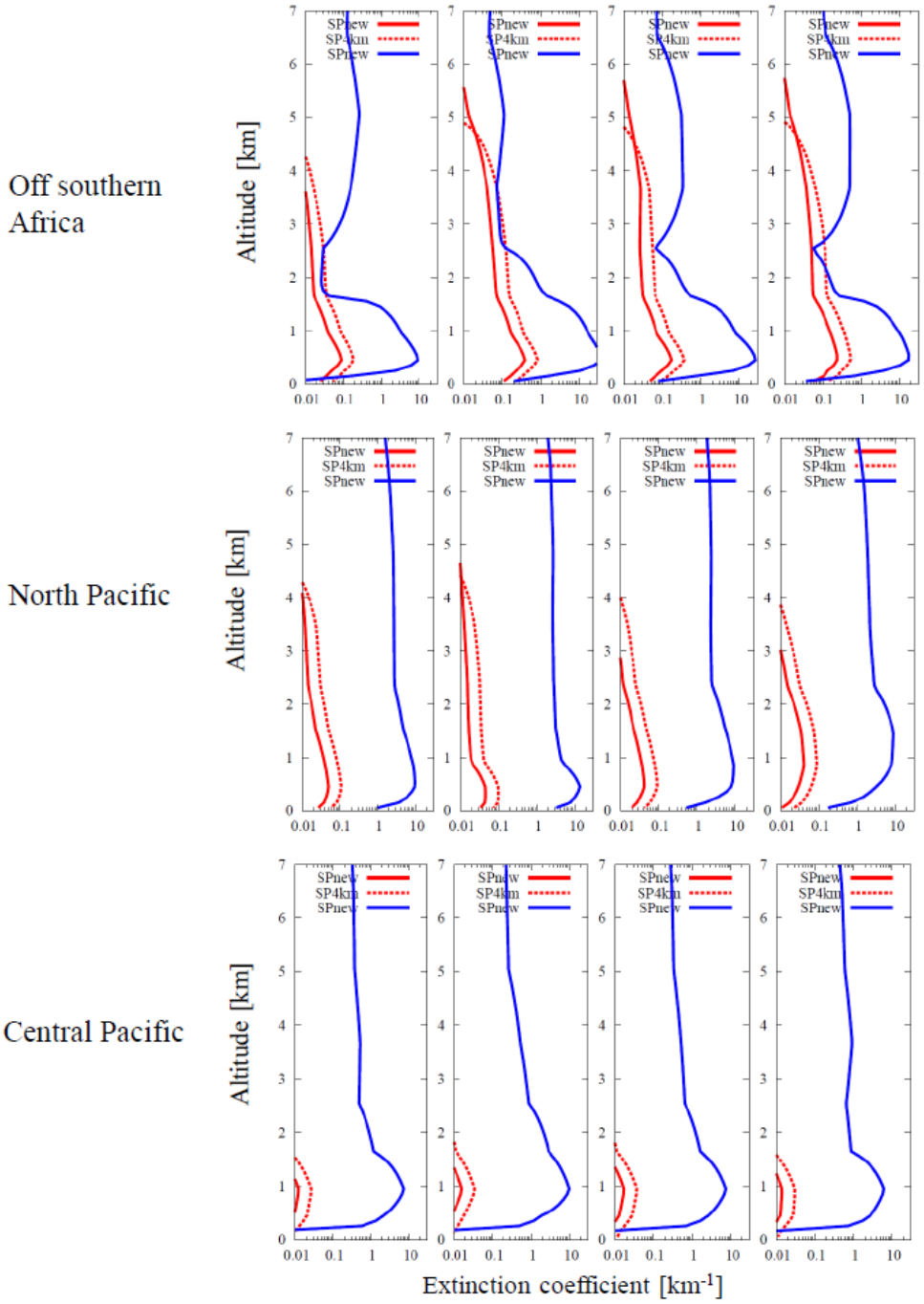

Fig. 4-8. The seasonal mean extinction profiles for aerosols and clouds of SPnew (solid line) and SP4km (dashed line) experiments in the cloudy-sky condition. These profiles are averaged in the three sections of Fig. 2-10 and in the seasons (boreal spring (left), summer (left-middle), autumn (right-middle), and winter (right)). The *x*-axis shows the logarithmic scale of the extinction coefficient [km^{-1}] and the *y*-axis shows the altitude [km].

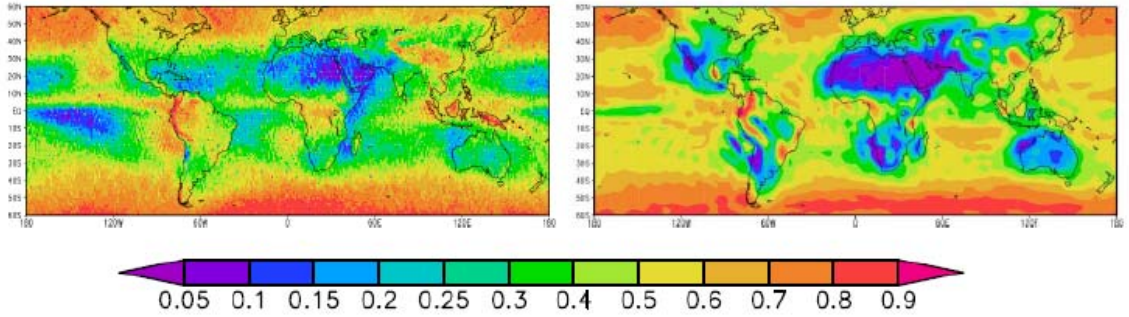

Fig. 4-9. Annual mean distributions of sum of the occurrence probabilities of above-cloud and cloudy-undetected cases in CALIPSO V3 product (left) and cloud fraction of clouds with COT of larger than 3 in SPnew model (right).

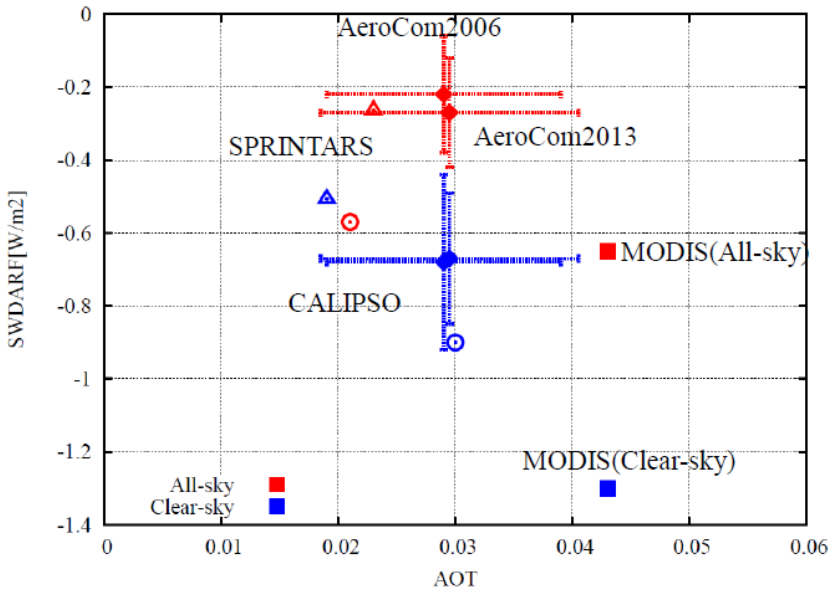

Fig. 4-10. Scatter plot between anthropogenic DARF and anthropogenic AOT under clear-sky (blue) and all-sky (red) conditions for CALIPSO V3 product (○), SPnew model(△), and AeroCom studies (●). The averages of SWDARF and AOT between 60°S and 60°N for CALIPSO V3 product and SPnew model, the global averages of SWDARF and AOT (550 nm) in reference to *Schulz et al.* [2006] (AeroCom2006) and *Bellouin et al.*, [2008] (MODIS), and the global averages of total (shortwave+ longwave) DARF and AOT(550 nm) in reference to *Myhre et al.* [2013] (AeroCom2013). The error bars show the standard deviations of DARF and AOT for AeroCom models.

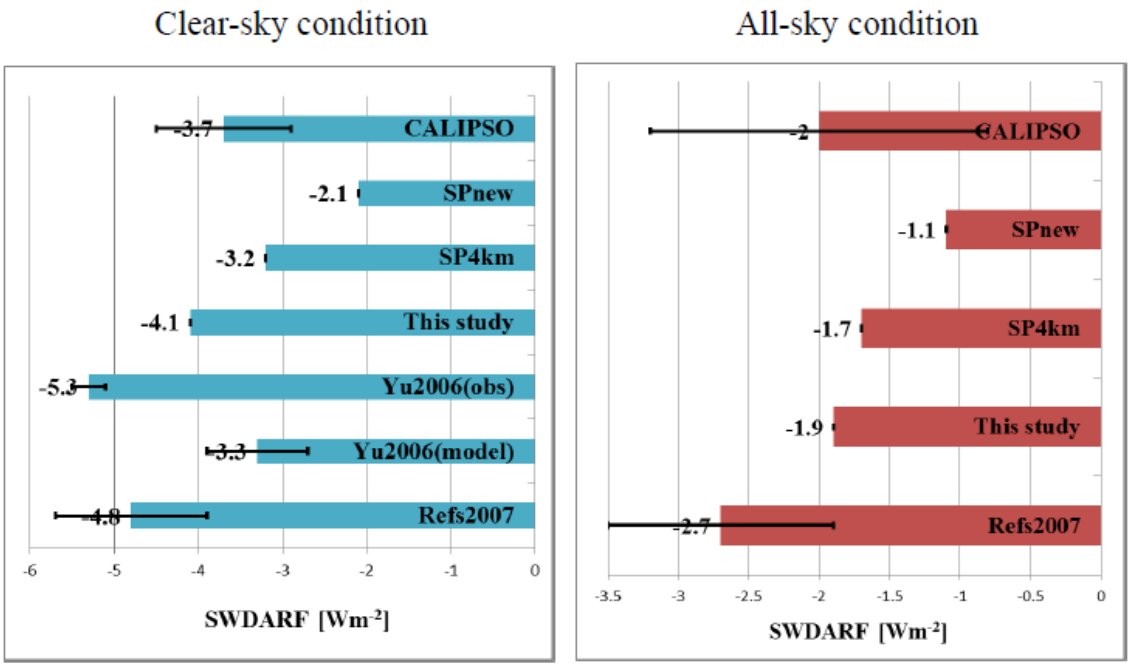

Fig. 4-11. Annual mean values of the clear-sky SWDARF (left) and all-sky SWDARF (right) for total aerosols. The averages of SWDARF between 60°S and 60°N for CALIPSO V3 product and SPnew and SP4km experiments. The best estimation of SWDARF in this study is estimated in section 4.5. Yu2006(obs) and Yu 2006(model) are the global mean values of the clear-sky SWDARF estimated by the multi-satellite observations and multi-models [*Yu et al*., 2006]. Refs2007 is referred to *Liu et al*. [2007], *Kim and Ramanathan* [2008], *Ma et al.* [2012], *Zhang et al.* [2012], and *Kinne et al.* [2013] and the error bars show the standard deviations of these studies.

5. Summary

In this study, shortwave direct aerosol radiative forcing (SWDARF) is estimated by using satellite observation data and climate modeling, and the uncertainties of estimated SWDARF are discussed.

The CALIPSO satellite with CALIOP lidar, for the first time, provides us with a global data of aerosol and cloud vertical profiles [*Winker et al*., 2009, 2013]. In addition, CALIOP has capability to detect aerosols existing above the optically thick clouds which are not observed by passive remote sensing and ground based lidar [*Winker et al*., 2010]. Several studies reported that absorbing aerosols above low-level clouds produce a large positive forcing over the Atlantic Ocean off southwest Africa [e.g. *Keil and Haywood*, 2003; *Chand et al*., 2009]. SWDARFs of aerosols above clouds have never been estimated in the global scale using observation data.

I investigate four scenarios for estimating the SWDARF at the top of the atmosphere (TOA) using data of CALIPSO lidar and data of MODIS sensor. The first scenario is a case that aerosols are observed in clear-sky condition (clear-sky case). The second scenario is a case of aerosols existing above clouds (above-cloud case). The third scenario is a case of aerosols existing below high-level clouds such as cirrus (below-cloud case). The fourth scenario is a case of aerosols undetected by CALIOP lidar exist below/within the optically thick clouds (cloudy-undetected case). The cloudy-sky SWDARF is calculated by SWDARFs of above-cloud, below-cloud, and cloudy-undetected cases weighted by the occurrence probability of each scenario. The all-sky SWDARF is then calculated by combination of clear-sky and cloudy-sky SWDARF weighted by the cloud occurrence probability. In this study, the global scale estimate of cloudy-sky SWDARF is performed for the first time by using observation data. My analysis of the CALIPSO Version 3 product shows the occurrence probabilities in clear-sky, above-cloud, below-cloud, and cloudy-undetected cases are 38%, 4%, 16%, and 42%, respectively. This indicates that CALIOP can observe 58% of aerosols in all-sky condition, whereas the aerosol observation by passive remote sensing is limited only in clear-sky condition, i.e. 38% of aerosols.

In clear-sky and below-cloud cases, aerosols mainly scatter sunlight and SWDARF shows negative values, except for bright surfaces. On the other hand, SWDARF globally shows positive value in above-cloud case. In this case, the absorption of aerosols is enhanced by the high reflectance of clouds and changes the SWDARF at TOA from negative to positive. As for the cloudy-undetected case, I assume the SWDARF to be zero, because optically thick clouds dominantly scatter the incident sunlight. The above mentioned method of analysis is applied to CALIPSO Version 2

and Version 3 products to obtain SWDARFs between 60°S and 60°N under clear-sky, cloudy-sky, and all-sky conditions as −3.7±0.8, −3.7±0.7, and −2.0±1.2 Wm^{-2}. The result indicates the difference of the version of the CALIPSO product is as large as 50% in all-sky forcing.

According to previous studies of the global aerosol model intercomparison project AeroCom, SWDARF simulated by MIROC-SPRINTARS is smaller negative than the mean value of other model estimates [*Yu et al.*, 2006; *Schulz et al.*, 2006; *Myhre et al.*, 2013]. In this study, SWDARF is also calculated by the latest version of MIROC [*Watanabe et al.*, 2010]. In the MIROC model, the optical properties of aerosols and clouds are separately calculated in SPRINTARS aerosol module and mstrnX radiation module. By detailed investigation of aerosol optical thickness (AOT) and and single scattering albedo (SSA) from the two modules, I found that the mstrnX AOT and SSA are smaller than those of SPRINTARS, because aerosol size indices of mstrnX is different from that of SPRINTARS in order to save CPU time. In order to make the two modules consistent with each other, I modified the interface between the two modules to set common optical aerosol models with 6 size bins of mineral dust, 4 types of carbonaceous aerosols, sulfate, and 4 size bins of sea salt. In this study, this new model is referred to as the SPnew model. I confirmed that AOT of each aerosol component and SSA of mstrnX agree with those of SPRINTARS within 4% in the SPnew model. Absorption of dust and carbonaceous aerosols becomes smaller from the standard model to the SPnew model. Zonal averages of SWDARF between 60°S and 60°N under clear-sky, cloudy-sky, and all-sky conditions change from −2.0, +0.3, and −0.7 Wm^{-2} in the standard model to −2.1, −0.1, and −1.1 Wm^{-2} in SPnew model.

The vertical profiles of aerosols are globally observed by CALIPSO lidar under clear-sky condition. High concentrated aerosols are globally observed by CALIPSO lower than 2 km altitude; in particular, aerosol extinction coefficient is larger than 0.05 at altitude lower than 1 km. On the other hand, the aerosol extinction coefficient in SPnew model is underestimated globally below 2 km altitude, while aerosols are elevated up to 7 km altitude around source regions of carbonaceous aerosols and dust in the model. These results indicate that aerosols are transported higher than the observation in a vertical direction, but are hardly transported in a horizontal direction in MIROC.

I compared the the obtained geographical distributions of AOT and SSA from satellites and models. The geographical distribution of CALIPSO AOT is found similar to that of MODIS observations, while CALIPSO AOT is smaller than MODIS AOT by 20%. Compared with CALIPSO and MODIS AOT, SPnew AOT is underestimated in

almost all regions. This causes smaller negative SWDARF under clear-sky condition in the model. It is also found that under clear-sky condition the aerosol extinction coefficient of SPnew is smaller below 4 km altitude and larger above 4 km altitude than that of CALIPSO. The ratio of CALIPSO AOT to SPnew AOT (CALIPSO AOT / SPnew AOT) is 2.14 below 4 km and 0.29 above 4 km altitude. In order to study the effect of this difference, I performed a model simulation that aerosol concentrations multiplied by 2.14 below 4 km altitude and 0.29 above 4 km altitude in the SPnew model. This simulation is referred to as the SP4km experiment.

Zonal averages of SWDARF between 60°S and 60°N under clear-sky, cloudy-sky, and all-sky conditions are calculated in the SP4km experiment as –3.2, -0.3, and –1.7 Wm^{-2}. The zonal average AOT between 60°S and 60°N for SP4km is comparable to CALIPSO AOT and the modeled SSA is overestimated, but the zonal average of clear-sky SWDARF for SP4km is smaller negative than CALIPSO by 0.5 Wm^{-2}. This difference is mainly caused by an underestimation of aerosol extinction coefficient below 2 km altitude over ocean in the Southern Hemisphere.

MIROC frequently simulate optically thicker clouds than observation. Off southwest Africa, absorbing aerosols emitted by biomass burning in Africa are transported above low-level clouds. Aerosols usually undetected below 1.5 km altitude by CALIPSO observations in above-cloud case, whereas aerosols are simulated from surface to 5 km altitude in the model. In cloudy-sky condition, the modeled SWDARF is more positive than the observation, because the absorption of aerosols within/above clouds is largely enhanced by higher cloud reflectance derived from optically thick clouds. Over central and northern Pacific, optically thick clouds are simulated from the lower to upper troposphere in the model, so that clouds mainly scatter sunlight and aerosols cause less negative forcing than the CALIPSO case. From these results, the cloudy-sky SWDARF in MIROC is considered to be smaller negative than that of CALIPSO.

Summarizing the results in this study, I like to propose the best estimates of clear-sky and all-sky SWDARF of –4.1 and –1.9 Wm^{-2}. On the other hand, the global averages of SWDARF from the past studies are -4.8 ± 0.8 and -2.7 ± 0.9 Wm^{-2} under clear-sky and all-sky conditions [*Liu et al*., 2007; *Kim and Ramanathan,* 2008; *Ma et al.,* 2012; *Zhang et al.,* 2012; *Kinne et al.,* 2013]. My estimate of the clear-sky SWDARF is located in between the CALIPSO values obtained in this study and the average of previous studies. This conclusion suggests that both the satellite-borne lidar and modeling methods have their own characteristic errors in SWDARF estimation. The present analysis is considered to be useful to identify causes for errors found in this study.

Appendix A

In this study, four scenarios for radiative transfer calculation in CALIPSO observations, *i.e.* clear-sky, above-cloud, below-cloud, and cloudy-undetected cases, are investigated. The conditional occurrence probability of aerosols observed in the clear-sky condition is given as

$$P_a = \frac{N_a}{N_{\text{clear-sky}}}, \tag{A-1}$$

where N_a is the pixel count where aerosols are observed in clear-sky condition and $N_{\text{clear-sky}}$ is the pixel count in clear-sky condition. We use the conditional AOT at wavelength of 532 nm for radiative transfer calculations defined as

$$\tau_a = \frac{\tau_{a,sum}}{N_a}, \tag{A-2}$$

where $\tau_{a,sum}$ is the sum of AOT observed at clear-sky pixels. The clear-sky AOT shown in Fig. 2-8 is given as

$$\tau_{\text{clear-sky}} = \frac{\tau_{a,sum}}{N_{\text{clear-sky}}} = P_a \frac{\tau_{a,sum}}{N_{\text{a}}}. \tag{A-3}$$

Shortwave direct aerosol radiative forcing (SWDARF) in clear-sky case is defined as

$$SWDARF_{\text{clear-sky}} = P_a \times SWDARF_a, \tag{A-4}$$

where $SWDARF_a$ is the SWDARF calculated by using τ_a.

In a similar way, P_{ac}, P_{bc}, and P_{uc} are the conditional occurrence probabilities of above-cloud, below-cloud, and cloudy-undetected cases, respectively:

$$P_{ac} = \frac{N_{ac}}{N_{\text{cloudy-sky}}}, \quad P_{bc} = \frac{N_{bc}}{N_{\text{cloudy-sky}}}, \quad \text{and} \quad P_{uc} = \frac{N_{\text{cloudy-sky}} - N_{ac} - N_{bc}}{N_{\text{cloudy-sky}}}, \tag{A-5}$$

$$P_{ac} + P_{bc} + P_{uc} = 1, \tag{A-6}$$

where N_{ac}, N_{bc}, and $N_{\text{cloudy-sky}}$ are the pixel counts of above-cloud, below-cloud and cloudy-sky cases, respectively. τ_{ac} and τ_{bc} are AOTs for radiation calculations in above-cloud and below-cloud cases, respectively:

$$\tau_{ac} = \frac{\tau_{ac,sum}}{N_{ac}} \quad \text{and} \quad \tau_{bc} = \frac{\tau_{bc,sum}}{N_{bc}} \tag{A-7}$$

where $\tau_{ac,sum}$ and $\tau_{bc,sum}$ are the sums of AOT observed in above-cloud and below-cloud cases, respectively. The cloudy-sky AOT is given as

$$\tau_{\text{cloudy-sky}} = \frac{\sum_{i=ac,bc,uc} \tau_{i,sum}}{N_{cloudysky}} = \sum_{i=ac,bc} P_i \cdot \tau_i + 0 = \sum_{i=ac,bc} P_i \cdot \tau_i. \tag{A-8}$$

The SWDARF in cloudy-sky condition is then given as

$$SWDARF_{\text{cloudy-sky}} = \sum_{i=ac,bc,uc} P_i \times SWDARF_i \approx \sum_{i=ac,bc} P_i \times SWDARF_i + 0 = \sum_{i=ac,bc} P_i \times SWDARF_i \,. \quad \text{(A-9)}$$

where SWDARF of the cloudy-undetected case is assumed to be close to zero, because optically thick clouds dominantly scatter the incident sunlight.

The AOT and SWDARF under all-sky condition are given as

$$\tau_{\text{all-sky}} = P_{\text{clear-sky}} \cdot \tau_{\text{clear-sky}} + P_{\text{cloudy-sky}} \cdot \tau_{\text{cloudy-sky}}\,, \quad \text{(A-10)}$$

$$SWDARF_{\text{all-sky}} = P_{\text{clear-sky}} \times SWDARF_{\text{clear-sky}} + P_{\text{cloudy-sky}} \times SWDARF_{\text{cloudy-sky}}\,, \quad \text{(A-11)}$$

where $P_{\text{cloudy-sky}}$ is equivalent to column cloud cover fraction, C.

Appendix B

The aerosol size distribution is usually expressed by the log-normal distribution and the number size distribution is expressed by

$$\frac{dN}{d\ln r} = \frac{C_n}{\sqrt{2\pi}\ln(\sigma_g)} \exp\left(-\tfrac{1}{2}\left(\frac{\ln(r/r_n)}{\ln(\sigma_g)}\right)^2\right), \quad \text{(B-1)}$$

where $dN/d\ln(r)$ is number of aerosol particles with radius in the infinitesimal size range $r \pm d\ln(r)$, r_n is number mean radius, C_n is total aerosol columnar particle number, and σ_g is geometric standard deviation (GSD) of the size distribution. The volume size distribution is

$$\frac{dV}{d\ln r} = \frac{C_v}{\sqrt{2\pi}\ln(\sigma_g)} \exp\left(-\tfrac{1}{2}\left(\frac{\ln(r/r_v)}{\ln(\sigma_g)}\right)^2\right), \quad \text{(B-2)}$$

where r_v is volume mean radius and C_v is total aerosol columnar particle volume. The relationship between r_v and r_n is expressed by

$$r_v = r_n \exp\left(3 \cdot \ln^2\left(\sigma_g\right)\right), \quad \text{(B-3)}$$

and the relationship between C_v and C_n is expressed by

$$C_v = \frac{4\pi}{3} r_n^3 \exp\left(4.5 \cdot \ln^2\left(\sigma_g\right)\right) C_n\,. \quad \text{(B-4)}$$

From equation B-4, the average mass of one aerosol particle m_p is given by

$$m_p = \frac{C_v}{C_n} \times m_a = \frac{4\pi}{3} r_n^3 \exp\left(4.5 \cdot \left(\ln\left(\sigma_g\right)\right)^2\right) m_a\,, \quad \text{(B-5)}$$

where m_a is mass per unit volume. Total aerosol columnar particle number N is given by

$$N = \frac{M_a}{m_p}, \tag{B-6}$$

where M_a is total aerosol columnar particle mass.

SPRINTARS treats 6 size bins of dust particle and 4 size bins of sea salt [*Takemura et al.*, 2009]. In SPnew model, aerosol volume size distribution in each size bin is defined by the log-normal distribution. Figures B-1 and B-2 show the log-normal distributions of dust and sea salt at each sizes based on Table 3-2. From these figures, GSDs of volume size distributions for dust and sea salt are set to 1.1 and 1.2 in SPnew model.

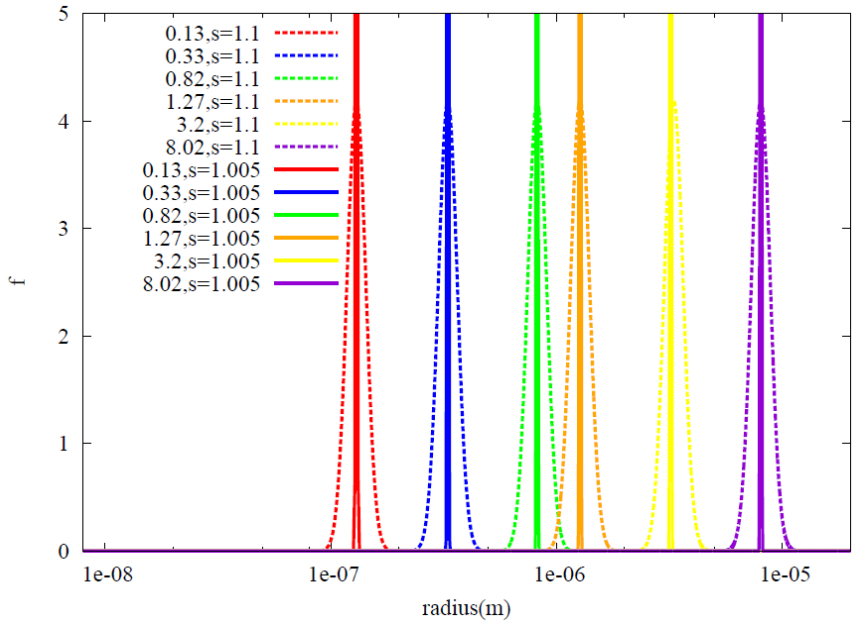

Fig. B-1. The log-normal distributions of 6 different size dust particles in the cases of GSD = 1.005 and GSD = 1.1.

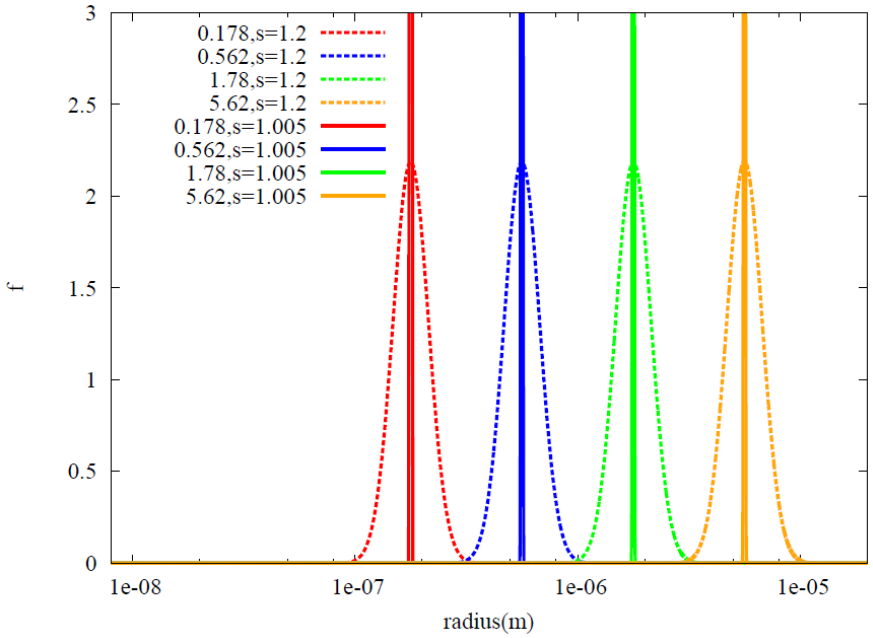

Fig. B-2. The log-normal distributions of 4 different size sea salt particles in the cases of GSD = 1.005 and GSD = 1.2.

Appendix C

I use AERONET Level 1.5 Product [*Holben et al.*, 1998; *Dubovik et al*., 2006] for the comparison of CALIPSO observation and MIROC model. AERONET Level 2 Product is the quality-assured products. The number of data in level 2 product is only 10% of that in level 1.5 product, so that AERONET level 1.5 product is used in this study. AERONET level 1.5 product includes a certain amount of data which has too large absorbing property ($\omega(\lambda) < 0.6$); therefore, a data selection procedure is performed to remove the low-quality data. I select the data which has $1.33 < m_r(\lambda) < 1.6$, $m_i(\lambda) < 0.1$, and $\omega(\lambda) < 0.987$, where m_r and m_i are the real part and imaginary part of refractive index, ω is SSA, and λ = 440, 675, 870, and 1020 nm. In addition, I eliminate the data which has both $\tau(\lambda) < 0.05$ and $FMF(\lambda) < 0.985$, where τ is AOT and *FMF* is fine mode fraction of AOT. After these data selections, SSA at 550 nm is interpolated using SSA at 440 and 675 nm. The calculated SSA at 550 nm is used for the comparison of CALIPSO observation and MIROC model (see section 4.3).

Acknowledgements

I am deeply grateful to Prof. Teruyuki Nakajima at Atmosphere and Ocean Research Institute (AORI), the University of Tokyo, for giving the notable subject of research and insightful comments during many years of the doctoral course for my study.

I am indebted to Asst. Prof. Miho Sekiguchi at Tokyo University of Marine Science and Technology for technical comments about the radiation models of Rstar, Fstar, and mstrnX. I would like to thank Dr. D. Goto at National Institute for Environmental Studies (NIES) for helping my research about the MIROC-AGCM simulation. I appreciate Dr. Nishizawa at NIES for his kind advice about the lidar observations. I have a lot to be thankful to Dr. Nick Schutgens, Dr. Toshiro Inoue, Dr. Haruo Tsuruta, and Dr. Junya Uchida for discussions and comments about my study.

I would also like to express my gratitude to my family for their moral support and warm encouragements.

The model simulations were performed by using the supercomputer system (NEC SX-9A/ECO) of the NIES.

References

Ackerman, A. S., O. B. Toon, D. E. Stevens, A. J. Heymsfield, V. Ramanathan, and E. J. Welton (2000), Reduction of tropical cloudiness by soot, *Science*, *288*, 1042-1047, doi:10.1126/science.288.5468.1042.

Albrecht, B. A. (1989), Aerosols, cloud microphysics, and fractional cloudiness, *Science*, *245*, 1227–1230.

d'Almeida, G. A., P. Koepke, and E. P. Shettle (1991), *Atmospheric Aerosols: Global Climatology and Radiative Characteristics*, A. Deepak Publishing, Hampton, VA.

Bellouin, N., A. Jones, J. Haywood, and S. A. Christopher (2008), Updated estimate of aerosol direct radiative forcing from satellite observations and comparison against the Hadley Centre climate model, *J. Geophys. Res.*, *113*, D10205, doi:10.1029/2007JD009385.

Bougamont, M., J. L. Bamber, and W. Greuell (2005), A surface mass balance model for the Greenland Ice Sheet, *J. Geophys. Res*., *110*, F04018, doi:10.1029/2005JF000348.

Chand, D., T. L. Anderson, R. Wood, R. J. Charlson, Y. Hu, Z. Liu, and M. Vaughan (2008), Quantifying above-cloud aerosol using spaceborne lidar for improved understanding of cloudy-sky direct climate forcing, *J. Geophys. Res.*, *113*, D13206, doi:10.1029/2007JD009433.

Chand, D., R. Wood, T. L. Anderson, S. K. Satheesh, and R. J. Charlson (2009), Satellite-derived direct radiative effect of aerosols dependent on cloud cover, *Nature Geoscience*, *2*, 181-184, doi:10.1038/NGE0437.

Chu, D. A., Y. J. Kaufman, C. Ichoku, L. A. Remer, D. Tanré, and B. N. Holben (2002), Validation of MODIS aerosol optical depth retrieval over land, *Geophys. Res. Lett.*, *29(12)*, doi:10.1029/2001GL013205.

Coddington, O. M., P. Pilewskie, J. Redemann, S. Platnick, P. B. Russell, K. S. Schmidt, W. J. Gore, J. Livingston, G. Wind, and T. Vukicevic (2010), Examining the impact of overlying aerosols on the retrieval of cloud optical properties from passive remote sensing, *J. Geophys. Res.*, *115*, D10211, doi:10.1029/2009JD012829.

De Graaf, M., L. G. Tilstra, P. Wang, and P. Stammes (2012), Retrieval of the aerosol direct radiative effect over clouds from spaceborne spectrometry, *J. Geophys. Res.*, *117*, D07207, doi:10.1029/2011JD017160.

Deepak, A. and H. G. Gerber (Eds.) (1983), Report of the experts meeting on aerosols and their climatic effects, World Meteorological Organization, Geneva, Switzerland, *Rep. WCP-55*, 107 pp.

Dubovik, O., B. Holben, T. F. Eck, A. Smirnov, Y. J. Kaufman, M. D. King, D. Tanré,

and I. Slutsker (2002), Variability of absorption and optical properties of key aerosol types observed in worldwide locations. *J. Atmos. Sci.*, *59*, 590-608.

Dubovik, O., A. Sinyuk, T. Lapyonok, B. N. Holben, M. Mishchenko, P. Yang, T. F. Eck, H. Volten, O. Muñoz, B. Veihelmann, W. J. van der Zande, J.-F. Leon, M. Sorokin, and I. Slutsker (2006), Application of spheroid models to account for aerosol particle nonsphericity in remote sensing of desert dust, *J. Geophys. Res*., *111*, D11208, doi:10.1029/2005JD006619.

Fraser, R. S., and Y. J. Kaufman (1985), The relative importance of aerosol scattering and absorption in remote sensing, *IEEE Trans. Geosci. Remote Sens. GE-23*, 625-633.

Hansen, J., M. Sato, and R. Ruedy (1997), Radiative forcing and climate response, *J. Geophys. Res.*, *102*, 6831–6864, doi:10.1029/96JD03436.

Haywood, J. M., and K. P. Shine (1997), Multi-spectral calculations of the radiative forcing of tropospheric sulphate and soot aerosols using a column model, *Quart. J. Roy. Meteor. Soc.*, *123*, 1907-1930.

Haywood, J. M., S. R. Osborne, and S. J. Abel (2004), The effect of overlying absorbing aerosol layers on remote sensing retrievals of cloud effective radius and cloud optical depth, *Q. J. R. Meteorol. Soc.*, *130*, 779-800.

Hobbs, P. V., J. S. Reid, R. A. Kotchenruther, R. J. Ferek, and R. Weiss (1997), Direct radiative forcing by smoke from biomass burning, *Science*, *275*, 1776–1778.

Holben, B. N., T. F. Eck, I. Slutsker, D. Tanre´, J. P. Buis, A. Setzer, E. Vermote, J. A. Reagan, Y. J. Kaufman, T. Nakajima, F. Lavenu, I. Jankowiak, and A. Smirnov (1998), AERONET—A federated instrument network and data archive for aerosol characterization, *Remote Sens. Environ*., *66*, 1– 16.

Hu, Y., M. Vaughan, Z. Liu, K. Powell, and S. Rodier (2007), Retrieving optical depths and lidar ratios for transparent layers above opaque water clouds from CALIPSO lidar measurements, *IEEE Trans. Geosci. Remote Sens. Lett.*, *4*, 523–526.

Hu, Y., D. Winker, M. Vaughan, B. Lin, A. Omar, C. Trepte, D. Flittner, P. Yang, S. L. Nasiri, B. Baum, R. Holz, W. Sun, Z. Liu, Z. Wang, S. Young, K. Stamnes, J. Huang, and R. Kuehn (2009), CALIPSO/CALIOP cloud phase discrimination algorithm, *J. Atmos. Oceanic Technol*., *26*, 2293–2309, http://dx.doi.org/10.1175/2009JTECHA1280.1.

Hubanks, P., M. D. King, S. Platnick, and R. Pincus (2008), *MODIS Atmosphere L3 Gridded Product Algorithm Theoretical Basis Document*, ATBD Reference Number: ATBD-MOD-30.

Ichoku, C., D. A. Chu, S. Mattoo, Y. J. Kaufman, L. A. Remer, D. Tanre´, I. Slutsker,

and B. N. Holben (2002), A spatio-temporal approach for global validation and analysis of MODIS aerosol products, *Geophys. Res. Lett*., *29(12)*, doi:10.1029/2001GL013206.

Intergovernmental Panel of Climate Change (IPCC) (2013), *Climate Change 2013: The Physical Science Basis. Contribution of Working Group I to the Fifth Assessment Report of the Intergovernmental Panel on Climate Change*, edited by: Stocker, T. F., Qin, D., Plattner, G.-K., Tignor, M., Allen, S. K., Boschung, J., Nauels, A., Xia, Y., Bex, V., and Midgley, P. M., 1535pp., Cambridge University Press, Cambridge, United Kingdom and New York, doi:10.1017/CBO9781107415324.

Kalnay, E., M. Kanamitsu, R. Kistler, W. Collins, D. Deaven, L. Gandin, M. Iredell, S. Saha, G. White, J. Woollsen, Y. Zhu, M. Chelliah, W. Ebisuzaki, W. Higgins, J. Janowiak, K. C. Mo, C. Ropelewski, J. Wang, A. Leetmaa, R. Reynolds, R. Jenne, and D. Joseph (1996), The NCEP/NCAR 40-year reanalysis project, *Bull. Amer. Meteor. Soc.*, *77*, 437-471.

Kaufman, Y.J., D. Tanre, O. Dubovik, A. Karnieli, and L.A. Remer (2001), Absorption of sunlight by dust as inferred from satellite and ground-based remote sensing, *Geophys. Res. Lett.*, *28*, 1479-1482.

Kaufman, Y. J., L. A. Remer, D. Tanr´e, R.-R. Li, R. Kleidman, S. Mattoo, R. Levy, T. Eck, B. N. Holben, C. Ichoku, J. Martins, and I. Koren (2005), A critical examination of the residual cloud contamination and diurnal sampling effects on MODIS estimates of aerosol over ocean, *IEEE Trans. on Geoscience & Remote Sensing*, *43(12)*, 2886–2897.

Keil, A., and J. M. Haywood (2003), Solar radiative forcing by biomass burning aerosol particles during SAFARI 2000: A case study based on measured aerosol and cloud properties, *J. Geophys. Res.*, *108*, 8467, doi:10.1029/2002JD002315.

Kim, D. and V. Ramanathan (2008), Solar radiation budget and radiative forcing due to aerosols and clouds, *J. Geophys. Res.*, *113*, D02203, doi:10.1029/2007JD008434.

Kinne, S., M. Schulz, C. Textor, S. Guibert, Y. Balkanski, S. E. Bauer, T. Berntsen, T. F. Berglen, O. Boucher, M. Chin, W. Collins, F. Dentener, T. Diehl, R. Easter, J., Feichter, D. Fillmore, S. Ghan, P. Ginoux, S. Gong, A. Grini, J. Hendricks, M. Herzog, L. Horowitz, I. Isaksen, T., Iversen, A. Kirkevåg, S. Kloster, D. Koch, J. E. Kristjansson, M. Krol, A. Lauer, J. F. Lamarque, G. Lesins, X. Liu, U. Lohmann, V. Montanaro, G. Myhre, J. Penner, G. Pitari, S. Reddy, O. Seland, P. Stier, T. Takemura, and X. Tie (2006), An AeroCom initial assessment – optical properties in aerosol component modules of global models, *Atmos. Chem. Phys.*, *6*, 1815-1834, doi:10.5194/acp-6-1815-2006.

Kinne, S., D. O'Donnel, P. Stier, S. Kloster, K. Zhang, H. Schmidt, S. Rast, M. Giorgetta, T. F. Eck, and B. Stevens (2013), MAC-v1: A new global aerosol climatology for climate studies, *J. Adv. Model. Earth Syst*., *5*, 704–740, doi:10.1002/jame.20035.

Kittaka, C., D. M. Winker, M. A. Vaughan, A. Omar, and L. A. Remer (2011), Intercomparison of column aerosol optical depths from CALIPSO and MODIS-Aqua, *Atmos. Meas. Tech.*, *4*, 131-141, doi:10.5194/amt-4-131-2011.

Kneizys P. X., E. P. Shettle, L. W. Abreu, J. H. Chetwynd, G. P. Anderson, W. O. Gallery, J. E. A. Selby, and S. A. Clough (1988), Users Guide to LOWTRAN 7, *Rep. AFGL-TR-88-0177, Bedford, MA: Air Force Geophys. Lab.*.

Levy, R. C., L. A. Remer, S. Mattoo, E. F. Vermote, and Y. J. Kaufman (2007), Second-generation operational algorithm: Retrieval of aerosol properties over land from inversion of Moderate Resolution Imaging Spectroradiometer spectral reflectance, *J. Geophys. Res.*, *112*, D13211, doi:10.1029/2006JD007811.

Levy, R. C., L. A. Remer, R. G. Kleidman, S. Mattoo, C. Ichoku, R. Kahn, and T. F. Eck (2010), Global evaluation of the Collection 5 MODIS dark-target aerosol products over land, *Atmos. Chem. Phys.*, *10*, 10399–10420, doi:10.5194/acp-10-10399-2010.

Li, Y., R. Yu, Y. Xu, and X. Zhang (2004), Spatial distribution and seasonal variation of cloud over China based on ISCCP data and surface observations, *J. Meteor. Soc. Japan, 82*, 761–773.

Liu, X., J. E. Penner, B. Das, D. Bergmann, J. M. Rodriguez, S. Strahan, M. Wang, and Y. Feng (2007), Uncertainties in global aerosol simulations: Assessment using three meteorological data sets, *J. Geophys. Res.*, *112*, D11212, doi:10.1029/2006JD008216.

Liu, Z., M. A. Vaughan, D. M. Winker, C. Kittaka, B. J. Getzewich, R. E. Kuehn, A. Omar, K. Powell, C. R. Trepte, and C. A. Hostetler (2009), The CALIPSO lidar cloud and aerosol discrimination: Version 2 algorithm and initial assessment of performance. *J. Atmos. Oceanic Technol., 26***,** 1198–1213.

Liu, Z., R. Kuehn, M. Vaughan, D. Winker, A. Omar, K. Powell, C. Trepte, Y. Hu, and C. Hostetler (2010), The CALIPSO cloud and aerosol discrimination: Version 3 algorithm and test results, *25th International Laser Radar Conference (ILRC)*, St. Petersburg, Russia, ISBN 978-5-94458-109-9.

Ma, X., F. Yu, and G. Luo (2012), Aerosol direct radiative forcing based on GEOS-Chem-APM and uncertainties, *Atmos. Chem. Phys*., *12*, 5563-5581, doi:10.5194/acp-12-5563-2012.

Meyer, K., S. Platnick, L. Oreopoulos, and D. Lee (2013), Estimating the direct

radiative effect of absorbing aerosols overlying marine boundary layer clouds in the southeast Atlantic using MODIS and CALIOP, *J. Geophys. Res. Atmos*., *118*, 4801–4815, doi:10.1002/jgrd.50449.

Myhre, G. (2009), Consistency between satellite-derived and modeled estimates of the direct aerosol effect, *Science*, *325*, 187–190.

Myhre, G., B. H. Samset, M. Schulz, Y. Balkanski, S. Bauer, T. K. Berntsen, H. Bian, N. Bellouin, M. Chin, T. Diehl, R. C. Easter, J. Feichter, S. J. Ghan, D. Hauglustaine, T. Iversen, S. Kinne, A. Kirkevåg, J.-F. Lamarque, G. Lin, X. Liu, M. T. Lund, G. Luo, X. Ma, T. van Noije, J. E. Penner, P. J. Rasch, A. Ruiz, Ø. Seland, R. B. Skeie, P. Stier, T. Takemura, K. Tsigaridis, P. Wang, Z. Wang, L. Xu, H. Yu, F. Yu, J.-H. Yoon, K. Zhang, H. Zhang, and C. Zhou (2013), Radiative forcing of the direct aerosol effect from AeroCom Phase II simulations, *Atmos. Chem. Phys*., *13*, 1853-1877, doi:10.5194/acp-13-1853-2013.

Nakajima, T. and M. Tanaka (1983), Effect of wind-generated waves on the transfer of solar radiation in the atmosphere-ocean system, *J. Quant. Spectrosc. Radiat. Transfer*, *29*, 521–537.

Nakajima, T. and M. Tanaka (1986), Matrix formulations for the transfer of solar radiation in a plane-parallel scattering atmosphere, *J. Quant. Spectrosc. Radiat. Transfer*, *35*, 13–21.

Nakajima, T., and M. Tanaka (1988), Algorithms for radiative intensity calculations in moderately thick atmospheres using a truncation approximation, *J. Quant. Spectrosc. Radiat. Transfer*, *40*, 51-69.

Nakajima, T., G. Tonna, R. Rao, Y. Kaufman, and B. Holben (1996), Use of sky brightness measurements from ground for remote sensing of particulate polydispersions. *App. Opt., 35*, 2672-2686.

Nakajima, T., S.-C. Yoon, V. Ramanathan, G.-Y. Shi, T. Takemura, A. Higurashi, T. Takamura, K. Aoki, B.-J. Sohn, S.-W. Kim, H. Tsuruta, N. Sugimoto, A. Shimizu, H. Tanimoto, Y. Sawa, N.-H. Lin, C.-T. Lee, D. Goto, and N. Schutgens (2007), Overview of the Atmospheric Brown Cloud East Asian Regional Experiment 2005 and a study of the aerosol direct radiative forcing in east Asia, *J. Geophys. Res.*, *112*, D24S91, doi:10.1029/2007JD009009.

Omar, A. H., D. M. Winker, C. Kittaka, M. A. Vaughan, Z. Liu, Y. Hu, C. R. Trepte, R. R. Rogers, R. A. Ferrare, K.-P. Lee, R. E. Kuehn, and C. A. Hostetler (2009), The CALIPSO automated aerosol classification and lidar ratio selection algorithm, *J. Atmos. Oceanic Technol.*, *26*, 1994–2014.

Omar, A. H., D. M. Winker, J. L. Tackett, D. M. Giles, J. Kar, Z. Liu, M. A.

Vaughan, K. A. Powell, and C. R. Trepte (2013), CALIOP and AERONET aerosol optical depth comparisons: One size fits none, *J. Geophys. Res. Atmos.*, *118*, 4748–4766, doi:10.1002/jgrd.50330.

Platnick, S., M. D. King, S. A. Ackerman, W. P. Menzel, B. A. Baum, J. C. Riedi, and R. A. Frey (2003), The MODIS cloud products: Algorithms and examples from Terra, *IEEE Trans. Geosci. Remote Sens.*, *41*, 459–473.

Powell, K. A., M. A. Vaughan, R. R. Rogers, R. E. Kuehn, W. H. Hunt, K.-P. Lee, and T. D. Murray (2010), The CALIOP 532- nm channel daytime calibration: Version 3 algorithm, *Proceedings of the 25th International Laser Radar Conference*, 1367–1370, ISBN 978-5-94458-109-9.

Rayner, N. A., D. E. Parker, E. B. Horton, C. K. Folland, L. V. Alexander, D. P. Rowell, E. C. Kent, and A. Kaplan (2003), Global analyses of sea surface temperature, sea ice, and night marine air temperature since the late nineteenth century, *J. Geophys. Res.*, *108*, 4407, doi:10.1029/2002JD002670, D14.

Redemann, J., M. A. Vaughan, Q. Zhang, Y. Shinozuka, P. B. Russell, J. M. Livingston, M. Kacenelenbogen, and L. A. Remer (2012), The comparison of MODIS-Aqua (C5) and CALIOP (V2 &V3) aerosol optical depth, *Atmos. Chem. Phys.*, *12*, 3025–3043, doi:10.5194/acp-12-3025-2012.

Remer, L. A., D. Tanré, Y. J. Kaufmann, C. Ichoku, S. Mattoo, R. Levy, D. A. Chu, B. Holben, O. Dubovik, A. Smirnov, J. V. Martins, R.-R. Li, and Z. Ahmad (2002), Validation of MODIS aerosol retrieval over ocean, *Geophys. Res. Lett.*, *29(12)*, doi:10.1029/2001GL013204.

Remer, L. A., Y. J. Kaufman, D. Tanré, S. Mattoo, D. A. Chu, J. V. Martins, R.-R. Li, C. Ichoku, R. C. Levy, R. G. Kleidman, T. F. Eck, E. Vermote, and B. N. Holben (2005), The MODIS aerosol algorithm, products, and validation, *J. Atmos. Sci.*, *62*, 947–973. doi: http://dx.doi.org/10.1175/JAS3385.1.

Remer, L. A., R. G. Kleidman, R. C. Levy, Y. J. Kaufman, D. Tanré, S. Mattoo, J. V. Martins, C. Ichoku, I. Koren, H. Yu and B. N. Holben (2008), Global aerosol climatology from the MODIS satellite sensors, *J. Geophys. Res.*, *113*, D14S07, doi:10.1029/2007JD009661.

Rienecker, M. M., M. J. Suarez, R. Gelaro, R. Todling, J. Bacmeister, E. Liu, M. G. Bosilovich, S. D. Schubert, L. Takacs, G.-K. Kim, S. Bloom, J. Chen, D. Collins, A. Conaty, A. da Silva, W. Gu, J. Joiner, R. D. Koster, R. Lucchesi, A. Molod, T. Owens, S. Pawson, P. Pegion, C. R. Redder, R. Reichle, F. R. Robertson, A. G. Ruddick, M. Sienkiewicz, and J. Woollen (2011), MERRA: NASA's Modern-Era Retrospective Analysis for Research and Applications, *J. Climate*, *24*, 3624–3648.

doi: http://dx.doi.org/10.1175/JCLI-D-11-00015.1.

Roesch, A., C. Schaaf, and F. Gao (2004), Use of Moderate-Resolution Imaging Spectroradiometer bidirectional reflectance distribution function products to enhance simulated surface albedos, *J. Geophys. Res.*, *109*, D12105, doi:10.1029/2004JD004552.

Román, M. O., C. B. Schaaf, P. Lewis, F. Gao, G. P. Anderson, J. L. Privette, A. H. Strahler, C. E. Woodcock, M. Barnsley (2010), Assessing the coupling between surface albedo derived from MODIS and the fraction of diffuse skylight over spatially-characterized landscapes, *Remote Sensing of Environment*, *114*, 738-760.

Rothman, L.S., D. Jacquemart, A. Barbe, D.C. Benner, M. Birk, L.R. Brown, M.R. Carleer, C. Chackerian, K. Chance, L.H. Coudert, V. Dana, V.M. Devi, J.M. Flaud, R.R. Gamache, A. Goldman, J.M. Hartmann, K.W. Jucks, A.G. Maki, J.Y. Mandin, S.T. Massie, J. Orphal, A. Perrin, C.P. Rinsland, M.A. Smith, J. Tennyson, R.N. Tolchenov, R.A. Toth, J. Vander Auwera, P. Varanasi, and G. Wagner (2005), The HITRAN 2004 molecular spectroscopic database, *J. Quant. Spectrosc. Radiat. Transfer*, *96*, 139–204. DOI: 10.1016/j.jqsrt.2004.10.008.

Ruggaber, A., R. Dlugi, and T. Nakajima (1994), Modelling of radiation quantities and photolysis frequencies in the troposphere, *J. Atmos. Chem.*, *18*, 171-210.

Satheesh, S. K., S. Deepshikha and J. Srinivasan (2006), Impact of dust aerosol on Earth-atmosphere clear-sky albedo and its short wave radiative forcing over Africa and Arabian regions. *Int. J. Remote Sens.*, *27*, 1691-1706.

Schaaf, C. B., F. Gao, A. H. Strahler, W. Lucht, X. Li, T. Tsang, N. C. Strugnell, X. Zhang, Y. Jin, J.-P. Muller, P. Lewis, M. Barnsley, P. Hobson, M. Disney, G. Roberts, M. Dunderdale, C. Doll, R. P. d'Entremont, B. Hu, S. Liang, J. L. Privette, and D. Roy (2002), First operational BRDF, albedo nadir reflectance products from MODIS, *Remote Sens. Environ.*, *83*, 135–148.

Schulz, M., C. Textor, S. Kinne, Y. Balkanski, S. E. Bauer, T. Berntsen, T. Berglen, O. Boucher, F. Dentener, A. Grini, S. Guibert, T. Iversen, D. Koch, A. Kirkev°ag, X. Liu, V. Montanaro, G. Myhre, J. Penner, G. Pitari, S. Reddy, Ø. Seland, P. Stier, and T. Takemura (2006), Radiative forcing by aerosols as derived from the AeroCom present-day and pre-industrial simulations, *Atmos. Chem. Phys., 6***,** 5225–5246.

Sekiguchi, M., and T. Nakajima (2008), A k-distribution-based radiation code and its computational optimization for an atmospheric general circulation model. *J. Quant. Spectrosc. Radiat. Transfer*, *109*, 2779–2793.

Sutherland, R. A., and R. K. Khanna (1991), Optical properties of organic-based

aerosols produced by burning vegetation, *Aerosol Sci, Techonol*., *14*, 331-342.

Takata, K., S. Emori, and T. Watanabe (2003), Development of the minimal advanced treatments of surface interaction and runoff, *Global Planet. Change*, 38, 209–222.

Takemura, T., H. Okamoto, Y. Maruyama, A. Numaguti, A. Higurashi, and T. Nakajima (2000), Global three-dimensional simulation of aerosol optical thickness distribution of various origins, *J. Geophys. Res.*, *105*, 17,853– 17,873.

Takemura, T., T. Nakajima, O. Dubovik, B. N. Holben, and S. Kinne (2002), Single scattering albedo and radiative forcing of various aerosol species with a global three-dimensional model, *J. Clim*., *15*, 333–352.

Takemura, T., T. Nozawa, S. Emori, T. Y. Nakajima, and T. Nakajima (2005), Simulation of climate response to aerosol direct and indirect effects with aerosol transport-radiation model, *J. Geophys. Res.*, *110*, D02202, doi:10.1029/ 2004JD005029.

Takemura, T., M. Egashira, K. Matsuzawa, H. Ichijo, R. O'ishi, and A. Abe-Ouchi (2009), A simulation of the global distribution and radiative forcing of soil dust aerosols at the Last Glacial Maximum, *Atmos. Chem. Phys*., *9*, 3061-3073, doi:10.5194/acp-9-3061-2009.

Tang, I. N., and H. R. Munkelwitz (1994), Water activities, densities, and refractive indices of aqueous sulfates and sodium nitrate droplets of atmospheric importance, *J. Geophys. Res.*, *99*, 18,801– 18,808.

Textor, C., M. Schulz, S. Guibert, S. Kinne, Y. Balkanski, S. Bauer, T. Berntsen, T. Berglen, O. Boucher, M. Chin, F. Dentener, T. Diehl, R. Easter, H. Feichter, D. Fillmore, S. Ghan, P. Ginoux, S. Gong, A. Grini, J. Hendricks, L. Horowitz, P. Huang, I. Isaksen, I. Iversen, S. Kloster, D. Koch, A. Kirkevåg, J. E. Kristjansson, M. Krol, A. Lauer, J. F. Lamarque, X. Liu, V. Montanaro, G. Myhre, J. Penner, G. Pitari, S. Reddy, Ø. Seland, P. Stier, T. Takemura, and X. Tie (2006), Analysis and quantification of the diversities of aerosol life cycles within AeroCom, *Atmos. Chem. Phys.*, *6*, 1777-1813, doi:10.5194/acp-6-1777-2006.

Thomson, A. M., K. V. Calvin, S. J. Smith, G. P. Kyle, A. Volke, P. Patel, S. Delgado-Arias, B. Bond-Lamberty, M. A. Wise, L. E. Clarke, and J. A. Edmonds (2011), RCP4.5: a pathway for stabilization of radiative forcing by 2100, *Clim. Change*, *109*, 77–94.

Twomey, S. (1977), Influence of pollution on shortwave albedo of clouds. *J. Atmos. Sci.*, *34*, 1149–1152.

Vaughan, M., K. Powell, R. Kuehn, S. Young, D. Winker, C. Hostetler, W. Hunt, Z. Liu, M. McGill, and B. Getzewich (2009), Fully automated detection of cloud and

aerosol layers in the CALIPSO lidar measurements, *J. Atmos. Oceanic Technol.*, *26*, 2034–2050.

Vaughan, M., R. Kuehn, J. Tackett, R. Rogers, Z. Liu, A. Omar, B. Getzewich, K. Powell, Y. Hu, S. Young, M. Avery, D. Winker, and C. Trepte (2010), Strategies for improved CALIPSO aerosol optical depth estimates, *Proceedings of the 25th International Laser Radar Conference*, 1340–1343, ISBN 978-5-94458-109-9.

Watanabe, M., S. Emori, M. Satoh, and H. Miura (2009), A PDF based hybrid prognostic cloud scheme for general circulation models, *Climate Dyn.*, *33*, 795–816, doi:10.1007/s00382-008-0489-0.

Watanabe, M., T. Suzuki, R. O'ishi, Y. Komuro, S. Watanabe, S. Emori, T. Takemura, M. Chikira, T. Ogura, M. Sekiguchi, K. Takata, D. Yamazaki, T. Yokohata, T. Nozawa, H. Hasumi, H. Tatebe, and M. Kimoto (2010), Improved climate simulation by MIROC5: mean states, variability, and climate sensitivity, *J. Climate*, *23*, 6312–6335. doi: http://dx.doi.org/10.1175/2010JCLI3679.1.

Wilson, D. R., and S. P. Ballard (1999), A microphysically based precipitation scheme for the UK Meteorological Office unified model, *Quart. J. Roy. Meteor. Soc.*, *125*, 1607–1636.

Winker, D. M., M. Vaughan, A. Omar, Y. Hu, K. Powell, Z. Liu, W. Hunt, and S. A. Young (2009), Overview of the CALIPSO mission and CALIOP data processing algorithms, *J. Atmos. Oceanic Technol*., *26*, 2310-2323.

Winker, D. M., J. Pelon, J. A. Coakley Jr., S. A. Ackerman, R. J. Charlson, P. R. Colarco, P. Flamant, Q. Fu, R. M. Hoff, C. Kittaka, T. L. Kubar, H. Le Treut, M. P. McCormick, G. Mégie, L. Poole, K. Powell, C. Trepte, M. A. Vaughan, and B. A. Wielicki (2010), The CALIPSO Mission: A global 3D view of aerosols and clouds, *Bull. Amer. Meteor. Soc*., *91*, 1211-1229.

Winker, D. M., J. L. Tackett, B. J. Getzewich, Z. Liu, M. A. Vaughan, and R. R. Rogers (2013), The global 3-D distribution of tropospheric aerosols as characterized by CALIOP, *Atmos. Chem. Phys.*, *13*, 3345-3361, doi:10.5194/acp-13-3345-2013.

Yoshida, M., and H. Murakami (2008), Dust absorption averaged over the Sahara inferred from moderate resolution imaging spectroradiometer, *Appl. Opt.*, *47*, 1995-2003.

Young, S. A., and M. A. Vaughan (2009), The retrieval of profiles of particulate extinction from Cloud Aerosol Lidar Infrared Pathfinder Satellite Observations (CALIPSO) data: Algorithm description, *J. Atmos. Oceanic Technol.*, *26*, 1105-1119, doi:10.1175/2008 JTECHA1221.1.

Yu, H., R. E. Dickinson, M. Chin, Y. J. Kaufman, M. Zhou, L. Zhou, Y. Tian, O.

Dubovik, and B. N. Holben (2004), Direct radiative effect of aerosols as determined from a combination of MODIS retrievals and GOCART simulations, *J. Geophys. Res.*, *109*, D03206, doi:10.1029/2003JD003914.

Yu, H., Y. J. Kaufman, M. Chin, G. Feingold, L. A. Remer, T. L. Anderson, Y. Balkanski, N. Bellouin, O. Boucher, S. Christopher, P. DeCola, R. Kahn, D. Koch, N. Loeb, M. S. Reddy, M. Schulz, T. Takemura, and M. Zhou (2006), A review of measurement-based assessments of the aerosol direct radiative effect and forcing, *Atmos. Chem. Phys.*, *6*, 613-666, doi:10.5194/acp-6-613-2006.

Zhang, K., D. O'Donnell, J. Kazil, P. Stier, S. Kinne, U. Lohmann, S. Ferrachat, B. Croft, J. Quaas, H. Wan, S. Rast, and J. Feichter (2012), The global aerosol-climate model ECHAM-HAM, version 2: sensitivity to improvements in process representations, *Atmos. Chem. Phys*., 12, 8911-8949, doi:10.5194/acp-12-8911-2012.

Zhang, Z., K. Meyer, S. Platnick, L. Oreopoulos, D. Lee, and H. Yu (2014), A novel method for estimating shortwave direct radiative effect of above-cloud aerosols using CALIOP and MODIS data, *Atmos. Meas. Tech.*, 7, 1777-1789, doi:10.5194/amt-7-1777-2014.